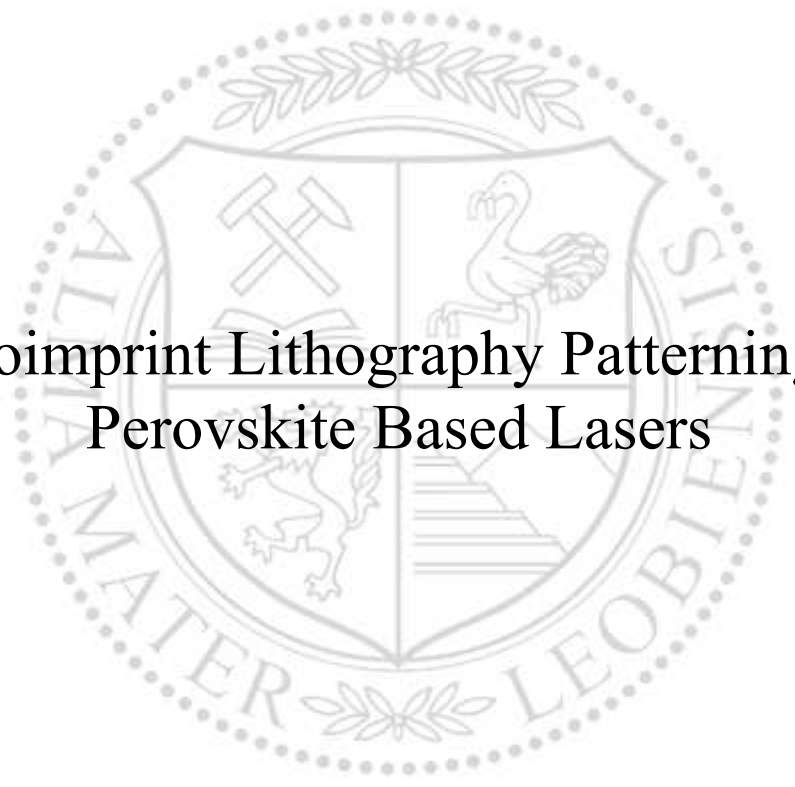




Chair of Physics

Master's Thesis



Nanoimprint Lithography Patterning for  
Perovskite Based Lasers

Simon Leitner, BSc

March 2023





---

---

## Nanoimprint Lithography Patterning for Perovskite Based Lasers

Master Thesis by Simon Leitner<sup>1</sup>

<sup>1</sup>simon.leitner@stud.unileoben.ac.at, m01535427, Montanuniversität Leoben, Austria

Leoben, Austria, February 28th, 2023

---

---

Supervisor: Iakov Goldberg<sup>2</sup>

Reviewer: Ao. Univ.-Prof. Dr. Christian Teichert<sup>3</sup>

<sup>2</sup>imec vzw, Leuven, Belgium

<sup>3</sup>Chair of Physics within the Department of Physics, Mechanics and Electrical Engineering,  
Montanuniversität Leoben, Austria





**EIDESSTÄTTLICHE ERKLÄRUNG**

Ich erkläre an Eides statt, dass ich diese Arbeit selbständig verfasst, andere als die angegebenen Quellen und Hilfsmittel nicht benutzt, und mich auch sonst keiner unerlaubten Hilfsmittel bedient habe.

Ich erkläre, dass ich die Richtlinien des Senats der Montanuniversität Leoben zu "Gute wissenschaftliche Praxis" gelesen, verstanden und befolgt habe.

Weiters erkläre ich, dass die elektronische und gedruckte Version der eingereichten wissenschaftlichen Abschlussarbeit formal und inhaltlich identisch sind.

Datum 28.02.2023

---

Unterschrift Verfasser/in  
Simon Leitner



## Acknowledgments

Creating this thesis was a little adventure for me, as I explored both a new country and a field of research that I did not know before. It would not have been possible without the support of very special people, to which I owe many thanks:

To **Iakov Goldberg**, for taking me in, sharing his knowledge with me, and patiently teaching me the diligence required for working in a field that was completely new to me. You were a great teacher.

To **Nirav Annavarapu**, for trusting me to not mess up his optical setup too much, and for helping me realign in case I still knocked a mirror over. You showed me the joy that sitting in complete darkness for multiple hours can bring.

To my thesis supervisor **Prof. Christian Teichert** for his valuable feedback, his patience, and his willingness to supervise a thesis that was performed abroad.

To **Karim Elkhoully**, **Robert Gehlhaar**, and **Prof. Jan Genoe**, for sharing their expertise on lasers and perovskites with me.

To my partner, for bearing with me both during our stay in Belgium and back in Austria while I was writing my thesis. Times like these can be stressful, and having support at my side makes everything seem a little more bearable.

To my family. Their support allowed me to take many opportunities in life so far, and brought me to where I am now. You gave your curious child everything he needed to follow his heart.

## Abstract

In this thesis, nanoimprint lithography (NIL) is evaluated as a possible process route to develop 2<sup>nd</sup> order one-dimensional distributed feedback Bragg (DFB) resonators for perovskite based thin film lasers. The main focus hereby lies on the perovskite methylammonium lead iodide ( $\text{CH}_3\text{NH}_3\text{PbI}_3$ ,  $\text{MAPbI}_3$ ). Grating resonators are prepared using an all-solution process and are evaluated using optical multispectral analysis, electron microscopy, as well as simulations.

Optically pumped lasing with low threshold ( $\sim 80\mu\text{J}/\text{cm}^2$ ) and narrow linewidth ( $< 0.1\text{nm}$ ) from a  $\text{MAPbI}_3$  layer coupled to a grating which is processed via UV-NIL is demonstrated. Identification of lasing versus other phenomena like amplified spontaneous emission (ASE) or random lasing (RL) in this scenario is aided by studying angular emission features, translational invariance, and far-field images. During experiments, it is found that an optical excitation with a linear shape can prevent parasitic losses through ASE. Grating-free areas should not be excited to restrict the influence of RL. It is noted that coupled wave theory is necessary for conclusive proof of lasing, which would exceed the scope of this thesis.

The evaluation of different processing parameters like curing times and temperatures highlights that curing temperatures need to be low enough not to degrade the perovskite, but high enough to enable proper adhesion.

The dry-etch process for the preparation of master stamps used during NIL is revised. For this purpose, etch parameters are varied and the resulting grating structures are analyzed using cross-sectional scanning electron microscopy (XSEM).

The thesis demonstrates that the UV-NIL route can produce gratings that support lasing. The experienced adhesion problems point to opportunities for further improvement and research in the scope of similar thin film systems. The increased throughput and the minimization of the need for expensive lithography tools enable fast and cheap manufacture of many samples, and may significantly aid and accelerate research in the field of perovskite gain media.



## Zusammenfassung

In dieser Arbeit wird Nanopräge-Lithografie (nanoimprint lithography, NIL) als möglicher Prozess zur Herstellung von eindimensionalen Distributed Feedback (DFB) Resonatoren zweiter Ordnung für Perowskit-basierte Dünnschichtlaser untersucht. Der Hauptfokus liegt hierbei auf dem Perowskit Methylammoniumbleiiodid ( $\text{CH}_3\text{NH}_3\text{PbI}_3$ ,  $\text{MAPbI}_3$ ). Gitter-Resonatoren werden durch einen All-Solution-Prozess hergestellt und mittels optischer Multispektral-Analyse, Elektronenmikroskopie als auch Simulationen evaluiert.

Optisch angeregtes Lasing von  $\text{MAPbI}_3$  mit einem in UV-NIL Technik hergestelltem Gitter wird demonstriert, welches niedrige Schwellenwerte ( $\sim 80 \mu\text{J}/\text{cm}^2$ ) und Linienbreiten ( $< 0.1 \text{nm}$ ) aufweist. Die Identifikation von Lasing gegenüber anderen in diesem Kontext auftretenden Phänomenen wie verstärkter spontaner Emission (ASE) oder Random Lasing (RL) wird durch Analyse der Emissionswinkel, der Translationsinvarianz und des Fernfeldes unterstützt. Während den Untersuchungen wird festgestellt, dass eine Anregung in Linienform parasitäre Verluste durch ASE minimieren kann. Keine gitterfreien Bereiche sollten angeregt werden, um den Einfluss von RL einzuschränken. Es wird darauf hingewiesen, dass „Coupled Wave Theory“ für einen schlüssigen Nachweis von Lasing nötig ist, was aber den Rahmen dieser Arbeit übersteigen würde.

Durch Untersuchung unterschiedlicher Prozessparameter wie Aushärtezeiten und -temperaturen wird gezeigt, dass die Aushärtung schonend genug sein muss, um den Perowskiten nicht zu schädigen, aber stark genug, um angemessene Adhäsion und Strukturtransfer zu gewährleisten.

Die Trockenätzung für die Herstellung von Hauptstempeln für NIL wird überarbeitet. Dazu werden Ätzparameter variiert und die daraus folgenden Gitterstrukturen durch Querschnittsanalyse im Rasterelektronenmikroskop (XSEM) untersucht.

Die Arbeit belegt, dass die UV-NIL-Routine Gitter erzeugen kann, die Lasing hervorrufen. Die aufgetretenen Adhäsionsprobleme zeigen Verbesserungs- und Forschungsmöglichkeiten in ähnlichen Dünnschichtsystemen auf. Der erhöhte Durchsatz und die Minimierung des Einsatzes teurer Lithografieanlagen ermöglichen schnelle und günstige Herstellung vieler Proben, und könnte die Forschung im Gebiet von Perowskit-Verstärkermedien erleichtern und beschleunigen.

## Content

Acknowledgments .....	I
Abstract .....	II
Zusammenfassung.....	III
List of Abbreviations.....	VI
1. Introduction.....	1
2. Aim .....	3
3. Theoretical Background .....	4
3.1. Laser fundamentals .....	4
3.2. Nanoimprint Lithography .....	9
3.3. Spin Coating.....	10
3.4. Perovskites.....	12
4. Methods .....	13
4.1. Solution Preparation.....	13
4.2. Substrate Cleaning.....	14
4.3. Spin Coating of Perovskite.....	14
4.4. ITO Deposition .....	16
4.5. Spin Coating of UV-NIL Resin.....	16
4.6. Nanoimprint Process .....	17
4.7. Master Stamp Layout .....	22
4.8. Simulations .....	26
4.9. Ellipsometry .....	27
4.10. Optical Measurements.....	27
4.11. Analysis of Optical Measurements .....	36

5.	Results .....	42
5.1.	Simulations .....	42
5.2.	Ellipsometry .....	46
5.3.	Cross-Sectional Scanning Electron Microscopy .....	47
5.4.	Adhesion Improvement.....	54
5.5.	Sample List.....	56
5.6.	Sample 1: Spot vs. Line Excitation .....	57
5.7.	Sample 2: Cryo-Cooling.....	59
5.8.	Sample 3: Grating Length Study .....	61
5.9.	Sample 4: Main Findings.....	62
5.10.	Sample 5: FAPb <sub>3</sub> .....	73
6.	Discussion .....	76
6.1.	Simulation .....	76
6.2.	Ellipsometry .....	76
6.3.	Cross-Sectional Scanning Electron Microscopy .....	76
6.4.	Adhesion improvement .....	78
6.5.	Sample 1: Spot Excitation .....	79
6.6.	Sample 2: Cryo-Cooling.....	80
6.7.	Sample 3: Grating Length Study .....	81
6.8.	Sample 4: Main Findings.....	81
6.9.	Sample 5: FAPb <sub>3</sub> .....	84
7.	Summary and Outlook .....	85
8.	Literature .....	87

## List of Abbreviations

ACE	acetone
ASE	amplified spontaneous emission
BFP	back focal plane
CB	chlorobenzene
CCD	charge-coupled device
CMOS	complementary metal oxide semiconductor
CMR	carcinogenic, mutagenic, and/or reprotoxic
DBR	distributed Bragg reflector
DFB	distributed feedback resonator
DI	deionized
DMF	dimethyl formamide
DMSO	dimethyl sulfoxide
DOE	design of experiment
e-beam	electron beam
e.m.	electromagnetic
FAI	formamide iodide
FAPb <sub>3</sub>	formamidine lead iodide
FWHM	full width at half maximum
ICP-RIE	inductively coupled plasma reactive ion etching
IPA	2-propanol
ITO	indium tin oxide

LED	light-emitting diode
MAI	methylammonium iodide
MAPbI <sub>3</sub>	methylammonium lead iodide
MIBK	methyl isobutyl ketone
MS	master stamp
NDF	neutral density filter
NIL	nanoimprint lithography
NPA	1-propanol
OLED	organic light emitting diode
OMA	optical multichannel analyzer
PbI <sub>2</sub>	lead iodide
PeLED	perovskite light-emitting diode
PET	polyethylene terephthalate
PGMEA	propylene glycol methyl ether acetate
PMAI	phenylmethanamine iodide
PMMA	polymethyl methacrylate
RL	random lasing
ROI	region of interest
SE	spontaneous emission
TE	transverse electric
TLD	thermoluminescence detector
TM	transverse magnetic
WGM	whispering-gallery mode
XSEM	cross-sectional scanning electron microscopy

## 1. Introduction

A fascination with light has followed humanity for a long time. Throughout the centuries, humanities' attempts to tame it have been closely correlated with developmental steps in different areas - starting with open fire, moving on to candles, to gas lighting, until finally electrical lights were state of the art around the turn of the century.<sup>1</sup> During the advent of quantum theory in the early 1920s, the principle of stimulated emission – the foundation of lasing – was first established by Einstein.<sup>2,3</sup> It took until 1960 for this idea to be realized with the first laser reported by Maiman.<sup>4</sup>

As of right now, laser manufacturing is quite expensive and complex. It would be beneficial to multiple branches of industry to be able to produce lasers with cheap, facile, and robust processes. In recent years, a lot of research effort was directed toward studying organic solid-state light emitters, which culminated with the industrialization of organic light-emitting diodes (OLEDs). Organic lasers were also studied at length, and optically pumped systems were readily demonstrated.<sup>5-7</sup> Although an important step, they have only limited opportunities for commercialization, while electrically pumped systems would be of great interest to industry and technology development. Electrical pumping has not been reported as of today, mainly owing to the inherent drawbacks of the used organic systems (e.g., low refractive indices, electrode losses, polaron and triplet absorption, and low charge carrier mobility).<sup>8,9</sup>

This is where lately perovskites have been proposed as an interesting system in which some of those drawbacks could be bypassed. Strong confinement in the octahedral layers of the perovskite and strong Coulombic bonding of electron-hole pairs (cf. chapter 3.4) promises low-threshold polariton lasing. Some other major advantages are easy band gap engineering, low defect state density, and large absorption coefficients.<sup>10</sup> After being studied at length in the photovoltaic community, research focusing on light emitters was kickstarted and it did not take long until perovskite LEDs (PeLEDs) had been demonstrated.<sup>11</sup> Soon after, optically pumped lasing systems were developed.<sup>12</sup> Nevertheless, electrically pumped perovskite lasing has yet to be published.<sup>13</sup>

One bottleneck in sample fabrication is the resonator integration process. In the context of complementary metal oxide semiconductor (CMOS) and III-V processing, it is usually done using conventional lithography that involves the deposition of the resonator material, resist deposition, resist exposure (mostly with either photolithography or electron beam lithography), resist development, after which an etch step then transfers the pattern into the previously deposited material. The final step strips off both the residual resist and any by-products from etching.

This process involves multiple expensive tools to achieve the desired features (where lithography sets the attainable critical dimensions) and takes up a lot of time.<sup>14</sup> Trying to circumvent those issues, nanoimprint lithography has been explored, especially for applications where large areas have to be covered in a cost-effective manner and the critical dimensions are quite relaxed.<sup>15</sup> Progress has been made, and industrial systems and applications are on the rise.<sup>16</sup>

## 2. Aim

Research was conducted at *imec vzw* in a group that has extensive knowledge of perovskite light emitting devices and is working towards creating an electrically pumped perovskite laser.

The resonator structures are currently produced in the traditional lithography process. As perovskites may not be introduced into etching tools, the grating is patterned underneath the perovskite. If the perovskite is then deposited via spin coating, it will fill the resonator trenches. This is unfavorable for both thresholds and outcoupling efficiency as shown by *Bonal et al.*,<sup>17</sup> and may reduce surface planarity for all layers deposited above it. Also, the electron beam (e-beam) writing process for creating resonator structures creates a bottleneck, since in-house capabilities are limited and out-of-house writing is expensive and restricted to a few samples every two weeks. An additional limitation is the inherent instability of the used perovskites towards ambient O<sub>2</sub> or H<sub>2</sub>O vapor and towards certain solvents like dimethyl formamide (DMF) or dimethyl sulfoxide (DMSO).

Nanoimprint lithography (NIL) (cf. chapter 3.2) would allow for much higher throughput, at a much cheaper cost. The deposited layers would benefit from improved planarity as the grating could be deposited above the perovskite (and any interlayers, if present), and losses due to perovskite patterning could be mitigated. Studying different resonator structures is also made much easier, as one NIL master stamp can incorporate a plethora of different geometries.

Therefore, the aim of this work is the following:

- 1) Create resonator structures using NIL
- 2) Model and simulate said structures
- 3) Study the optical properties of said structures
- 4) Study and explain the observed features

Studies will focus on the optical pumping of resonators fabricated directly above perovskite active media. The emission parameters like amplified spontaneous emission (ASE) or lasing thresholds, angular spread, polarization, and images in near- and far-field will be analyzed.



### 3. Theoretical Background

#### 3.1. Laser fundamentals

Here, a short overview will be given; for an in-depth treatment of the topic, the reader will be referred to literature, for example the book by Svelto<sup>18</sup>, from which a lot of inspiration for this summary has been drawn.

Three principles are important to create a laser<sup>18</sup>:

- An active material
- A pumping scheme
- A resonator

##### 3.1.1. Active Material

Active materials rely on the concept of stimulated emission. This derivation is based on a semi-classical treatment, meaning electrons and atoms will be seen as quantum states, while the photons will be treated as classical electromagnetic (e.m.) waves following Maxwell's equations. A photon then can excite an electron to an elevated energy state – this is known as absorption. Within its lifetime, this electron can relax back to its original state by either emitting a photon with an energy equivalent to the difference between the two levels – radiative decay also known as spontaneous emission, or by any nonradiative decay mechanism. If the excited electron is hit by a photon (= e.m. wave) that has the same wavelength as the energy gap between the two levels, it follows from perturbation theory that there is a chance that this photon forces the electron to relax to the lower energy level, therefore releasing a second photon of the same wavelength, phase, and direction – basically duplicating the incident photon (= doubling the amplitude of the incident e.m. wave). This process is referred to as stimulated emission.<sup>18,19</sup>

In absence of strong external excitation, the population of electrons in the ground states is higher than the one in the excited states (as is the case for thermal equilibrium), and the material will act as an absorber. But if the number of electrons in the excited state becomes higher, also known as population inversion, the material will act as an amplifier. In such a scenario, the probability of stimulated emission will be higher than absorption. The ability of certain materials to amplify light is coined "gain". In a full laser device with multiple functional layers, this material will then be called "active".

### 3.1.2. Pumping Scheme

The way in which population inversion can be achieved is called a pumping scheme.

For a two-level system in thermal equilibrium, the number of electrons in the lower energy state will remain larger than in the higher one. Through continuous optical or current-injection pumping, the low-energy electrons can be excited into the higher level. Upon increasing the excitation intensity, excitation (= absorption) and stimulated emission may compensate each other. In this case, the material would become transparent for further photons, and therefore a steady state population inversion can never be reached in a system with only two levels.<sup>18</sup>

If the system instead consists of three energy levels, the electrons can be excited from the ground to the highest level, then decay onto an intermediate level. Population inversion is then reached between the ground and intermediate levels. For a system of four energy levels, population inversion would be reached between two intermediate levels, with the big advantage that any electron in the higher intermediate level would immediately produce population inversion, as the lower intermediate level would be empty.<sup>18</sup>

One can also think about how the electrons are pumped to higher excitations. This can be achieved through optical pumping, meaning the active material is irradiated by light quanta with more energy than needed for the transition. While this is quite easy to set up by directing another laser at the active material, the usefulness of such a device is limited as it relies on the other laser, driven by a current injection.

More desirable is a system that can be electrically pumped. Here, the energy needed for the transition is supplied by electric current. The challenge of how to get the current to the active material is a very big one. For that reason, electrodes are applied to the active material. Electrons and holes need to be injected in balance, and their recombination should be predominantly radiative. Although not strictly necessary to achieve injection lasing, electrodes that are transparent to the emitted light on at least one side of the device facilitate probing the emission characteristics. Since most electrode materials have work functions that are not suitable to achieve direct ohmic contact with an active material, electron (or hole) transfer regions may be needed to facilitate current flow.

### 3.1.3. Resonator

To transform an amplifier into an oscillator, positive feedback must be established, where some of the light created due to stimulated emission is passed through the material anew. In the simplest form, this can be achieved by placing two parallel mirrors next to the active material; other resonator types rely on periodic structures or gratings to create constructive interference of selected wavelengths (e.g. distributed Bragg reflectors [DBR]<sup>20</sup>, distributed feedback [DFB]<sup>17,21,22</sup> and whispering-gallery mode [WGM]<sup>23,24</sup> resonators).

For the current work, a 2<sup>nd</sup> order DFB resonator will be used. It is characterized by light emission perpendicular to the grating surface (compared to in-plane emission for 1<sup>st</sup> order DFBs). The DFB resonator structure is very simple, adaptable, and easy to manufacture. The resonance condition for such a grating can be calculated using the equation

$$m * \lambda = 2 * n_{eff} * \Lambda \quad \text{Eq. 1}$$

a modified version of Bragg's law, where  $m$  is the diffraction order,  $\lambda$  the lasing wavelength,  $n_{eff}$  the effective refractive index of the grating, and  $\Lambda$  the period of the grating.<sup>25</sup>

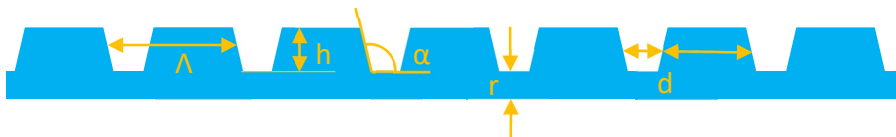


*Fig. 1: Grating resonator schematic. Critical parameters are shown in yellow:  $\Lambda$ ...period,  $h$ ...tooth height,  $\alpha$ ...tooth angle,  $r$ ...residual layer,  $d$ ...duty cycle.*

Furthermore, a grating can be characterized by its geometric properties, as shown in Fig. 1. The main characteristic is the period  $\Lambda$ , but properties of the grating teeth like height  $h$ , residual layer thickness  $r$ , duty cycle  $d$  (the ratio of tooth width to period), tooth shape (e.g., tooth angle  $\alpha$  for trapezoidal teeth) influence the amount of coupling between active material and grating and affect  $n_{eff}$ .

The effective refractive index  $n_{\text{eff}}$  captures the effect of the variation of all those parameters. It is only accessible through simulations, involved measurements, or approximation. The physical characteristics of the grating can be understood as a periodic modulation of  $n_{\text{eff}}$ , termed  $\Delta n_{\text{eff}}$ .

One parameter commonly used to describe the quality of a resonator is the quality (or Q) factor, which can be defined in two ways: The first is the amount of energy stored in the resonator in relation to the energy dissipated by one round trip, the second is the relation of resonance frequency  $\nu$  to resonance bandwidth at the full width at half maximum (FWHM)  $\Delta\nu_c$ <sup>26</sup>:

$$Q = 2\pi \frac{E_{\text{stored}}}{E_{\text{dissipated}}} = \frac{\nu}{\Delta\nu_c} \quad \text{Eq. 2}$$

Common Q-factors for cavity resonators can range around  $10^4$ - $10^5$ , while spectral lines of certain elements can be measured to achieve  $10^5$ - $10^7$ .<sup>27</sup>

A special characteristic of a DFB resonator is the relationship between the photonic band structure and the emission characteristics, which are heavily influenced by the grating. Photonic band structure describes which wavelengths of light are scattered under which angle when interacting with a photonic structure like a grating. For angles  $\theta$  far away from normal incidence, the following relationship holds:

$$\frac{2\pi}{\lambda} \sin(\theta) = \pm \frac{2\pi n_{\text{eff}}}{\lambda} \pm m \frac{2\pi}{\Lambda} \quad \text{Eq. 3}$$

This equation states the conservation of momentum for photons within the resonator. A forward and a backward propagating standing wave within the resonator will thus be outcoupled by the grating under different angles depending on the wavelength of light, which can be seen and is discussed in chapters 5.6-5.10.<sup>28,29</sup>

### 3.1.4. SE, Lasing, ASE, Random Lasing

Once a system of active material, resonator, and pump is in operation, different emission phenomena can be observed.

Spontaneous emission (SE) is the most basic phenomenon, being responsible for both fluorescence and incandescence. The physics to describe it requires quantum field theory, so it will not be further explained here.<sup>18</sup> Distinguishingly, the emitted radiation has a wide spectral range on the order of 20-50 nm, and no phase relation or spatial coherence.<sup>18</sup>

Amplified spontaneous emission (ASE) may occur if an optically dense medium (which the studied perovskites with their  $n \sim 2.4$  are) has high enough gain, that the emitted fluorescence light is amplified in a single pass<sup>30</sup>. The resulting beam has some degree of special coherence and a narrower spectral width down to 10nm.<sup>18</sup> Just like SE, ASE appears without the presence of a resonator, which is different from lasing. Also, if a resonator is present, ASE is influenced only weakly due to its single-pass nature.<sup>30</sup> The spectral linewidth and spatial beam width are also larger than for laser peaks by about a factor of 10 or over 100, respectively. ASE also displays a threshold: below it, the losses in the material reduce the single-pass net gain enough to prohibit amplification.<sup>18</sup>

Lasing itself has certain spectral characteristics that make it useful in a plethora of applications. For example, the presence of a resonator introduces positive feedback into the laser system and leads to high spatial coherence of the emitted beam. Also, photons generated by stimulated emission have the same direction and phase as the photons that caused them.<sup>18</sup> The resulting beams show high spatial coherency and possess narrow spectral line widths (often far below 1nm, depending on the quality factor of the resonator). For resonators that are polarization-selective (such as a grating), the output is also strongly polarized. Lasing also shows a distinct threshold above which it appears, as additional losses in the cavity from e.g., resonator mirrors have to be overcome first.<sup>30</sup>

Random lasing (RL) occurs in media with strong gain that also have many scattering centers contained in them. These scattering centers resemble lasing feedback features but are usually not well-controlled and thus undesirable. Light may follow a path within the sample undergoing multiple scattering events, which leads to a speckle-like emission from the sample.

Random lasers do not select a specific mode within the gain medium that is amplified. Instead, multiple modes can obtain amplifying conditions. The resulting spectrum can then consist of multiple fine lines close to each other, with line widths also reaching below 1nm.<sup>[25]</sup>

### 3.2. Nanoimprint Lithography

After two initial papers by Chou in 1995<sup>31</sup> and 1996<sup>32</sup>, nanoimprint lithography (or NIL) became vastly popular in research, as it was seen as a possible method for low-cost, high-throughput lithography. It never became a competitor in driving Moore's law forward and has not yet seen widespread commercial use. But it is a very reasonable approach for creating large-area structures in microelectronics design, and possible success in the area of photonics and light sources is predicted.<sup>15,33,34</sup>

*"Nanoimprint lithography (NIL) is a high throughput, high-resolution parallel patterning method in which a surface pattern of a stamp is replicated into a material by mechanical contact and three dimensional material displacement. This can be done by shaping a liquid followed by a curing process for hardening, by variation of the thermomechanical properties of a thin film by heating and cooling, or by any other kind of shaping process using the difference in hardness of a mold and a moldable material. The local thickness contrast of the resulting thin molded film can be used as a means to pattern an underlying substrate on [sic!] waver level by standard pattern transfer methods, but also directly in applications where a bulk modified functional layer is needed. Therefore it is mainly aimed towards fields in which electron beam and high-end photolithography are costly and do not provide sufficient resolution at reasonable throughput."*<sup>33</sup>

The definition by H. Schiff points us to the use of NIL in this work: Herein, a UV-curable resin is spin-coated and imprinted with a periodic structure that may act as a resonator on top of the active material. Therefore, an emphasis on UV-NIL is appropriate.

In UV-NIL, a curable polymer is applied either by spin-coating or spray-coating onto a substrate. The layer is then imprinted with a stamp, that will transfer a negative of the structure on the stamp onto the film. With the stamp still present, the array is exposed to UV light, to cure the layer. Afterward, the stamp can be removed by either peeling or lifting it off. Roll-to-roll-based approaches are being investigated but were not used in this thesis.<sup>14,16</sup> A schematic of the UV-NIL process as used within this thesis can be seen in Fig. 4.

It is also possible to use intermediate stamps, an approach pioneered by the company *obducat*. For this, the master stamp is coated with a curable polymer, which is backed by a soft supporting layer and then cured. After demolding, this intermediate stamp can be used to imprint the surface of samples, rather than the master stamp. This limits contamination and degradation of the master stamp, but introduces another replication step that might be associated with its own issues and introduce defects.<sup>35</sup> Important parameters for imprinting are the layer thickness, profile depth of the stamp, imprint force, time after contact (to allow for capillary filling), radiation dose, demolding force, etc.

### 3.3. Spin Coating<sup>36</sup>

Spin coating is used heavily to produce the samples for this work and is exploited for the perovskite deposition, and NIL master and working stamp fabrication. Spin coating is a process where a liquid is applied to a substrate held on a vacuum chuck, which is then rotated at high velocity. This spinning induces centrifugal forces, which fling excess liquid off the substrate and thin the film. In favorable spin coating conditions, the resulting films are very uniform (<1% thickness variation).

The process can be split up into four phases: deposition, spin-up, spin-off, and evaporation. During deposition, liquid is applied to the substrate – this can be done via a syringe or pipette, in an automated or manual fashion. The step can happen before (static deposition) or after spin-up (dynamic deposition). Dynamic deposition introduces the risk of splashing or decentral placement of the liquid, but may be necessary if the liquid deposited material interacts with the underlying layer, as in anti-solvent precipitation. Spin-up is a ramping up of the rotation

speed until the final speed is reached, usually characterized by an acceleration in  $\frac{rpm}{s}$ . If the liquid is already applied to the surface, it will start to spread out and will be aggressively expelled from the substrate.<sup>37</sup> Spin-off and evaporation both take place at the final spin speed, which is usually somewhere between 1000 and 10000 rpm: first excess liquid is thrown off the surface by the centrifugal force, then or parallel to it any solvent in the liquid may evaporate, thinning the final layer even more. The thickness of the liquid film depends on its rheological properties (density, viscosity), on the spin speed, and on eventual evaporation of the liquid during the process. Although sophisticated formulas can be derived<sup>38</sup>, the easier approach to predict film thickness  $H_f$  is to use empirical modeling following the formula Eq. 4, where  $\Omega$  is the spin speed, K and b are fitted parameters with b usually taking values close to 0.5.<sup>36</sup>

$$H_f = K\Omega^{-b} \quad \text{Eq. 4}$$

After deposition, often an annealing or baking step is done, wherein the substrate is placed onto a hotplate at an elevated temperature, to remove any remaining solvent from the coated film.

Different defects can appear:

- Striations – radial ridge-like variations in film thickness, usually resulting from capillary forces introduced during evaporation.
- Chuck marks – thickness variations caused by substrate deformation through excessive forces pressing the substrate against the chuck.
- Comets – if particles are on the surface or in the applied liquid, they might adhere to the surface, causing the liquid stream to be deflected, resulting in tails behind the particles.
- Dry spots, swirls – if a liquid is dispensed off-center, a swirl-like pattern or even an uncoated spot may appear.
- Dry edges/corners – if too little liquid is applied, it might not be sufficient to cover the whole surface, leading to outer regions staying uncoated.



### 3.4. Perovskites

Perovskites are crystals with the structure  $A^+B^{2+}X_3^-$ . They possess interesting structure-property relationships, which are readily adjustable by controlling anions, cations, and defectivities.<sup>39</sup>

Different (mainly inorganic) perovskites have piqued research interest in recent years, like  $BaTiO_3$  and  $BiFeO_3$  for their multiferroic properties, or high-temperature superconductors like YBCO, which has a complex structure based on perovskite.<sup>39</sup> (Organic) lead halide perovskites are within the most studied material class for optically active materials. They possess multiple selling points: they are easy to synthesize from readily available precursor powders, they are easily modifiable by exchanging cations and anions and adjusting their proportions in mixed-cation perovskites, and they lend themselves to solution processing.<sup>40–46</sup>

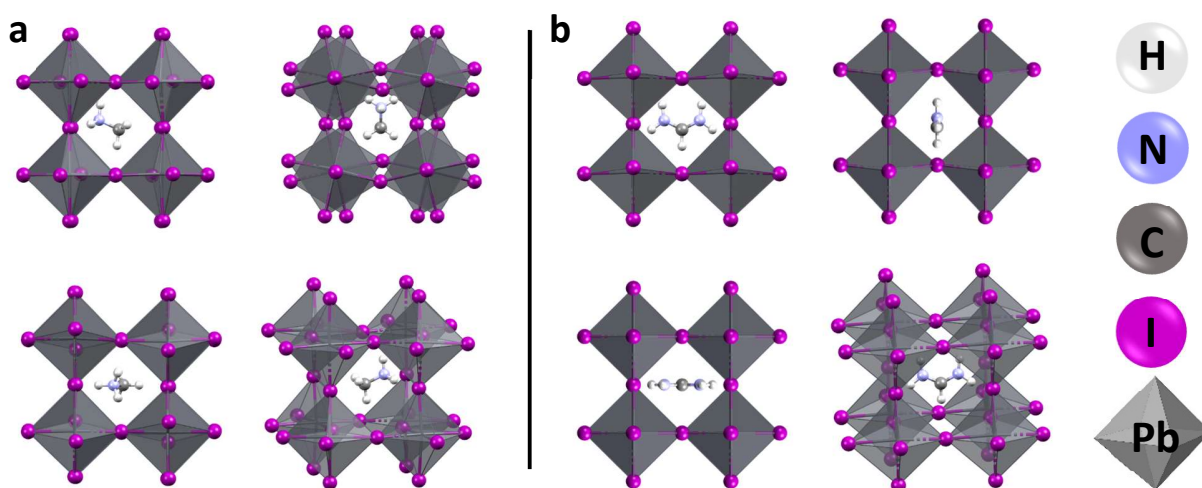


*Fig. 2: Simplified unit cell of  $MAPbI_3$  (a) and  $FAPbI_3$  (b). The unit cell is shown in projections along the unit cell axes as well as in perspective. The central organic ion can be seen enclosed between octahedra of  $PbI_6^{4-}$ . The octagons are tilted and/or twisted against each other.*

In this thesis, the focus is laid on the perovskite methylammonium lead iodide, commonly called  $MAPbI_3$ .  $MA^+$  ( $CH_3NH_3^+$ ) takes the A cation site, while  $Pb^{2+}$  is located at the B site of the lattice; the X sites are occupied by  $I^-$ . If visualized with A being the center of the unit cell, the organic molecule then sits in a volume surrounded by  $PbI_6^{4-}$  octahedra as illustrated in Fig. 2a.

Another perovskite investigated was formamidinium lead iodide, or  $FAPbI_3$ . The defining difference to  $MAPbI_3$  is that the  $MA^+$  ion is replaced by a  $FA^+$  ion ( $CH_5N_2^+$ ) as seen in Fig. 2b.

## 4. Methods

### 4.1. Solution Preparation

Precursors and solutions are stored in N<sub>2</sub> purged glove boxes for two reasons: Firstly, as a safety measure since lead compounds are used in our procedures that qualify as carcinogenic, mutagenic, or reprotoxic (CMR); additionally, special care is taken whenever handling of lead compounds is necessary, especially if it has to occur outside of the glovebox. Secondly, perovskites are inherently unstable in ambient air, as they react with O<sub>2</sub> and H<sub>2</sub>O.

The perovskite is synthesized by creating a solution of dry precursors in dimethyl formamide (DMF, *Sigma-Aldrich*). For MAPbI<sub>3</sub>, MAI (*Greatcell Solar Materials*) source and manufacturer and PbI<sub>2</sub> (*TCI Chemicals*) are mixed in a 1:1 molar ratio. The solution is diluted to 1.2M with DMF as a solvent for long-time storage (max. ~2 months), and further diluted to 0.6M before spin coating to obtain a desirable film thickness. FAPbI<sub>3</sub> is prepared in the same fashion, simply replacing MAI with FAI (*Greatcell Solar Materials*).

For each dry component and each solution desired, one glass vial is necessary. Glass vials (4ml) are blown with compressed N<sub>2</sub> and marked, and the ones for dry precursors are weighed empty. A magnetic stir bar is added to the vials for solutions.

Inside the glovebox, an eyeballed amount of dry powder is filled into the vials, while roughly accounting for the difference in molar weight to minimize waste. The powders are exported in a closed container. On precision scales housed in a laminar flow cabinet, the PbI<sub>2</sub> precursor is added to the solution vial and is differentially weighed. The required amount of MAI is calculated and added as precisely as possible to the same solution vial using a piece of Teflon weighing paper. The solution vial is brought back into the glove box, where the appropriate amount of DMF to prepare a 1.2M solution is added with a precision pipette. To dissolve the precursor, the vial is shaken and left overnight (or longer if needed) on a stir plate at ~800rpm at 40°C.

## 4.2. Substrate Cleaning

Substrates are cleaned using a six-step protocol (Tab. 1). All steps have the same duration of a minimum of 5mins, steps 2 to 5 take place in a heated ultrasonic bath (100W). The substrates are engraved with batch and sample number on the back side using a diamond pen, for easier recognition and handling. They are consequently slotted into a holder for cleaning. Immediately before spin coating, O<sub>2</sub> plasma cleaning is performed for 5min at 100W in a *Diener pico* tool.

Tab. 1: Cleaning procedure of substrates. ACE...acetone.

step	cleaning agent	t [min]	T [°C]
1	N <sub>2</sub> gas	short	RT
2	DI + detergent (~100:1)	5	40
3	DI	5	40
4	ACE	5	40
5	IPA	5	40
6	N <sub>2</sub> gas	until dry	RT

## 4.3. Spin Coating of Perovskite

The 1.2M stock solution is diluted to 0.6M using DMF before the process (ideally left overnight for perfect homogeneity). The cleaned substrates are brought into the glove box and placed on a vacuum chuck of the spin coater. 50µl of 0.6M MAPbI<sub>3</sub> solution is applied onto the resting substrate. The substrate is then spun according to the spin parameters (Tab. 2). After 3.5s of the spin, 150µl of toluene (*Sigma-Aldrich*) is dropped onto the spinning substrate to perform an antisolvent deposition.

Tab. 2: Spin and anneal parameters for perovskite deposition

spin speed	acceleration	duration	toluene drop	anneal
6000rpm	10000rpm/s	34s	after 3.5s	70°C, 5min

To adjust the thickness of the perovskite, the dilution of the stock solution can be changed according to a spin curve previously recorded in the group. From the fit, the corresponding values in the table below are calculated. The curve was recorded for  $\text{MAPbI}_3$  mixed with phenylmethylamine iodide (PMAI), an additive used to alter bulk morphology. The thickness of PMAI-free  $\text{MAPbI}_3$  closely follows the recorded spin curve. Moreover, the thickness of the samples was monitored using spectroscopic ellipsometry and profilometry measurements.

After the spin is complete, the substrate is placed on a hotplate to anneal for 5min at  $70^\circ\text{C}$ . Annealing is done in batches of 10 substrates. Samples are stored under  $\text{N}_2$  atmosphere with no  $\text{H}_2\text{O}$  or  $\text{O}_2$  content to prevent degradation of the perovskite.

*Tab. 3: Resulting thicknesses for different concentrations of perovskite*

layer thickness	solution dilution
120nm	0.6M
100nm	0.5M
80nm	0.4M

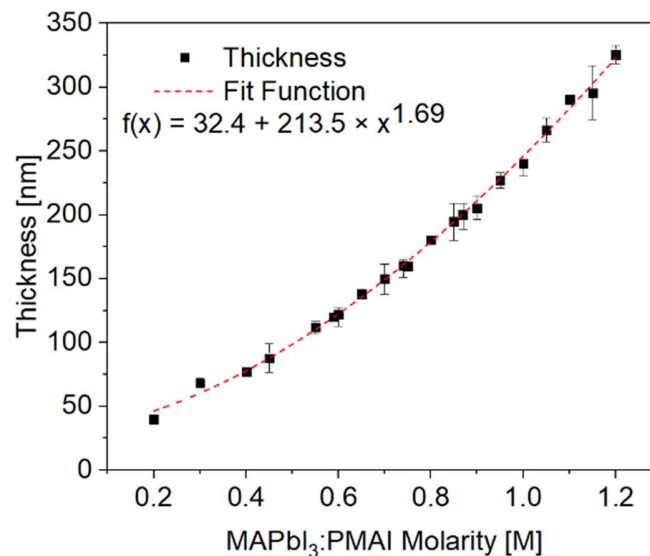


*Fig. 3: Spin curve for  $\text{MAPbI}_3$  with added PMAI. An exponential function is fitted to the data.*

#### 4.4. ITO Deposition

Indium tin oxide (ITO) was deposited on one batch of samples. One of those samples (sample 4) is discussed in this thesis. 20nm of ITO was deposited using DC-magnetron sputtering at 2mTorr and a substrate temperature of -5°C, with an O<sub>2</sub>/[O<sub>2</sub>+Ar] flow ration of around 3%. The deposition rate was 2nm/min. For some samples (including sample 4), a shadow mask was used to only cover half of the sample with ITO, thus obtaining identical ITO and ITO-free structures after NIL.

#### 4.5. Spin Coating of UV-NIL Resin

The substrates coated with the perovskite active layer are loaded onto the vacuum chuck of the spin coater inside the glove box. All processing is done under yellow light, as the resin is UV sensitive and will be cured under UV light in a dedicated tool in the cleanroom. The spin parameters (Tab. 4) are given for both adhesion promotor and NIL resin deposition.

*Tab. 4: Spin parameters for UV-NIL resin deposition*

spin speed	acceleration	duration	anneal
3000rpm	1000rpm/s	45s	variable

The liquids were dispensed either onto the substrate before spinning (“static drop”) or onto the spinning substrate after terminal velocity was reached (“dynamic drop”). The amount of liquid was increased from initially 100µl to 250µl, as incomplete coverage was observed in some previous cases. First, the perovskite was coated with adhesion promotor (if one was used), followed by curing it (cf. chapter 5.4). Afterward, the NIL resin was coated in a similar manner and also cured. During our investigations, the spin speed was varied to produce different thicknesses of NIL resin on top of the perovskite. The acceleration was directly coupled to the spin speed in this case, always amounting to 1/3 of the spin speed value (giving a fixed acceleration time of 3s).

## 4.6. Nanoimprint Process

The fully coated samples are introduced to the cleanroom via a sealed transfer container, to reduce the risk of particle contamination, UV exposure, and O<sub>2</sub>-induced degradation.

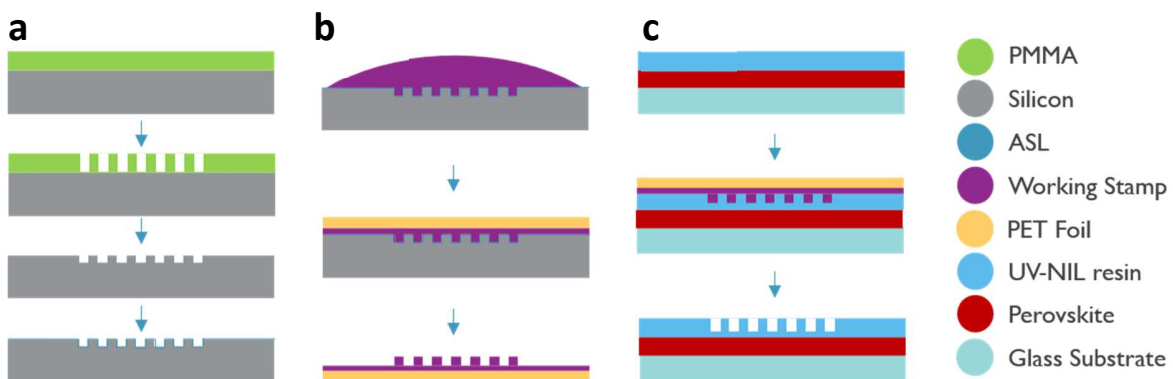


*Fig. 4: Schematic of the NIL process. In (a), the master stamp preparation is shown (resist deposition, patterning, pattern transfer, anti-sticking layer coating; cf. chapter 4.6.1). In (b), working stamp (WS) preparation is depicted (WS deposition, backing with carrier, delamination; cf. chapter 4.6.2). (c) shows the pattern transfer to a UV-NIL resin coated sample (contacting, exposure, demolding; cf. chapter 4.6.4).*

### 4.6.1. Master Stamp Preparation

A 2" p-doped Si wafer is prepared for electron beam writing. For that purpose, the wafer is cleaned and a chlorobenzene (CB) based polymethyl methacrylate (PMMA) solution with a molecular weight of 950kg/mol (AR-P 671.04; *Allresist GmbH*) is spin-coated (1000rpm, 333rpm/s acceleration, 45s, static drop) onto the Si wafer, which should result in a 300nm thick layer of PMMA. After a 3min bake at 165°C, the thickness is confirmed using a single spot ellipsometer. On top of the PMMA, 40nm of Electra 92 (AR-PC 5090.02; *Allresist GmbH*) is spin-coated (4000rpm, 1333rpm/s acceleration, 60s, static drop) and soft-baked for 2min at 90°C. This charge dissipation layer is used to improve writing quality: charge accumulations can lead to pattern displacement or distortion, the latter being a critical error when producing resonators.<sup>47</sup>

Electron beam writing is done at an external facility. The structures to be written were created in the program *KLayout*. A nanofabrication system from *Raith GmbH* is used to expose the resist with a dose of 101.2μC/cm<sup>2</sup>.

After electron beam exposure, the Electra layer is removed by a short deionized (DI) water rinse in an overflow bath, after which it is N<sub>2</sub> dried. The developer consists of a 1:1 ratio of methyl isobutyl ketone (MIBK) and 2-propanol (IPA), where IPA is used to dilute the developer. The mixture process is endothermic, hence the developer should be left out for at least 45min after mixing, so it can reach room temperature again.

The Si wafer is submersed into the developer for 60s without movement, after which it is promptly moved into a beaker filled with 200ml of 1-propanol (NPA) for 60s to stop the development, using slight movement. After removal from the second beaker, the wafer is dried using compressed N<sub>2</sub>, and a 2min hard bake at 90°C is performed to improve the plasma resistance of the resist. The wafer is then ready for plasma etching.

*Tab. 5: Etch parameters for ICP-RIE etch*

	SF <sub>6</sub> [sccm]	C <sub>4</sub> F <sub>8</sub> [sccm]	N <sub>2</sub> [sccm]	ICP [W]	RF [W]
Si etch	6	45	8	300	100

The wafer is then loaded into an *Oxford PlasmaLab 100* inductively-coupled plasma reactive ion etcher (ICP-RIE). The recipe run is outlined in Tab. 5. After completing the etch, the wafer is thoroughly cleaned in acetone (ACE) and IPA in an ultrasonic bath to remove the remaining PMMA resist. The resulting etch profile should be around 100nm deep.

A self-assembled monolayer of anti-sticking agent is applied to the stamp. For that purpose, the stamp is spin-cleaned with ACE and IPA, and activated in O<sub>2</sub>-plasma (100W, 5'). The anti-sticking agent (EVGASL 1, *EVG Group GmbH*) is applied to cover the whole wafer surface. Spin coating is done according to Tab. 6. The layer is annealed at 190°C for 1min. To remove excess anti-sticking agent, the wafer is spin-cleaned thoroughly with propylene glycol methyl ether acetate (PGMEA). This master stamp can be used for the preparation of multiple working stamps.

*Tab. 6: Spin coating and annealing parameters for anti-sticking layer*

substance	speed	acceleration	amount	spin time	anneal
EVGASL	3000rpm	1000rpm/s	Cover surface	30s	190°C, 1min

#### 4.6.2. Working Stamp Preparation

Three different working stamp materials were available, their characteristics are summarized in Tab. 7. All were obtained from *OpTool AB*, Sweden.

*Tab. 7: Summary of working stamp properties*

working stamp	non-sticking level	Martens hardness [N/mm <sup>2</sup> ]	viscosity [cPs]	suggested use
GMN-PS40	95%	0,39-0,4	~400	Pillars
GMN-PS90	88%	0,9-1,0	~750	Complex mix structure, slanted structure
GMN-PS380	62%	3,7-4,0	~600	Complex mix structure, high aspect ratio, slanted structure

Before spin coating of the working stamp material, the master stamp is first cleaned either using 5mins of 100W O<sub>2</sub> plasma and/or with ACE and IPA spin cleaning. Gentle mechanical rubbing using a clean room wipe with ACE can be used to remove the excess contamination. The working stamp material is then applied generously onto the master stamp, which has been loaded onto a vacuum chuck. Spin parameters can be found below (Tab. 8).

*Tab. 8: Spin parameters for working stamp deposition*

substance	speed	acceleration	amount	anneal
working stamp	3000rpm	1000rpm/s	500μl	none

A polyethylene terephthalate (PET) carrier foil is pre-exposed for ~5s to facilitate the removal of a protective cover, which is removed just before carefully placing the PET foil onto the coated surface. It is then gently but firmly rolled on with a hand roller, avoiding any bubbles between stamp and foil. The whole array of master stamp, working stamp material and foil is UV-A exposed for 300s at 100mW/cm<sup>2</sup>. After exposure, the wafer is left to cool down, before the foil



can carefully be delaminated from the master stamp. The working stamp (which consists of the hardened working stamp material and the backing foil) can then be used for further processing.

#### 4.6.3. Working Stamp Conditioning

To reduce the risk of delamination and to decrease adhesion between the working stamp and the UV resin spun above the perovskite, conditioning should be performed:

A 4" bare Si wafer (conditioning wafer) is spin cleaned using IPA (to promote hydrophilic surface conditions) coated with adhesion promotor and NIL resin according to the parameters presented in Tab. 9.

*Tab. 9: Spin and curing conditions for working stamp conditioning*

substance	speed	acceleration	amount	time	temperature
adhesion promotor	3000rpm	1000rpm/s	500 $\mu$ l	2min	120°C
NIL resin	3000rpm	1000rpm/s	500 $\mu$ l	1min	120°C

A clean room wipe is wetted with ACE, and coating on the edge is removed by hand before NIL resin curing, leaving a small circle of around 2" of coated surface. This is done to prevent the working stamp from sticking to the whole surface of the 4" wafer, aiding in demolding. The working stamp is applied to the conditioning wafer according to the procedure outlined in chapter 4.6.4. This process is done to reduce adhesion of the NIL resin to the working stamp surface.

#### 4.6.4. Pattern Transfer to the Sample

A substrate with perovskite and NIL resin is blown with N<sub>2</sub> and placed onto a Si carrier wafer. To prevent the sample from slipping, thick tape can be applied to the wafer, so that the sample can rest against the tape's ledges. The working stamp is then held at an angle of about 20° above the sample, keeping enough distance between stamp and sample to prevent the sample from dislocating. The roller is placed at the part of the stamp touching the working surface. The stamp is then brought in contact swiftly and firmly with the sample, without dropping the stamp onto the sample.

Any dirt on the sample or any excessive roughness might produce air bubbles between the sample and the working stamp. The utmost care is to be taken to prevent such flaws and maximize coverage; the use of a cleanroom environment facilitates the imprint. Above one minute is required to let the NIL resin fill nanometer-sized gaps of the working stamp before exposing the array (carrier wafer + sample + working stamp) with the  $100 \text{ mW/cm}^2$  UV-A irradiation for 100s.

After exposure, the whole assembly is left to cool down for one minute. After this, the working stamp is separated very cautiously and slowly. Upon lifting the foil at one corner of the sample, one performs a rolling motion to prevent delamination of the NIL resin from the perovskite. If delamination appears, the procedure should be stopped, and tried again at another corner of the sample. If the removal of the working stamp is successful, it may be reused for one or two more imprints, before pattern degradation makes it unusable (especially in the case of PS40). If some part of the NIL resin sticks to the working stamp, the stamp is discarded and a new one is produced for imprinting different samples.

A visual inspection under white light can be made to confirm grating structures on the sample. By tilting the sample, a grating diffraction pattern should appear under certain angles.

#### 4.7. Master Stamp Layout

During the thesis, three different master stamps were used. The first master stamp (MS1) was broken during imprinting, and had to be replaced by an identical stamp (MS2). The third stamp (MS3) was made to incorporate different grating types, and was adapted to accommodate a wider range of periods (Fig. 5).

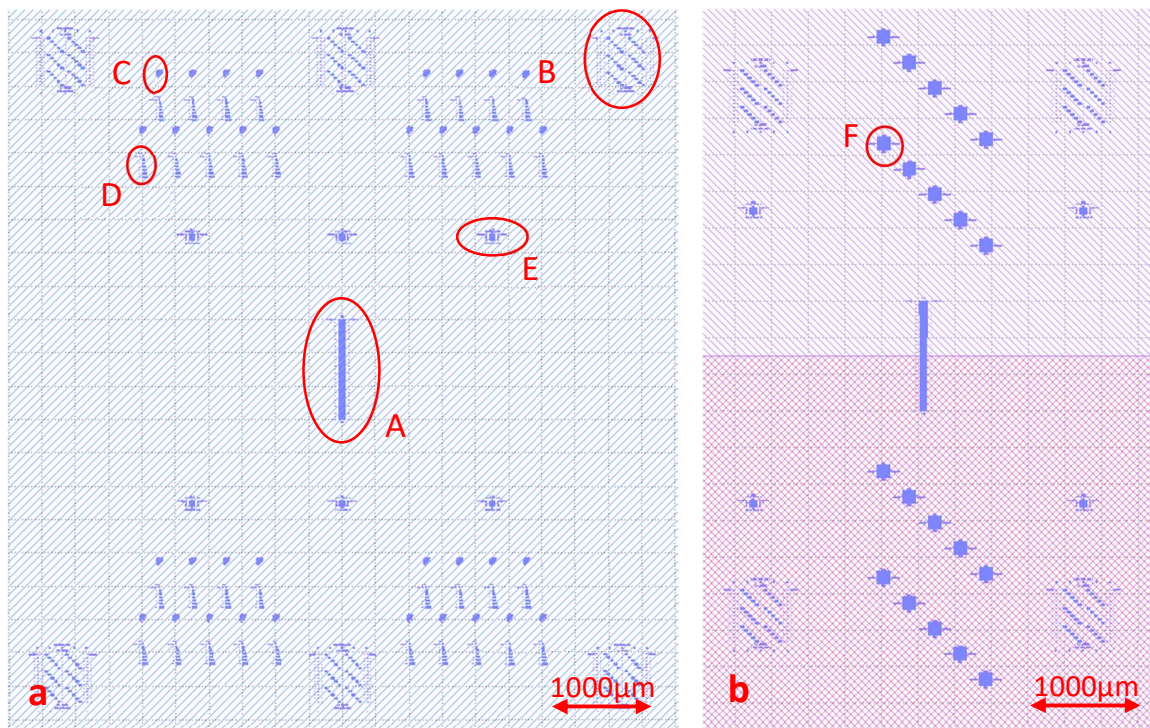


*Fig. 5: Layout of master stamps. The first two stamps (MS1, MS2) were fabricated according to the left layout (a), the third (MS3) according to the right layout (b). Different structures (A-F) are visible on the stamps and are shown in detail in Fig. 7.*

The first layout contains five distinct structure types, some of which are present multiple times with varying periods. Any arrows or small squares seen are used as orientation markers. This layout was produced to fabricate MS1 and MS2.

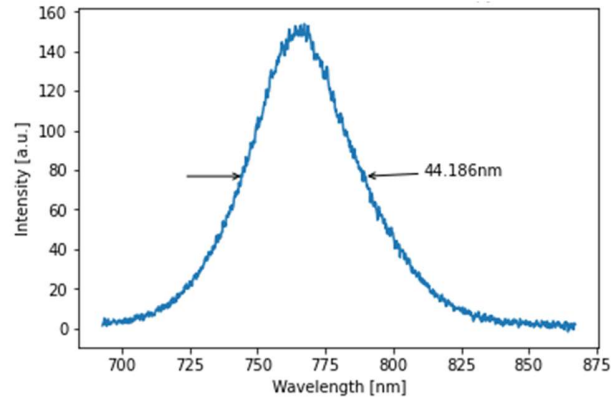


*Fig. 6: SE spectrum of MAPbI<sub>3</sub> below ASE or lasing threshold. A FWHM of ~45nm is indicated.*

All structures utilize 2<sup>nd</sup> order DFB gratings. From previous experiments, it is known that MAPbI<sub>3</sub> will emit light around 780nm with an FWHM of ~45 nm (Fig. 6).

To find out which period of gratings should show resonance with the light emitted by the perovskite, Eq. 1 turns to  $(780 \pm 40)nm = n_{eff} * \Lambda$ . Assuming  $n_{eff} \sim 2$  as expected from simulations (cf. 5.1 Simulations), the period should be in the range of  $\Lambda \sim 390nm$ . Accordingly, the periods of gratings on master stamps range between 350nm and 480nm.

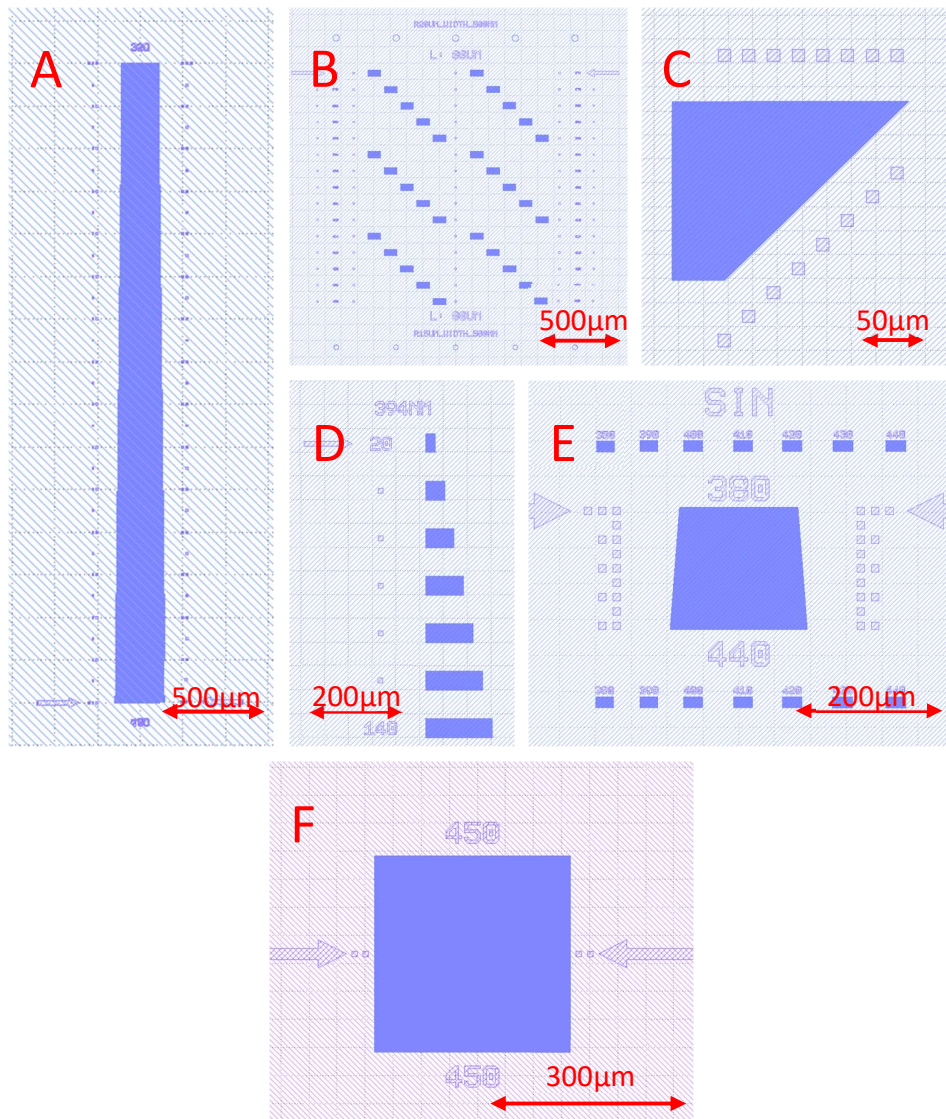


*Fig. 7: Structures A-F in detail. Big arrows are used for alignment and to measure etch depth using the profilometer. Structures C and E were not investigated in this thesis.*

Structure A is a large chirped grating, ranging in period from 350 to 480nm. It is 3mm long and is used for structural sample inspection such as cross-sectional scanning electron microscopy (XSEM). It can be used for optical pumping experiments to obtain a rough estimate for a suitable grating periodicity (Fig. 7A). Structure B is an array of blocks with a discrete period, ranging from 374nm to 430nm in steps of 4nm; the blocks are 40x80µm in size (Fig. 7B). These gratings were studied, but it was discovered their size was too small to target them with a spot. Structure C is a grating of fixed period, but with a continuously varying length (from 42.5µm to 192µm) and a height of 150µm; it exists in the same periods as structure D. It was not used in our investigations

(Fig. 7C). Structure D is an array of gratings with the same period, but differing lengths, ranging from  $20\mu\text{m}$  to  $140\mu\text{m}$ . The structures exist in periods of  $374\text{nm}$ ,  $382\text{nm}$ ,  $386\text{nm}$ ,  $394\text{nm}$ ,  $402\text{nm}$ ,  $406\text{nm}$ ,  $426\text{nm}$ ,  $430\text{nm}$ , and  $434\text{nm}$  (Fig. 7D). Structure E is a short chirped grating, ranging from  $380\text{nm}$  to  $440\text{nm}$  in period. It is  $170\mu\text{m}$  long and around  $170\mu\text{m}$  wide, and accompanied by discrete blocks of different wavelengths, measuring  $30\times 15\mu\text{m}$ . Structure E was also not used in our investigations (Fig. 7E).

MS3 was fabricated using a simpler layout, having only structures A, B, and E as in the first iteration. Additionally, structure F was introduced – a big block of  $300\times 300\mu\text{m}$  of a discrete period from  $396\text{nm}$  to  $430\text{nm}$  in steps of  $4\text{nm}$ , and additionally  $440\text{nm}$  and  $450\text{nm}$  (Fig. 7F). This structure can easily be targeted by a narrow laser spot, without exciting too much of the surrounding bulk material.

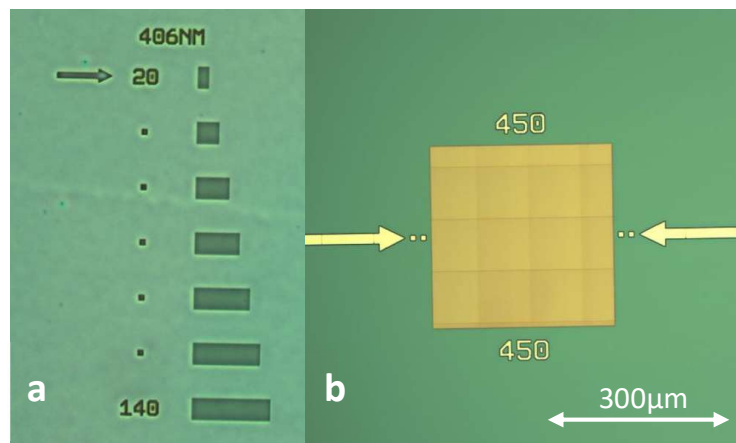


*Fig. 8: Microscope images of structures D imprinted in a sample (a) and structure F after developing of the resist during manufacture (b). In (b) stitching errors can be seen, where the e-beam writing tool had to be realigned.*

Fig. 8 shows microscope images of one structure of type D (a), and one of type F (b) to show how they look in reality. In the type-F structure, square regions can be recognized. The EBL system's area of exposure is limited, so the large pattern is broken down into smaller areas, which are exposed one after the other, making stage translation necessary. Deviations from a perfect alignment of neighboring areas are called stitching errors and become apparent as the faint lines seen in the pattern (stitching errors are also discussed in chapter 5.3).

## 4.8. Simulations

Simulations of the sample stack (substrate, perovskite, grating (incl. parameters) are performed using *Ansys Lumerical* software.

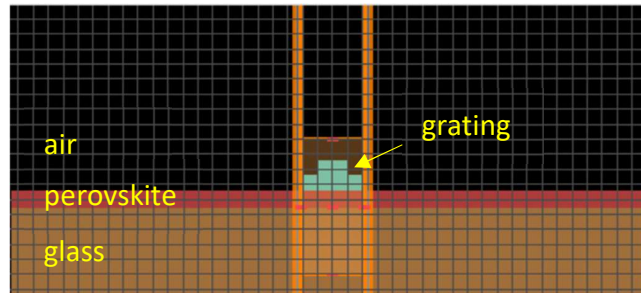


*Fig. 9: Visualization of the simulation stack. The orange vertical lines indicate periodic boundaries, the orange box indicates a finer meshed region. For this image,  $r=h$ ,  $d=0.5$ .*

A simulation stack is created, consisting of 700 $\mu\text{m}$  glass substrate, followed by a variable thickness of perovskite (standard 120nm), and the grating above. For the grating, different parameters, like residual thickness, tooth height, tooth slope, duty cycle, and period are evaluated.

The simulation is set up with periodic boundary conditions on either side of the grating as seen in Fig. 9, and also along the field of view. A broadband light pulse is injected along the vertical axis. Modes within the perovskite or transmission of light above the sample are measured to study the influence of the grating on the light pulse. The stack geometry is iteratively modified according to findings from XSEM analyses.

The eigenmode expansion solver within *Lumerical* is used to calculate  $n_{\text{eff}}$  of the grating and to study the mode overlap between the perovskite and the grating. The simulated data is iteratively incorporated into the sample design (e.g., experiments are conducted to modify the residual NIL layer or the perovskite thickness).

## 4.9. Ellipsometry

For ellipsometry measurements, a *Woollam RC2* ellipsometer was used. Points were measured at three angles (60°, 65°, 70°), and seven points (hexagon and center point) on the sample were measured and averaged to obtain film thickness or (n, k)-values.

Elliptically polarized light is shined on a sample under different angles, and the change in polarization and amplitude after being reflected by the sample is measured. Through fitting, parameters like (n, k) value pairs and layer thicknesses can be extracted.<sup>48</sup>

## 4.10. Optical Measurements

During the experiments, the setup for optical measurements was changed multiple times. Different setups are shown in Fig. 10 and Fig. 11.

In literature, many kinds of input parameters are reported in quantifying light emitters. Energy or energy density, and power or power density are most commonly used. In optical setups, the beam can be modified in many ways, most notably the energy of the beam can be changed, but the beam diameter and the beam shape can be modified as well. It is therefore important to report all three parameters. In our opinion, energy density, also referred to as fluence, is the most reliable reporting parameter. It has a physical meaning and is hard to manipulate in misleading ways. Generating reliable values faces certain problems as no universal standard for assessing the optical beam profile dimensions is accepted in the community.

To study the emission characteristics like spectral distribution, thresholds, angular spread, etc., the emission spectrum of the sample is recorded with the setups outlined in chapters 4.10.3 through 4.10.5.



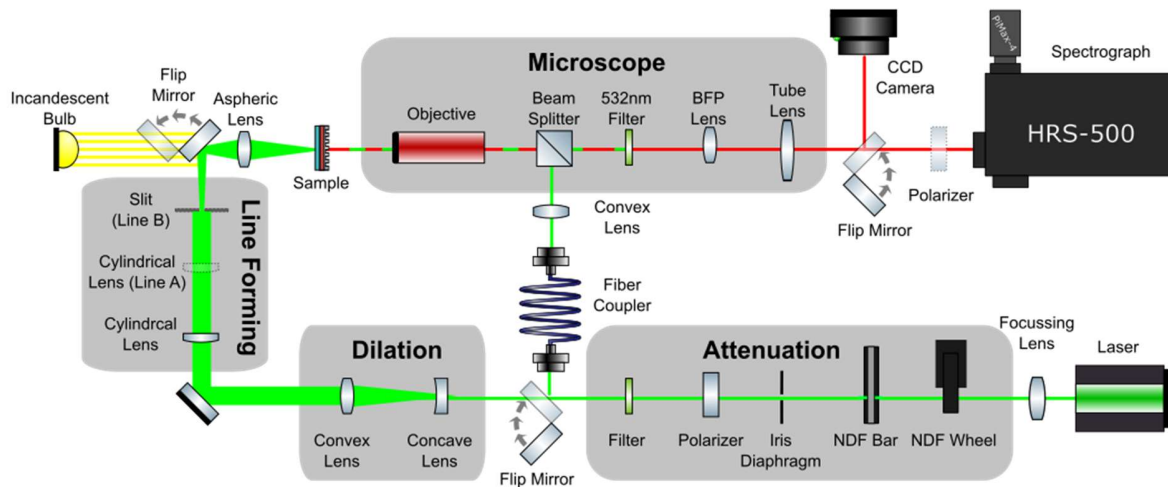


Fig. 10: Visualization of setup for optical investigations with line and spot. For using the spot, the flip mirror between attenuation and dilation was placed in the beam, diverting the beam to the fiber coupler. In the line forming stage, either a second cylindrical lens (setup A) or a slit (setup B) was used. The flip mirror after the line forming could be removed to allow for easy sample alignment using an incandescent bulb and a CCD camera after the microscope section.

#### 4.10.1. Pulse generation

In our setups, a CryLas FTSS 355-300 pulsed laser is utilized. It uses a Nd:YAG source bonded to a saturable Cr:YAG absorber to produce 355nm laser light. The laser also has non-linear optics installed, which allow to convert the nominal 355nm output to 532nm utilizing frequency combination and conversion. An external pulse generator (HP8110A, 150MHz) supplies 20Hz pulses, producing light pulses <math><1.7\text{ns}</math>.

#### 4.10.2. Attenuation

Two sets of adjustable neutral density filters (NDFs) are available: one motorized wheel containing five different NDFs and one empty window, and one translatable bar with five different optical densities (Tab. 10).

Tab. 10: Attenuation of different neutral density filters

position	1	2	3	4	5	6
wheel transmission	100%	97%	52.8%	8.44%	0.567%	0.07%
bar transmission	100%	50%	25%	16%	10%	1%

Additionally, a rotatable wire grid polarizer is placed in the beam path. As the laser source produces inherently linearly polarized light, turning the polarizer allows for almost step-less adjustment of attenuation. The markings of the rotation are spaced by  $2^\circ$ , so the minimum used step is  $1^\circ$ . The resulting attenuation can be calculated using Malus' law, where  $\theta=0$  correlates with the maximum of the transmission:

$$I_{trans} = I_0 * \cos^2(1 - \theta), \quad \text{Eq. 5}$$

Before the polarizer, an iris diaphragm is situated, which can be used to constrict and circularize the beam.

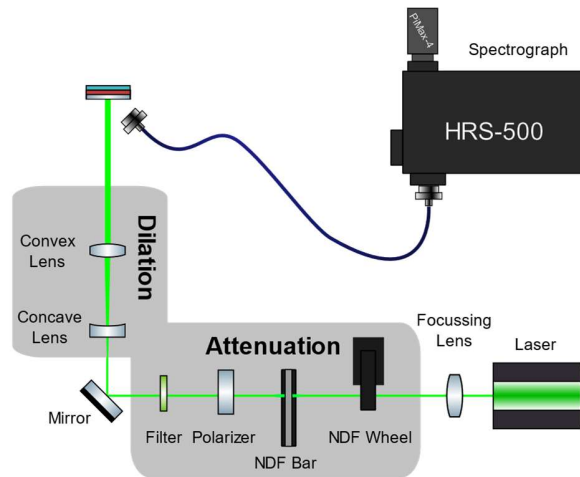


*Fig. 11: Optical setup for data acquisition in backscatter mode. The dilation is kept low. Backscattered light is collected with a glass fiber, located close to the sample under  $45^\circ$ .*

#### 4.10.3. Backscatter Setup

The sample is placed in the beam path after attenuation, using a rather crude sample holder that does not allow for precise enough alignment of the beam to target specific grating areas. A glass fiber angled at around  $45^\circ$  is used to collect backscattered light after hitting the sample. The beam is attenuated and aligned to hit a spot on the sample far away from any gratings. The diffusely scattered light is collected and analyzed with the optical multichannel analyzer (OMA) system. This way, any directional light from lasing or interaction with the grating is removed.

#### 4.10.4. Spot Setup

After passing through the attenuation section, the beam is diverted with a flip mirror and coupled via a glass fiber cable to a 50/50 beam splitter within the microscope cage (cf. Fig. 10). A plano-convex lens is placed in front of the splitter on a translation stage, projecting a spot with changeable size onto the sample. The light reflected by the sample is passed through the microscope and analyzed in the OMA system.

#### 4.10.5. Line Setup

In the line setup, the beam passes through additional optical equipment:

##### Beam expander

One plano-concave ( $f = -30\text{mm}$ ) and one plano-convex lens ( $f = 200\text{mm}$ ) are used to dilate the beam and make it slightly convergent.

##### Line shaping

Two different variants of line generation setups are used – line variant A is used for measurements on samples 1 and 2, whereas line variant B is used for measurements on samples 3, 4, and 5. In both variants, the slightly converging beam is directed at a plano-convex cylindrical lens ( $f = 150\text{mm}$ ), mounted on a translation stage equipped with a stepper motor, and affixed to a mount allowing for rotation of the lens around the axis of light propagation. This way, the light is constricted in one direction, and by moving the lens on the translation stage, the position of the focus spot can be changed. The aspheric projection lens then projects a wider or narrower stripe of light onto the samples. The reason for constricting the pump beam in a stripe-like shape is to prevent the excitation of parasitic lateral ASE modes. Also, when exciting a chirped grating, the line width must not be too high to prevent excitation of grating areas with completely different periods. Other grating features (like structure D) are quite small and line-shaped, so line-like excitation makes sure no surrounding bulk material is excited.

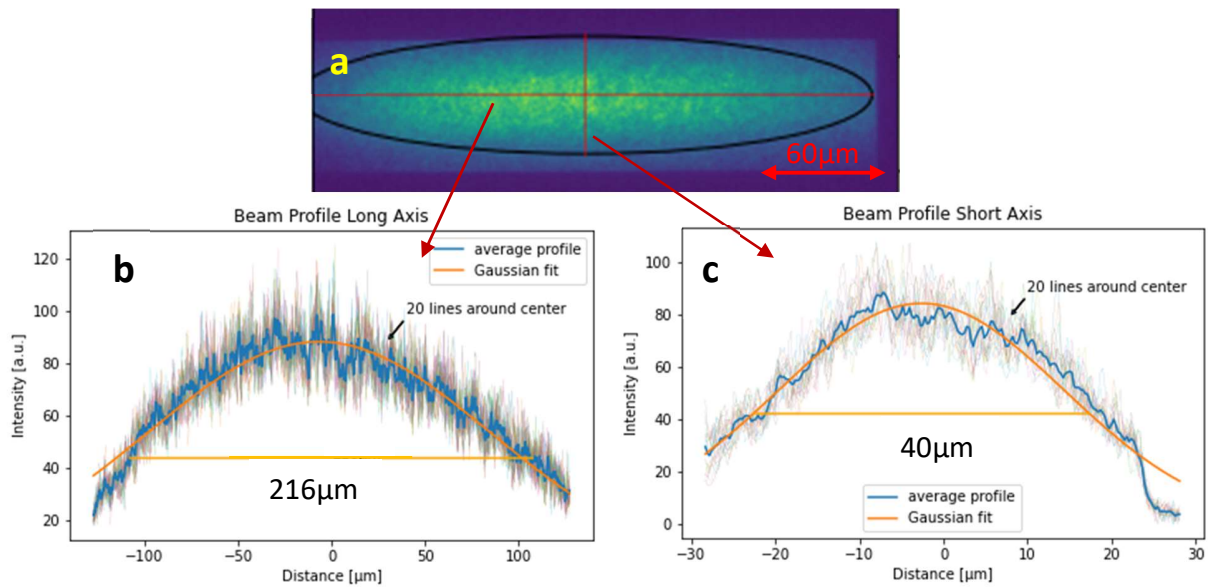


*Fig. 12: Line shape for variant A. (a) shows a 2D image of the line on the sample through the slit of the spectrometer. The two main axes of an ellipse are shown in (b) and (c). 20 lines surrounding the center have been averaged to smoothen noise, and Gaussian beam profiles have been fitted. The FWHM of those profiles is considered when measuring dimensions of the beam.*

In variant A, the beam then passes through another plano-convex cylindrical lens ( $f = 100\text{mm}$ ) constricting the beam in the direction perpendicular to the first one, allowing for changing the line length (although only roughly, and also being coupled to the first cylindrical lens controlling the width of the beam). The lens is mounted on a micrometer-screw-driven translation stage and affixed to a rotation mount. The resulting beam has a Gaussian shape in long and short axis, with FWHM values of around  $200\mu\text{m}$  and  $40\mu\text{m}$ , respectively.

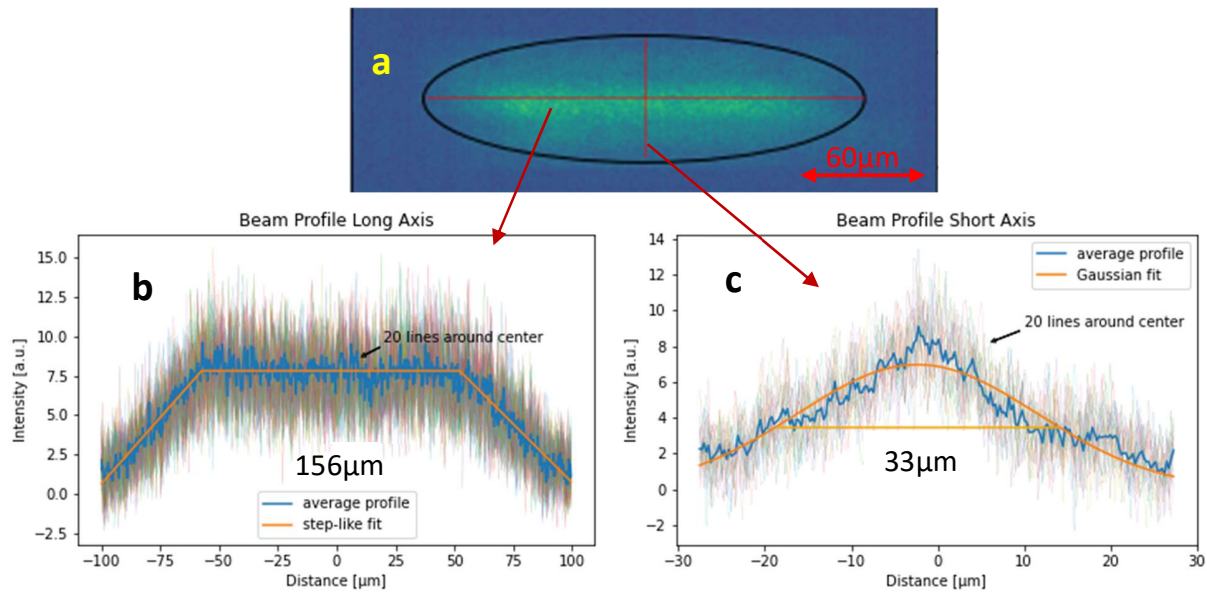


*Fig. 13: Line shape for variant B, with length set to  $\sim 140\mu\text{m}$  by visually overlapping it with a  $140\mu\text{m}$  grating. In (a), a 2D image of the beam recorded with the spectrometer is shown. The main axes through the ellipse used for finding the beam are shown in (b), and (c). 20 lines around the center were averaged to reduce noise. The minor axis was fitted with a Gaussian profile, and the FWHM was calculated. The major axis was fitted with a rectangular step profile with linear slopes. The length is taken as the distance between the two midpoints of the linear slopes. It can be seen that the fitted major axis length of 156 is a bit higher than the targeted value of  $140\mu\text{m}$ .*

In variant B, the beam is instead passed through a mechanical slit, where the line length can be adjusted with a micrometer screw, allowing for more precise and repeatable line length settings. One downside of this setup is that the beam is clipped, so less energy reaches the sample, although the energy density (= fluence) stays constant. The resulting beam has a Gaussian profile of around  $30\mu\text{m}$  FWHM along the short axis, and a rectangular profile with linear slopes along the long axis. The length of the long axis is related to the truncating slit opening.

#### Projection onto the sample

A 150mm focal length aspheric imaging lens is used to project the image of the spot close to its narrowest area onto the sample.

### Power measurement

In the later stages of the experiment, a 70/30 beam splitter is placed in front of the sample stage, allowing for direct monitoring of the energy contained within the spot. An S120VC power sensor was used to record the power of the 30% output beam, while the 70% output beam was directed onto the sample.

### Sample stage

Two different stages are available; one simple translation stage adjustable in x, y, and z coordinates, and one cryostat chamber. The cryostat can be pumped to vacuum (down to  $10^{-7}$ mbar) and cooled to liquid N<sub>2</sub> temperatures, but it was only used for measurements on sample 2. The simpler translation stage provides more flexibility and makes targeting and aligning the sample much easier, thus allowing for the required higher throughput of samples.

### Microscope setup

A 60mm cage system is used to create a microscope to probe the light emitted by our samples. Three objectives are available (Mitutoyo Plan Apo 10x, 50x, 100x) of which 50x was mainly used in this thesis, and 10x was used only for measurements of sample 2. A 200mm focal length infinity-corrected tube lens (TTL200-S8) is used as the ocular lens. Objective and ocular mounts are spaced 9" (22.86cm) apart. On a translatable flip mount between objective and ocular, a back focal plane (BFP) lens ( $f = 150$ mm) is mounted. If flipped into the beam path, it acts as a Bertrand lens, allowing for imaging in the Fourier space. A 50/50 beam splitter cube is mounted behind the objective, allowing the same microscope to be used in combination with the spot setup for reflection imaging, as well as the line setup (cf. Fig. 10) for transmission imaging. The splitter is AR-coated to reflect pump light, which might damage the spectrometer. It is imperative to prevent high-energy pump light from entering the spectral analyzer, so an additional filter absorbing 532nm light is placed in the beam path.

### Output Polarizer

Additionally, a second wire grid polarizer can be placed after the microscope, allowing to analyze the polarization of the emitted light.

### CCD Camera

To be able to adjust the sample and beam properly, a charge-coupled device (CCD) camera (IDS U3-3682XLE-M) can be used to image the sample through the microscope system. The camera can be placed in the optical path via a flip mirror, and records images in greyscale. It is used for focusing and positioning (in which case an incandescent lamp is used to illuminate the sample), to perform some of the measurements, namely to record the far-field pattern of the gratings. It has a wider field of view than the spectral analyzer, which is limited by the slit width.

### **4.10.6. Optical Multichannel Analyzer (OMA) System**

A *Princeton Instruments SpectraPro 500 HRS* is used as a spectral analyzer, and data are recorded using a *PI-MAX 4 1024x1024* sensor. The analyzer has two entrance ports: on the side port, the backscatter collecting fiber is coupled in via a fiber coupler equipped with a manually adjustable slit; on the front port, a motorized slit is used to allow the light from the microscope to enter the system. Two turrets with three gratings each are available, their specifications are listed in Tab. 11. Only gratings from one turret were used (500nm blaze – 150, 300, and 1200g/mm).

The 2D nature of the sensor allows for different analysis modes: Spectra can be collected along the x-axis of the sensor, while the y-axis preserves the physical dimension of the sample. Also, the slit can be opened to record a real image of the analyzed area. Both modes can also be transformed into Fourier space using a back-focal plane lens incorporated in the microscope cage. Either full 2D images can be recorded, or a region of interest in a 2D area of the sensor can be selected and binned to create a 1D graph.

Tab. 11: Optical gratings available within the spectrometer

line density [g/mm]	blaze [nm]
1200	500
300	500
150	500
1800	670
600	750
150	800

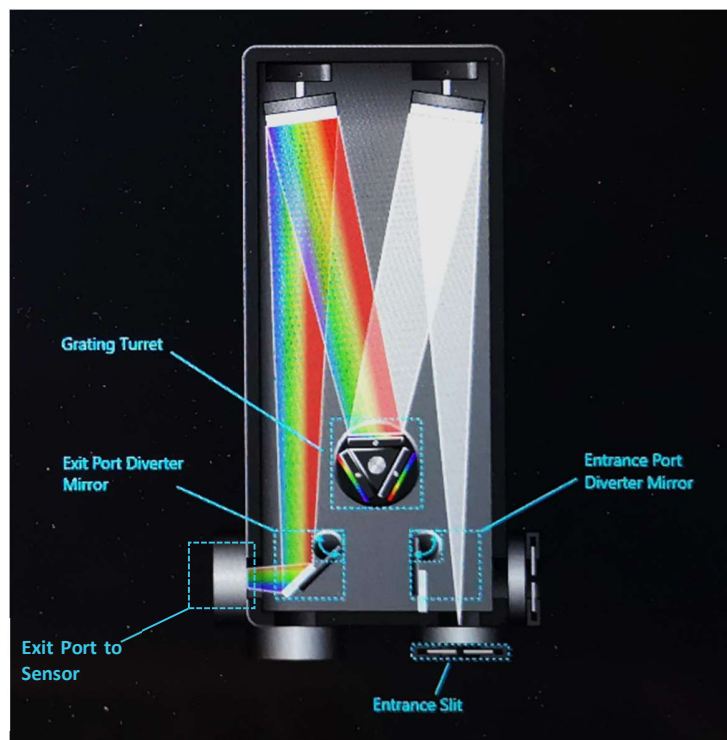


Fig. 14: Schematic view of the light path within the spectrometer. Adapted after schematic within Princeton Instruments' "LightField" software.



#### 4.11. Analysis of Optical Measurements

Different types of data are collected using the multispectral analyzer. The data processing and preparation shall be discussed here. Image processing was done in *python* with custom code.

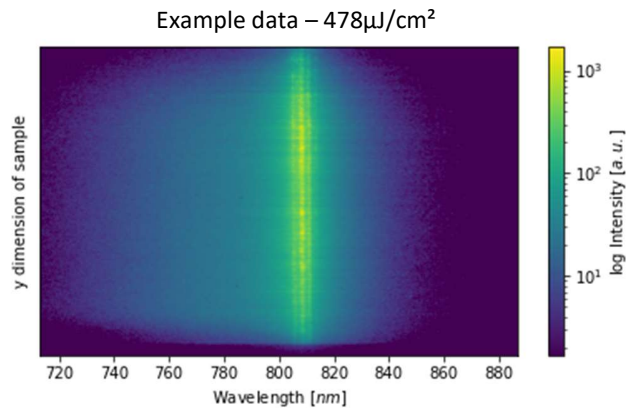


Fig. 15: 2D spectral image. The x-axis shows wavelength, the y-axis the position of emission on the sample. The color according to the color bar represents the recorded intensity.

The 2D spectral images are what the sensor records in spectral mode. The x-axis shows the wavelength of the light, the y-axis is a spatial axis and therefore shows where on the sample the light originated from. One can see whether the emission is uniform over the whole area. In this particular case, bright spots appear. Grating action can be assessed as gratings tend to amplify the light that hits them more than bulk areas and appear brighter on the spatial ordinate. The intensity is displayed on a logarithmic scale. The colormap for 2D images is centered around green, making it easier for the human eye to contrast the differences.

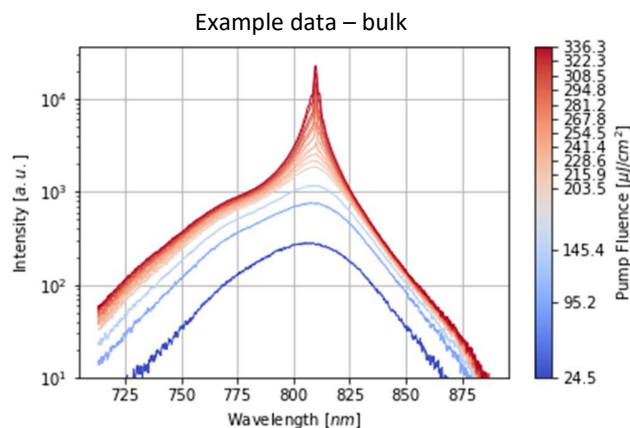


Fig. 16: 1D spectrum. Spectra recorded on the same grating structure are overlaid, while colors represent the fluence at which the spectra were recorded. The y-axis is logarithmic.

The 1D spectra are related to the 2D variant, in that a region of interest (ROI) is defined in the center of the sensor. The data in the ROI is binned to create a 1D graph, as seen in Fig. 16. Spectra of different excitation fluences are overlaid in a logarithmic plot, the color bar on the right gives the corresponding fluences for each spectrum. These plots can be used to visually estimate thresholds (by looking at what fluence a peak appears), and to judge peak shape, width, and possible multiplicity. The spectra can be recorded using three spectrometer gratings ('regular' – 150g/mm, 'fine' – 300g/mm, 'finest' – 1200g/mm), yielding different amounts of resolution to the spectrum.

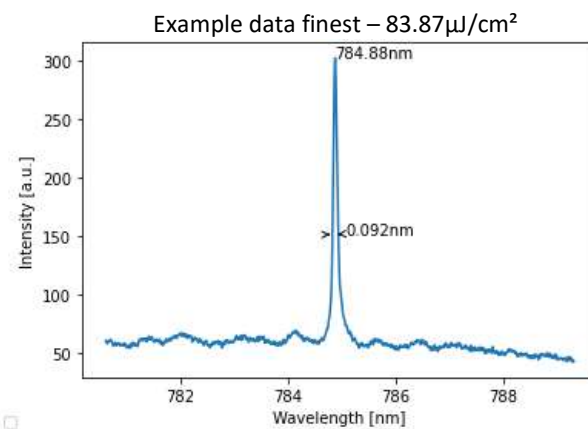


Fig. 17: Spectrum with peak position and FWHM. This spectrum was recorded using the 1200g/mm grating of the spectrometer. A peak finding algorithm gives the peak position and FWHM.

If one takes a single spectrum, a peak detection algorithm can calculate the peak width (FWHM), as is displayed in Fig. 17.

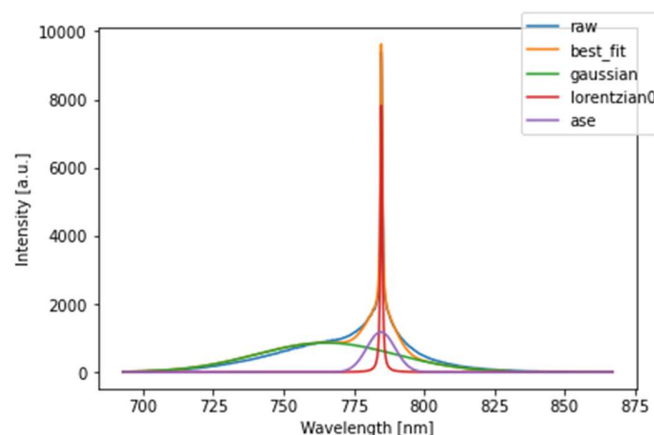


Fig. 18 Peaks fitted to spectrum. Green shows the Gaussian peak representing SE, purple shows the signal coming from ASE. Red indicates a Lorentzian lasing (or RL) peak. The blue curve shows the raw data, while yellow combines all fitted peaks together.

This becomes more difficult if multiple peaks or an ASE signal are present in the spectrum. For that reason, different peaks are fitted to the spectrum: a Gaussian peak captures SE, Lorentzian peaks are used to fit ASE (if present) and lasing. The fitted peaks are not used to calculate the threshold, but the FWHM of the highest peak for each threshold is shown in intensity-FWHM plots (cf. Fig. 19, Fig. 20). Peak height is used for polarization measurements.

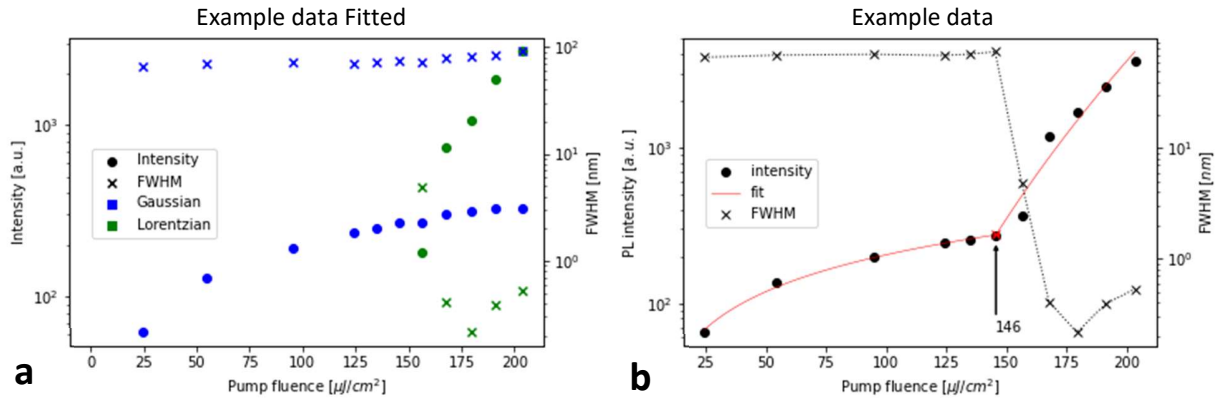


Fig. 19: Intensity-FWHM plots. (a) shows the values generated from fitting, (b) shows the highest intensity, FWHM of the highest respective peak in (a), and a two-piece linear function fitted to the intensities in double logarithmic scale. The intersection of those two lines is marked as the threshold. Due to the x-scale being linear (for easier comprehension), the two lines appear curved.

The results of the fit are visualized in Fig. 19a. In Fig. 19b, the maximum intensity and the FWHM of the highest peak are shown. The red fit line consists of two linear functions and a variable intersection point that is fitted to the log-log version of the data. It is visualized with the x-axis in linear scale, for easier comprehension. The intersection point is taken as the threshold value for the measurement. Sometimes, intensity values tend to approach a plateau at higher fluences, which leads to the right line having a slightly lower slope. This may lead to the two lines intersecting at lower values, and can thus culminate in an underestimation of the threshold.

The issue of clear threshold detection is very topical in the community. A review paper by *Milanese et al.* highlighted how many different methods are currently used, ranging from visual inspection over slope comparison to reporting no thresholds at all.<sup>49</sup> They found that taking the point at which the FWHM starts to decrease gives the most accurate threshold values, while other methods like slope comparison tend to overestimate<sup>50</sup>. In this thesis, slope comparison is mainly used, supported by visual inspection and FWHM. Slope comparison is robust, easy to understand

for readers, and quick to implement. This is the case especially in combination with FWHM and visual inspection to explain any anomalies.

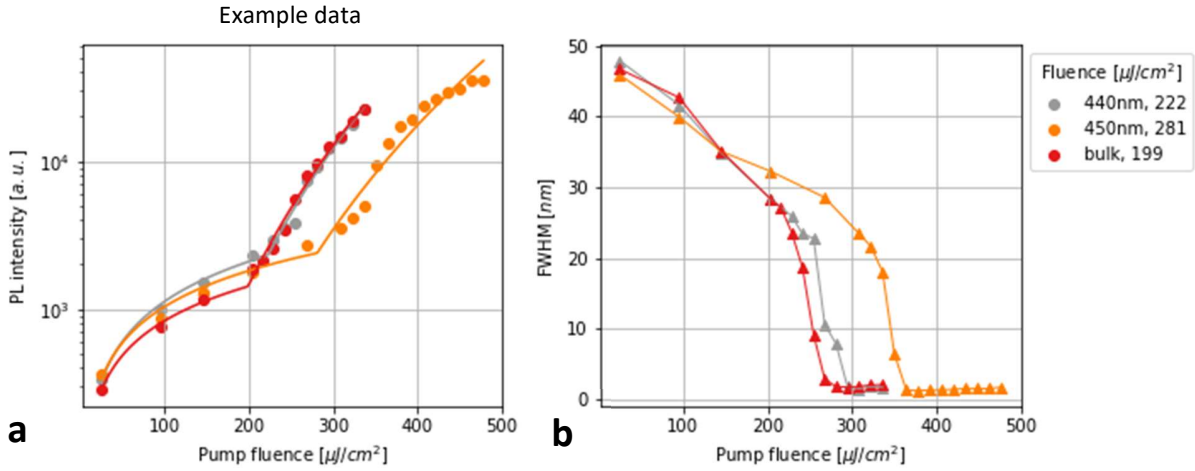


Fig. 20: Multiple intensity-FWHM plots. For easier reading, (a) shows intensities, (b) FWHM. The y-scale in (b) is linear, while in (a) it is logarithmic.

If multiple measurements should be compared, the intensity and FWHM curves can be visualized as in Fig. 20. For easier reading, the intensity and FWHM are shown in separate plots.

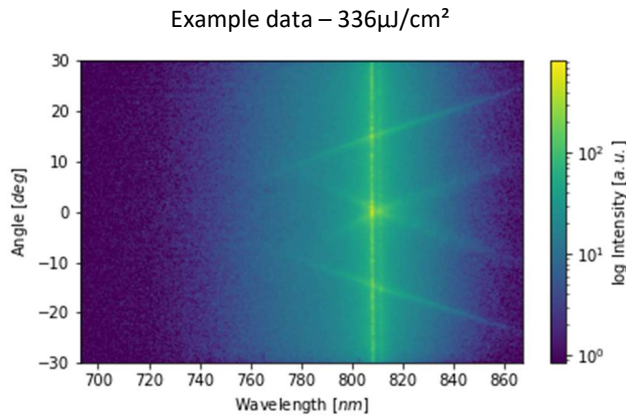
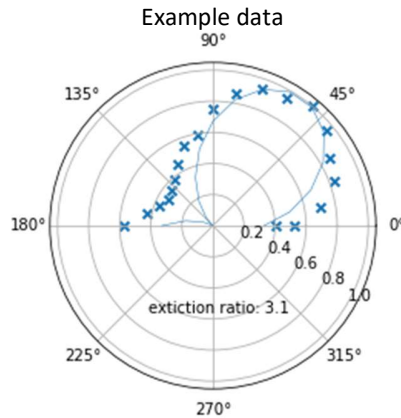


Fig. 21: Angular spectrum. The color scale shows the intensity in log scale. Forward and backward propagating modes within the studied structure can be seen as slanted lines. Vertical lines indicate the gain band of the material (the wavelength region in which light is amplified).

Angular spectra can be very useful in determining emission mechanisms. Here, the BFP lens is used (cf. Fig. 10) to transform the image into Fourier space. The y-axis then shows the angles under which the light is emitted from the sample, with the x-axis still showing the wavelength. The image can be understood as a photonic band structure (cf. chapter 3.1.3). Sloped

lines indicate forward and backward propagating modes within the resonator (cf. Eq. 3). If the grating period changes, so does the position of the sloped lines. Vertical lines indicate emission without angular dependence, characteristic of SE and ASE in our samples. Lasing should occur if the mode crossing lies in the optimal gain region. If a bright spot appears close to the crossing, it is a good indication that lasing takes place.<sup>28,29</sup>



*Fig. 22: Polarization plot. The points correspond to the peak height normalized to the maximum intensity. On the polar axis, the rotation of the polarizer is plotted. The extinction ratio (highest value/lowest value) is stated as well.*

If the polarization of the output beam should be analyzed, the fluence is kept the same while a polarizer in front of the spectrometer (cf. Fig. 10) is rotated and the change in intensity is recorded. The height of the Lorentzian peak fitted to those spectra (normalized to the highest peak) is plotted vs. the rotation angle of the polarizer. The extinction ratio is calculated as the ratio of intensity of the highest vs. the lowest peak. A  $\cos^2$  trend (which would be expected for perfectly polarized light) is shown with a fine blue line. Due to imperfections in the polarizer, only 180° of the polarization was measured.

The far-field image is a 2D Fourier image of the emission beam (with the BFP lens in the beam path). It can be recorded with the spectrometer (with its slit fully open) or with the CCD camera (cf. Fig. 10). A 1D DFB structure creates circular emission patterns in the far-field, which are spaced by  $2\pi\Lambda$  apart. The bent lines seen in Fig. 23 are sections of those circular patterns, characteristic of DFB lasing.<sup>51</sup> No scales are given for far-field images, since calibration is very difficult, and only the pattern is studied, not any features.

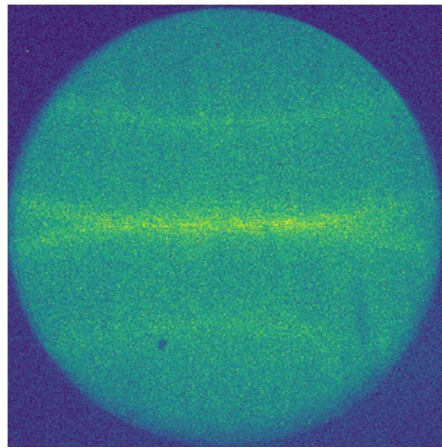


*Fig. 23: Far-field image, recorded via the CCD camera. The circular appearance is due to the mirror that diverts the image to the sensor. Curved lines correspond to emission features generated by a grating. The image is taken in  $k$ -space.*

## 5. Results

### 5.1. Simulations

Grating period, duty cycle, residual layer thickness, and tooth angle are varied and results analyzed. The transmission spectrum is analyzed. Dips in the spectrum indicate that light of that wavelength interacts with the structure in the form of resonance.

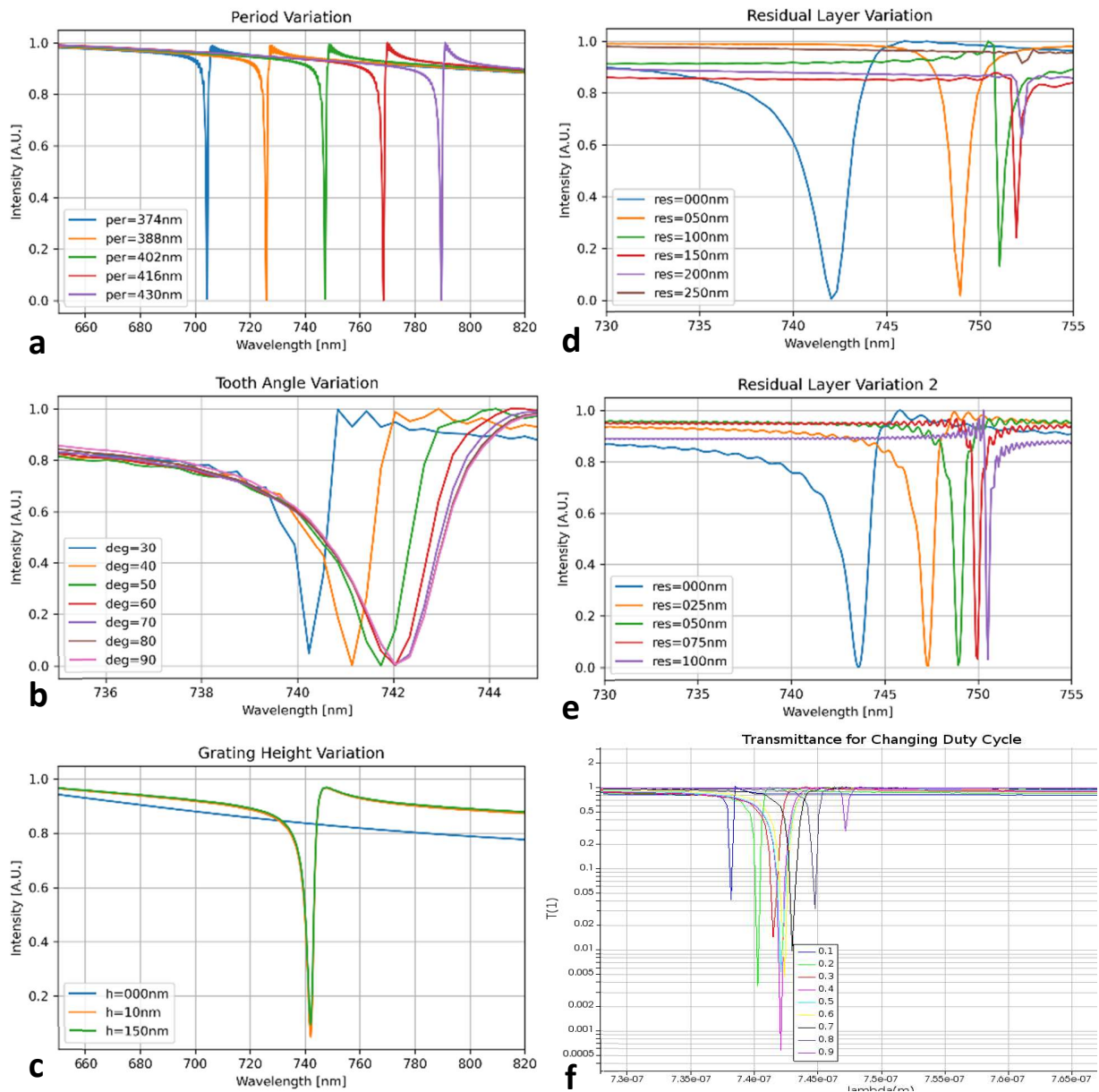
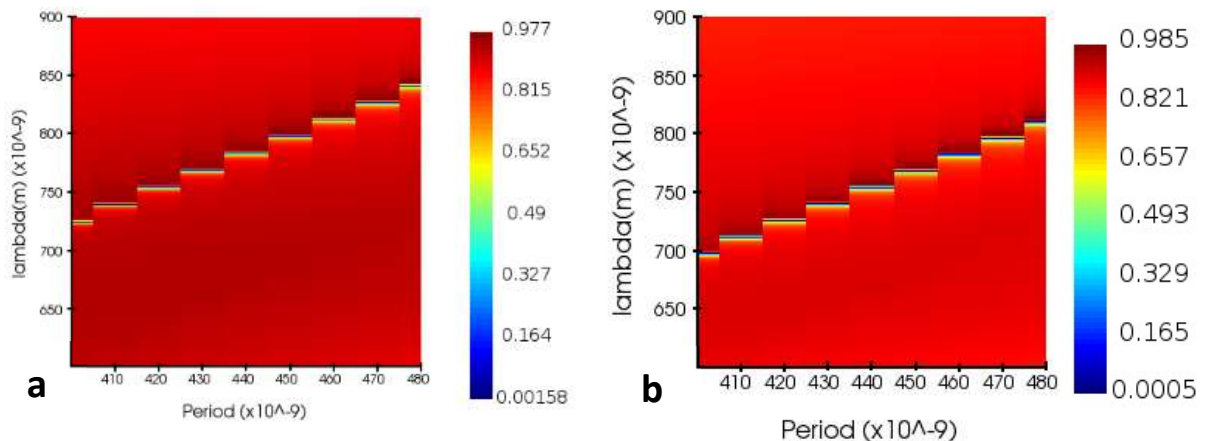


Fig. 24: Results of different parameter studies simulated in Ansys Lumerical. Shown are the transmittance spectra for (a) period, (b) tooth angle, (c) tooth height, (d) and (e) residual layer, and (f) duty cycle variation.

For changes of the period, a clear linear shift as expected by Bragg's law can be seen. For this simulation, the duty cycle was fixed at 0.5, tooth height at 100nm, residual layer at 25nm, angle at 85°, and  $n=1.4$  was assumed. Two residual layer simulations were performed, the first with parameters  $h=100\text{nm}$ ,  $\Lambda=400\text{nm}$ ,  $\alpha=90^\circ$ ,  $n=1.4$ ,  $d=0.5$ ; the second with  $h=100\text{nm}$ ,  $\Lambda=402\text{nm}$ ,  $\alpha=85^\circ$ ,  $n=1.4$ ,  $d=0.5$ . It can be observed that for higher residual layers, the resonance peaks obtain a redshift towards higher wavelengths and also show a decrease in resonance height (which tends to be negligible if the residual layer thickness is below 100nm). A variation of the tooth angle shows negligible effect up to an angle of 60° (other parameter settings for this case:  $h=100\text{nm}$ ,  $\Lambda=400\text{nm}$ ,  $d=0.5$ ,  $r=0\text{nm}$ ). Lower angles result in a blueshift. The decreased height of the 30° curve is related to the fact that at a 30° slope, the tooth becomes triangular. If the grating height is varied, it can be seen that there is no strong influence on either peak position or peak height as soon as a grating is present ( $h>0\text{nm}$ ). If the duty cycle is changed, there is a peak shift to the left for lower values, and to the right for higher values. The highest resonance response can be found for a duty cycle of 0.4. The peak height does not straightforwardly correlate with the duty cycle.



*Fig. 25: Sweeps varying the period (x axis), recorded is the transmission spectrum – wavelength shown on y axis, intensity through color. (a) shows the resonance frequencies of an optimized grating geometry for an 80nm active layer, while (b) shows the same results for 100nm active layer.*

Sweeps can be performed where the period is varied and the response is plotted against the wavelength in a 2D plot. Those plots were used to identify which grating period would most likely show resonance for our grating. This avoids time-consuming trial and error in the lab.



*Tab. 12: Parameter influence on mode coupling between active layer and grating*

active layer [nm]	residual layer [nm]	tooth height [nm]	% change
120	35	80	0%
120	10	80	-9%
120	10	100	-2%
120	10	120	4%
120	35	100	5%
120	35	120	8%
100	10	80	12%
100	10	100	22%
100	10	120	29%
100	35	80	-29%
100	35	100	-22%
100	35	120	-18%
80	10	80	35%
80	10	100	49%
80	10	120	60%
80	35	80	-10%
80	35	100	-21%
80	35	120	7%
70	10	120	75%
60	10	120	90%

The subset of these data excluding active layer thickness of 60nm and 70nm can be treated as a full-factorial design of experiment (DOE) with three factors, two with three and one with two levels. Analyzing the response box plots, it becomes apparent that having a thicker residual layer is detrimental to mode coupling between active layer and grating. Reduced active layer thickness also shows a positive effect on mode coupling. The tooth height does have some influence, but it is limited compared to the other two factors. An optimization within the given parameter space shows that the best response is obtained by the following combination: active layer 80nm, residual layer 10nm, tooth height 120nm. From Tab. 12 it can be seen that further decreasing the active layer thickness would further improve mode coupling.

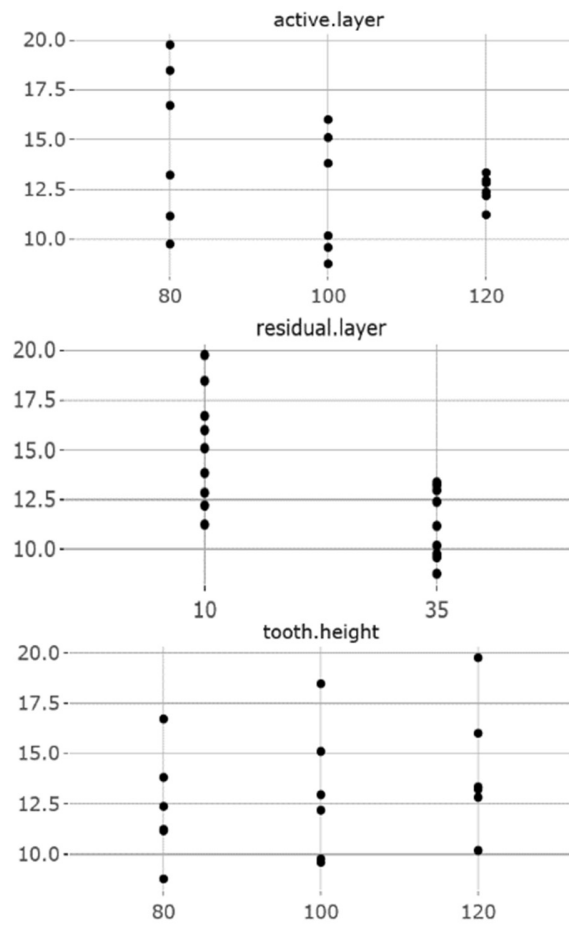


*Fig. 26: Response box plots for the DOE within Tab. 12. Responses are grouped by levels of the factors (active layer, residual layer and tooth height).*

## 5.2. Ellipsometry

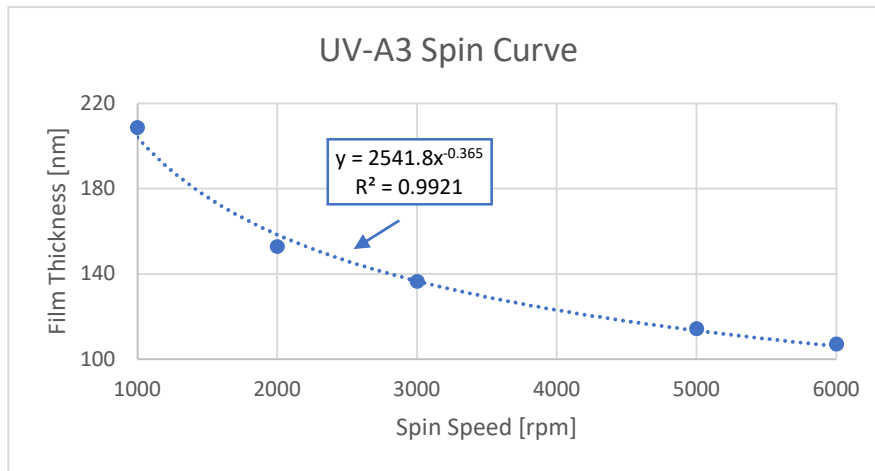


Fig. 27: Spin curve for UV-A3. Power law fit according to Eq. 4.

To evaluate how thick the UV-NIL layer is before imprint, bare Si wafers are coated with adhesion promotor Prim K (standard procedure) and UV-A3, which is spin-coated at variable spin speeds. The film thickness is measured via ellipsometry on seven points of the sample and averaged. The spin curve of UV-A3 shows a thickness of 136nm at 3000rpm, which is the spin speed usually used. Additionally, the refractive index  $n$  is evaluated as 1.50 for light of wavelength 780nm.

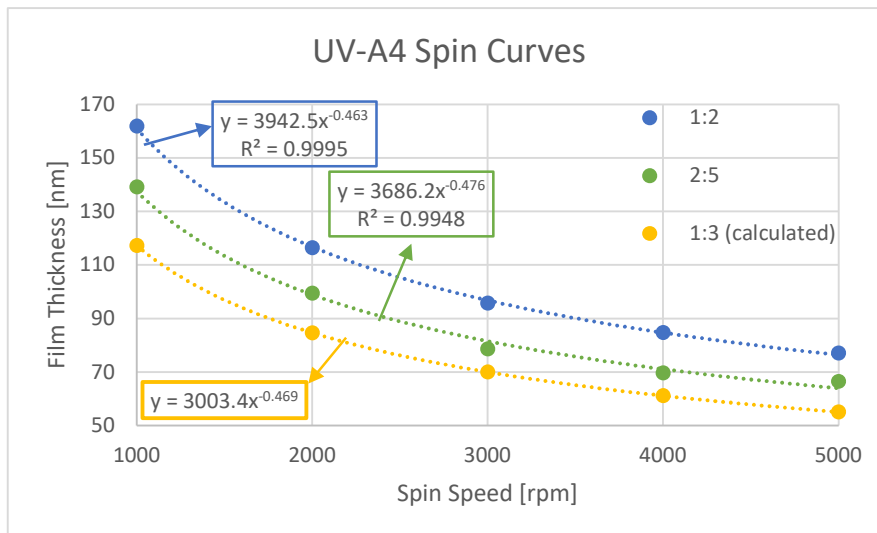


Fig. 28: Spin curves for different dilutions of UV-A4 with PGMEA. The yellow line was calculated through averaging exponents  $b$  and extrapolating prefactor  $K$ . (cf. Eq. 4)

Towards the end of the experiments, the previously used UV-A3 resin stock was depleted and could only be replaced with UV-A4 from the same company. This resin has slightly different rheological and optical properties, which are explored via ellipsometry. The resin UV-A4 is used only for sample 3.

Bare Si wafers are spin-coated with Prim K (standard procedure) and UV-NIL resin (UV-A4, *EVG Group GmbH*), which is diluted 1:2 and 2:5 with PGMEA. Those dilutions are then spin-coated with spin speeds from 1000 to 5000rpm. The film thickness is measured via ellipsometry on seven points on each sample and averaged. The goal of this study is to reduce the residual layer that was observed in XSEM images, and hopefully to improve grating coupling. For that purpose, an initial film thickness of 70nm before imprint is targeted. From the two recorded dilutions, the exponent  $b$  is averaged, and  $K$  was extrapolated linearly. This way, the yellow curve for a 1:3 dilution was calculated, showing a thickness of 70nm at a spin speed of 3000rpm.

### 5.3. Cross-Sectional Scanning Electron Microscopy

#### 5.3.1. Master Stamp 1

After the first stamp was lost due to breaking during NIL lamination, it was decided to sacrifice it and prepare it for cross-sectional scanning electron microscopy (XSEM). The wafer is cleaved perpendicular to the large chirped grating (structure A), to investigate periodicity, uniformity, and etch depth of the gratings.

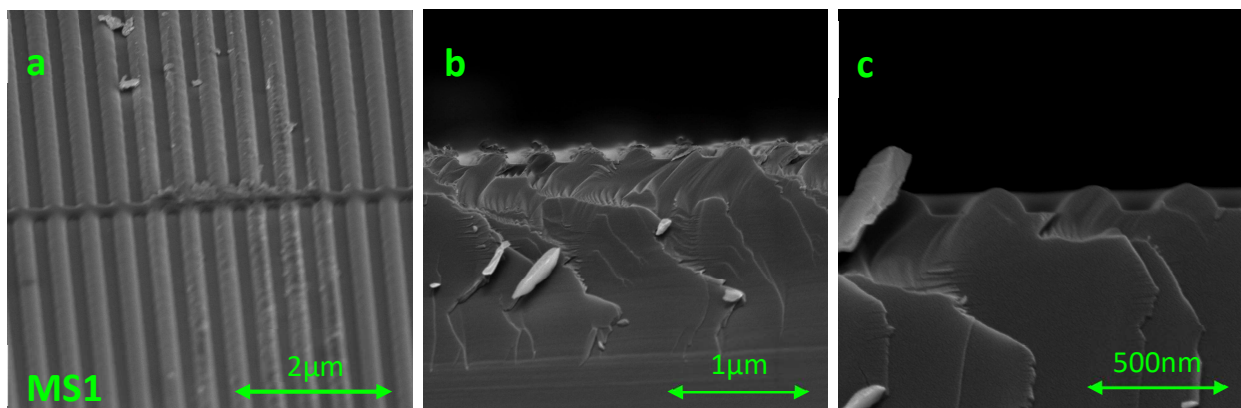


*Fig. 29: XSEM of master stamp 1. (a) shows the grating in top view; dirt is observed in the top of the picture. Across the middle, a stitching error is present (cf. Fig. 8b). (b) shows the tilted view. Chipping can be observed in the cleavage plane. The profile is shown in detail in (c).*

XSEM investigations are carried out using a *FEI Nova 200* scanning electron microscope. The accelerating voltage is set at 5kV, the working distance at 4.6mm. A thermoluminescence detector (TLD) is used for imaging.

Generous amounts of dirt are seen on the stamp, even after rigorous cleaning with ACE and IPA. This could be explained by the extended use of the working stamp materials. Most notably, the etch profile is somewhat lacking, as a vertical and uniform grating would be expected. There are no flat tops present and the profile seems to differ between neighboring ridges. The valleys of the structure are flat. The periodicity is still preserved and the structure should function as a grating. A duty cycle cannot be determined in the same way as it would be possible for a vertical structure, but if the width is measured around half of the height of the peaks, a duty cycle of around 65% can be estimated.

Lastly, the depth of the trenches is around 70-80nm, although a depth larger than 100nm would be preferred to produce a stronger coupling between the resulting grating and the perovskite layer.

### 5.3.2. Etch Improvement

During XSEM investigations of the previously destroyed MS1, it was discovered that the etch profile is not as vertical as expected, and also somewhat irregular, which might impact the grating performance as a resonator. It was therefore decided to try different etch recipes to improve the etch profile.

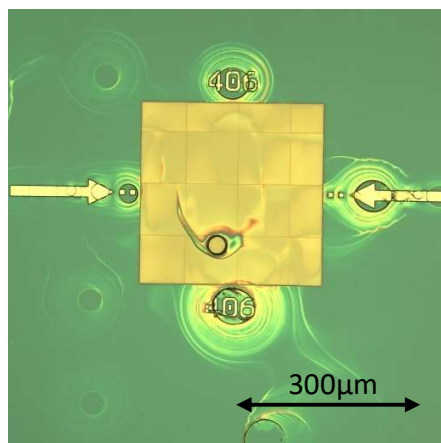


*Fig. 30: Failed development of a prospective MS. Drying patterns can be occur around features.*

Operator error led to one additional MS being lost during the development step. The wafer was not transferred from the developer to the development-stop reagent quickly enough, so drying marks formed on the PMMA surface, especially covering critical areas like the big chirped grating, as some developer would specifically attach there. It was decided to sacrifice this stamp too, and to use it for testing different etch recipes to refine the MS etch.

The stamp is cleaved into four pieces, each containing some sort of grating structure along one of its edges. Etching is done using an *Oxford PlasmaLab 100* tool. Seven different sets of parameters as indicated in Tab. 13 are tried. It can be preemptively noted that variations 5, 6, and 7 do not produce a stable plasma and are therefore not further pursued.

Tab. 13: Etch parameter variations

	SF <sub>6</sub> [sccm]	C <sub>4</sub> F <sub>8</sub> [sccm]	N <sub>2</sub> [sccm]	CF <sub>4</sub> [sccm]	ICP [W]	RF [W]
baseline	6	45	8	0	300	100
variation 1	6	55	8	0	300	100
variation 2	6	45	16	0	300	100
variation 3	12	45	8	0	300	100
variation 4	24	60	0	27	200	100
variation 5	6	70	8	0	300	100
variation 6	6	45	8	0	300	50
variation 7	24	60	0	27	950	15

Since etch speed is a function of multiple variables like pattern density or etch gas concentrations, and as there are also tool-specific influences, it is easiest to calibrate the etch speed empirically. Maximum etch time is calculated using spare pieces of Si covered with ~300nm of PMMA, similar to the stamps. A scratch is introduced to the surface using plastic forceps, and film thickness is measured using a single-spot ellipsometer as well as a *Dektak* profilometer across the scratch. A short etch is done using the recipes as listed in Tab. 13. After around 30s, the Si

piece is removed, and the PMMA thickness is remeasured with ellipsometer and profilometer. From the thickness difference, the etch rate is calculated. A maximum etch time is calculated, so that a minimal residue of PMMA would remain on the surface, resulting in maximum etch depth without over-etch, which can cause pattern degradation. After etching, the residual PMMA layer is measured with ellipsometry and profilometry, and etch depth is verified using the profilometer alone.

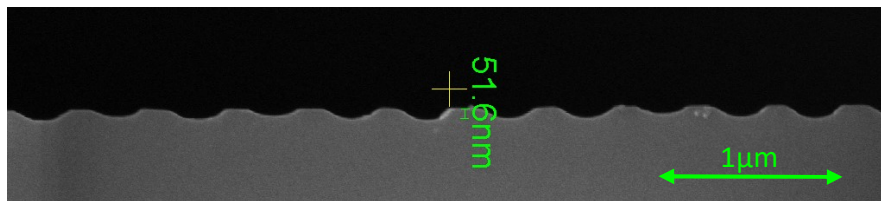


*Fig. 31: Etch variation 1. The profile depth is lower, and slope angles are higher than the baseline. There is a plateau at the top of the teeth.*

As can be seen in Fig. 31, variation 1 produces shallower, more rounded features than the baseline (cf. Fig. 29). Profilometer and ellipsometer readings indicate minimal to no (<1nm) residual PMMA, meaning over-etch might have occurred.

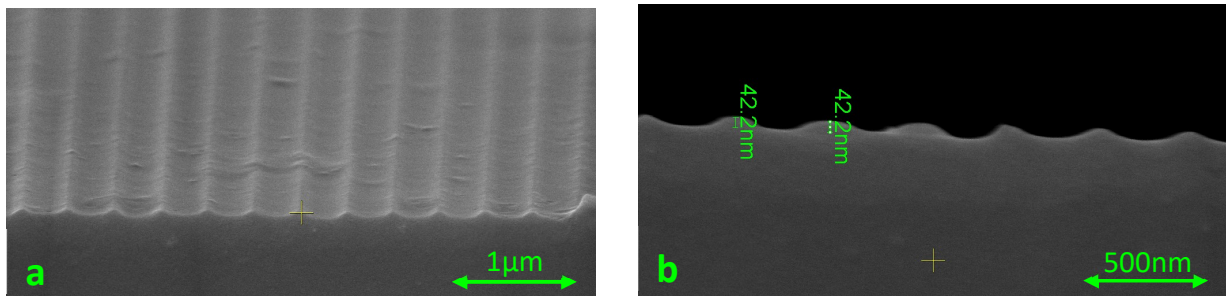


*Fig. 32: Etch variation 2. Profile depth is even less, and features look triangular, with circle-segment-like valleys. (a) shows a tilted view, (b) shows the profile in projection (-4°).*

Variation 2 shows even less pronounced features, indicating isotropic etching. Profilometer readings indicate around 35nm of resist remaining.

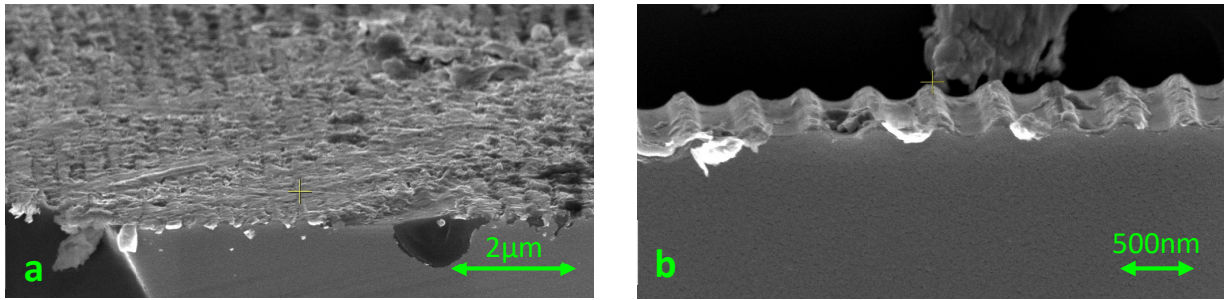


*Fig. 34: Etch variation 3. The sample was dropped and contaminated with dirt by touching a surface and/or tweezer tips. The profile can be seen in (b): Trench valleys show some rounding, the tooth profile appears similar to the baseline (cf. Fig. 29).*

Images of variation 3 show a dirty substrate, owing to bad sample handling and contamination after dropping the sample. Underneath, it can be seen though that the etch profile appears similar to the baseline. No measurement of etch depth was possible in this case. The ellipsometer shows around 40nm of PMMA remaining, profilometer measurements were not possible.

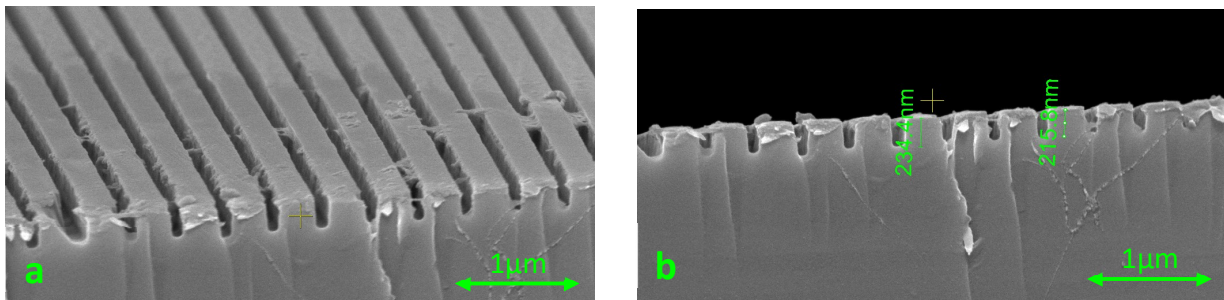


*Fig. 33: Etch variation 4. High trench depth and uniformity can be seen.*

Variation 4 shows the most promising results: very uniform, narrow trenches, flat tops, and an exceptionally high depth of around 200nm. The trenches are narrower than in the baseline etch, which alters the duty cycle. ~75% instead of ~65% as for the baseline is observed. Overall, this profile looks much more appealing and should be further pursued in future studies. The tilted view also shows a high level of uniformity, although some dirt close to the cleavage site can be seen. Only 80nm of PMMA were removed, 210nm remained, indicating the possibility for much deeper etching.



### 5.3.3. Working Stamp Comparisons

XSEM was performed on multiple samples imprinted using different working stamp materials. The UV-NIL layer was cured at different times and temperatures according to Tab. 14:

Tab. 14: Curing parameters for working stamp XSEM comparison

	PS40 @70°C	PS40 @120°C	PS90	PS380
adhesion promotor	Prim K	Prim K	Prim K	Prim K
curing T [°C]	70	120	70	70
curing time [min]	5	2	5	5

Samples were not prepared on glass substrates as described above, but rather on Si substrates with thermally grown SiO<sub>2</sub> to facilitate cleavage. The UV-NIL resin was spin-coated directly onto the bare substrate without any active layer present. The process (cf. chapter 4.5) remained the same otherwise.

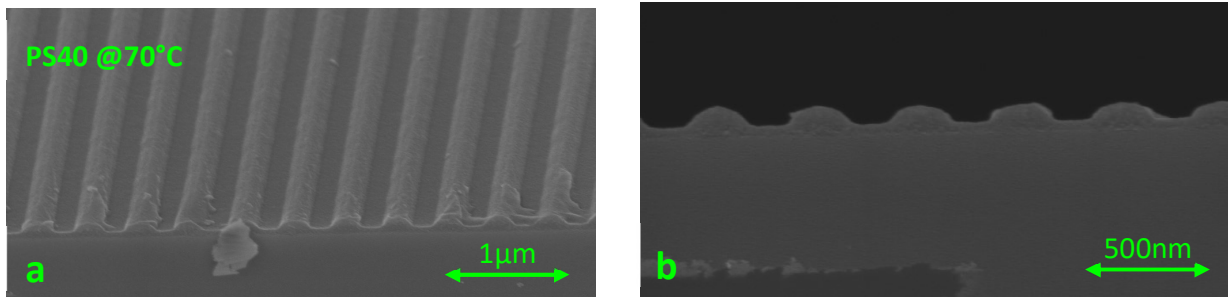


Fig. 35: Imprint of PS40 annealed at 70°C for 5min. Features appear rounded, residual layer is around 40nm while tooth height (measurement - residual layer) is around 80nm. Valleys appear flat. (a) shows the grating in top view, (b) in profile.

The softest working stamp baked at lower temperatures showed significant feature rounding compared to the master stamp. The trench depth reaches the expectations of the master. A significant residual layer of around 40nm thickness can be observed. It is hard to estimate a duty cycle for this geometry of features. If measurements are taken approximately at half of the height of the peaks, around 70% duty cycle is measured.

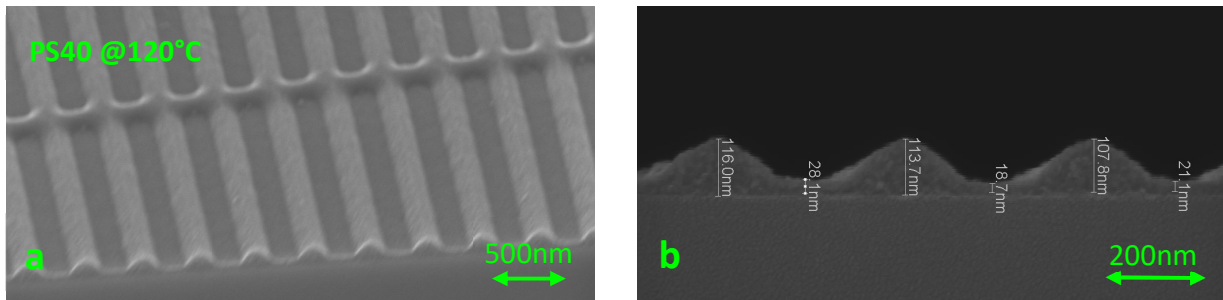


Fig. 37: Imprint of PS40 annealed at 120°C for 1min. The features appear more triangular, residual layer is lower at ~20nm, tooth height is ~90nm. A stitching error can again be seen in (a), which shows the grating in top view, while (b) shows the grating in profile.

If the same working stamp material is annealed at higher temperatures, feature rounding is less pronounced. Triangular-like periodic structures can be seen, heights are as expected. The residual layer is less pronounced at ~25nm. The duty cycle is ~65%.

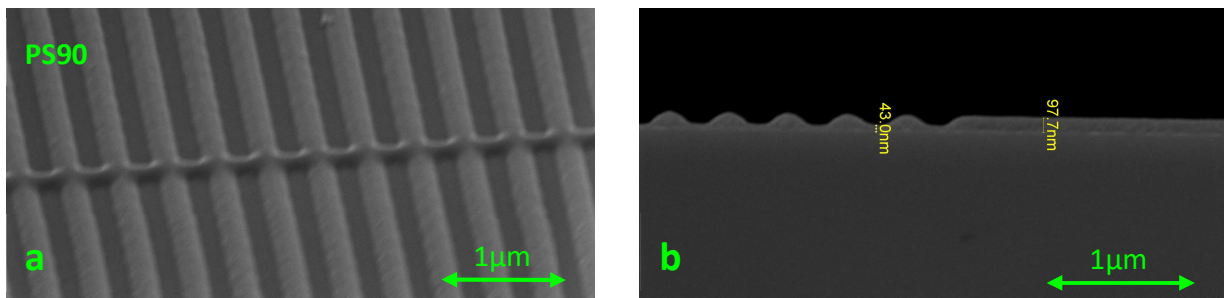


Fig. 36: Imprint of PS90 annealed at 70°C for 5min. The residual layer is ~35nm (measurements not in image), while the unimprinted layer thickness amounts to ~100nm. (a) top view, (b) profile view.

PS90 also shows decent replication quality. With around 35nm, the residual layer is significant. Measurements outside the grating area indicate an initial thickness of around 100nm before imprint. Duty cycle amounts roughly to 70%.

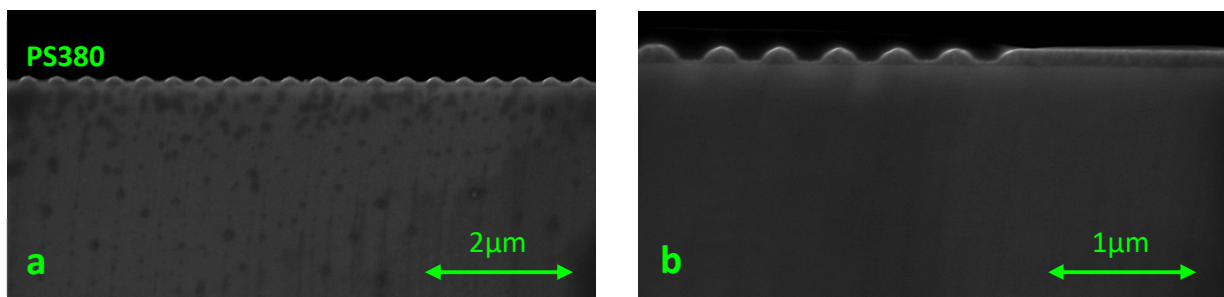


Fig. 38: Imprint of PS380, annealed at 70°C for 5min. Charging issues are apparent by the white glowing tips of the grating. The features are uniform, residual layer is thin, ~20nm. (a) shows the profile in lower, (b) in higher resolution. Glowing tips indicate a charging issue.

PS380 shows good replication, and a significantly reduced residual layer thickness, especially toward the imprint-free areas. Overall, the residual layer thickness averages around 20nm. Some charging is evident by the bright tips of the structures and a degraded resolution. The duty cycle is also close to 70%.

#### 5.4. Adhesion Improvement

As *imec* conducts in-house research on nanoimprint lithography, many processes are already established. Most of them cannot be applied to spin-processed semi-organic perovskites, and have to be modified and adjusted accordingly. The first issue encountered during applying standard NIL techniques is lacking adhesion of the NIL resin to the perovskite surface. Delamination occurs during demolding of the working stamp, with the NIL resin sticking to the working stamp more than the perovskite.

Adhesion is a parameter that is easy to describe qualitatively, but not quantitatively. Although methods for calculating values of surface energies for thin films are known in literature, this would have exceeded the scope of this thesis by far. Therefore, adhesion is qualified by visual inspection of the film. Differences in haptic feedback during delamination can also be felt, but not quantified.

The manufacturer's instructions call for curing of the NIL resin at 120°C for 1min. As the MAPbI<sub>3</sub> perovskite is cured at 70°C for 5min and it was noticed during earlier trials that heat above 100°C degrades the light emitting properties, it was decided that curing of the NIL resin should take place at no higher than 50°C. After observing severe delamination issues, annealing is moved to 70°C for 5min, and partial improvements are seen. The first trials are done to confirm if curing the resin at higher temperatures for the short time of 1min will degrade the performance of the perovskite noticeably. Therefore, samples are prepared with MAPbI<sub>3</sub> and UV-A resin, and a test split with different annealing times and temperatures is run as illustrated in Tab. 15.

Tab. 15: Annealing temperatures and times of curing trial

T [°C]	70	70	70	80	90	100	120
t [min]	5	10	15	5	5	5	2

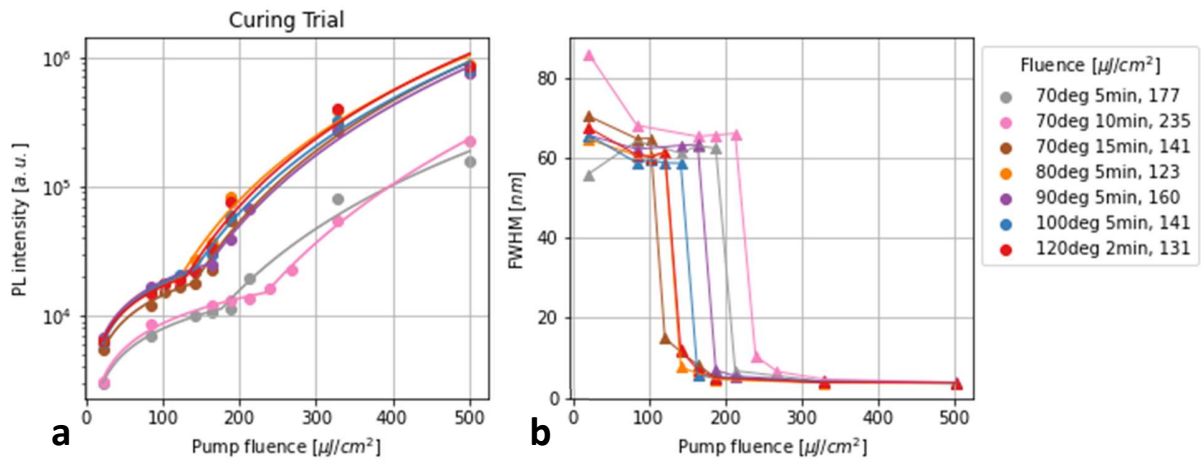


Fig. 39: Threshold (a) and FWHM curves (b) from curing trial. Two lines (70°C 5min and 70°C 10min deviate from the general trend. The FWHM curves are separated, but without showing any trend.

Spectra are collected with the 45° backscatter fiber (cf. chapter 4.10.3) so that no grating interaction is recorded. Fig. 39 shows the results of the fiber measurements. Most thresholds lie between 123 and 177 μJ/cm<sup>2</sup>, only one is higher at 235. It can be seen that two samples (70°C 5min and 70°C 10min) have lower total intensity, with 70°C 5min also having a significantly lower slope angle after threshold. The FWHM curves are spread out more, but no clear trend is visible.

Results show no significant increase in threshold, recorded via the fiber setup. Adhesion is notably getting better with higher curing temperature, but delamination will still occur in about 50% of cases (either on the whole surface or only on parts of the surface – in both cases, the working stamp is still unusable for further imprints).

Data from one sample is shown below in Fig. 40, which shows the emission spectra for different fluences in a logarithmic scale. It can be seen that a bump appears around the 164.2 μJ/cm<sup>2</sup> line in Fig. 40a, and a kink is visible around the same fluence in Fig. 40b. The FWHM of the peak does not decrease below 4nm as the intensity further increases, which is expected due to the setup only collecting diffusely scattered light from an unimprinted (= bulk) area.

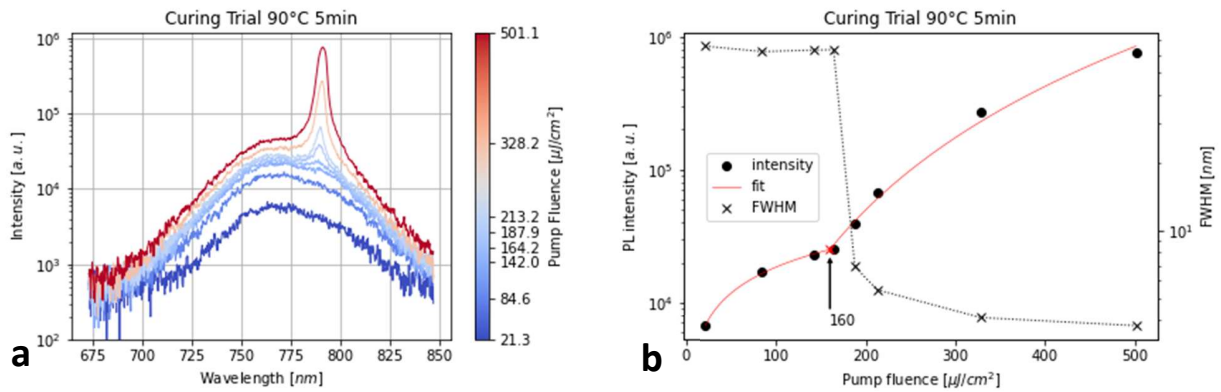


Fig. 40: Spectrum (a) and combined threshold/FWHM curve (b) for 90°C/5min curing. The peak is very broad, threshold and drop in FWHM coincide.

## 5.5. Sample List

An overview of the properties of samples discussed further in chapters 5.6-5.10 is given in Tab. 16. Samples investigated in XSEM or for curing trials are not included in the list.

Tab. 16: Samples and their process parameters

sample	active material	adh. prom.	resin	curing	imprint	remarks
1	120nm MAPbI <sub>3</sub>	70°C 5min	3000rpm	70°C 5min	PS380	UV-NIL deposition in cleanroom atmosphere
2	80nm MAPbI <sub>3</sub>	120°C 2min	3000rpm	120°C 1min	PS40	diluted UV-NIL resin to reduce thickness, residual layer
3	120nm MAPbI <sub>3</sub>	120°C 2min	6000rpm	120°C 1min	PS40	resin spin speed higher to reduce residual layer, UV-A4
4	120nm MAPbI <sub>3</sub>	70°C 5min	3000rpm	70°C 5min	PS90	half of surface covered with ITO before NIL
5	120nm FAPbI <sub>3</sub>	120°C 2min	3000rpm	120°C 1min	PS40	different active material, annealed at 90°C for ~30min

### 5.6. Sample 1: Spot vs. Line Excitation

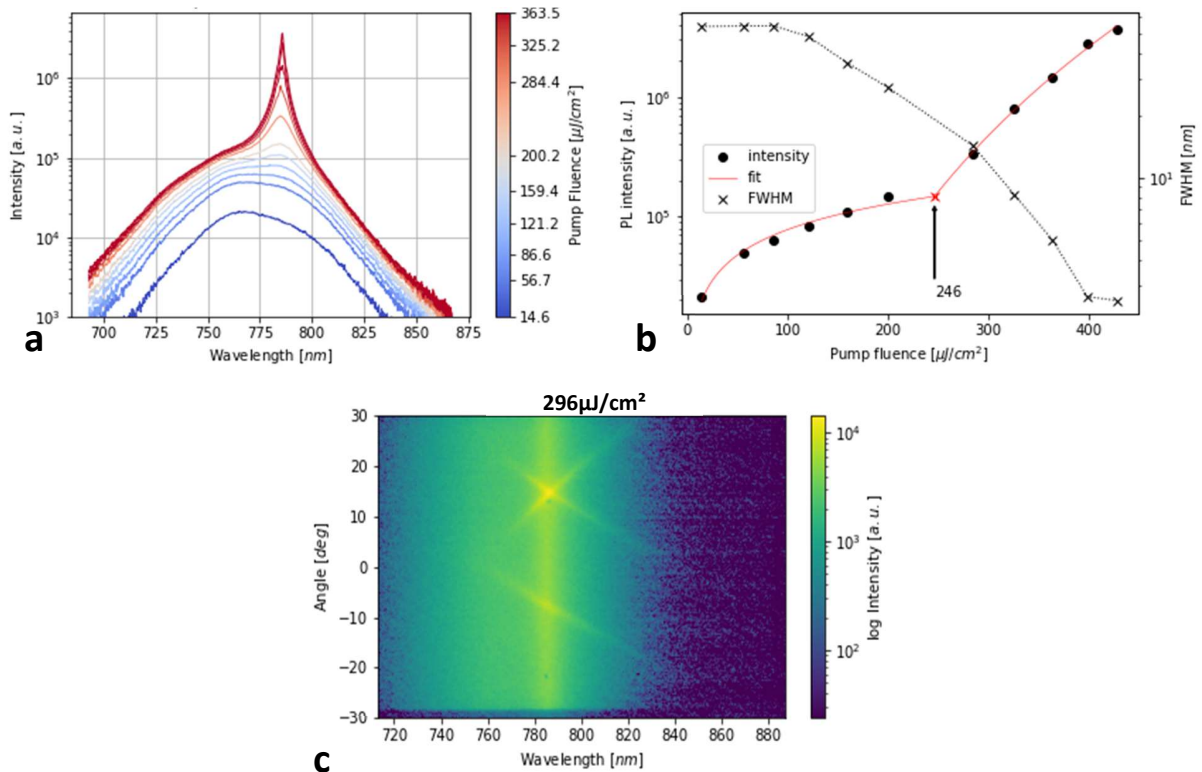


Fig. 41: Spectrum (a), threshold plot (b) and angular spectrum (c) of a 406nm grating on sample 1. The grating excited was of a B-type structure according to Fig. 7 ( $40\mu\text{m} \times 80\mu\text{m}$ ). The FWHM of the spectra does not drop below 2nm, and the slope after threshold is low. Angular spectra are shifted by  $\sim 15^\circ$  due to misalignment.

If a sample is investigated using the spot setup (cf. Fig. 10), a large bump in the spectra does become apparent above  $121\mu\text{J}/\text{cm}^2$ , which narrows constantly down to  $\sim 2\text{nm}$  FWHM at the highest fluence. At the highest fluences, a small sharp peak appears on top of the bump. The angular spectrum (here shifted by  $\sim 15^\circ$  due to a misaligned lens) shows a forward and backward propagating mode line. Below  $0^\circ$ , another line appears, which can be attributed to a higher-order mode within the resonator. The mode lines cross around 785nm, the area where a very wide vertical line can be seen. In the crossing point, the intensity appears somewhat amplified, but to a limited extent.

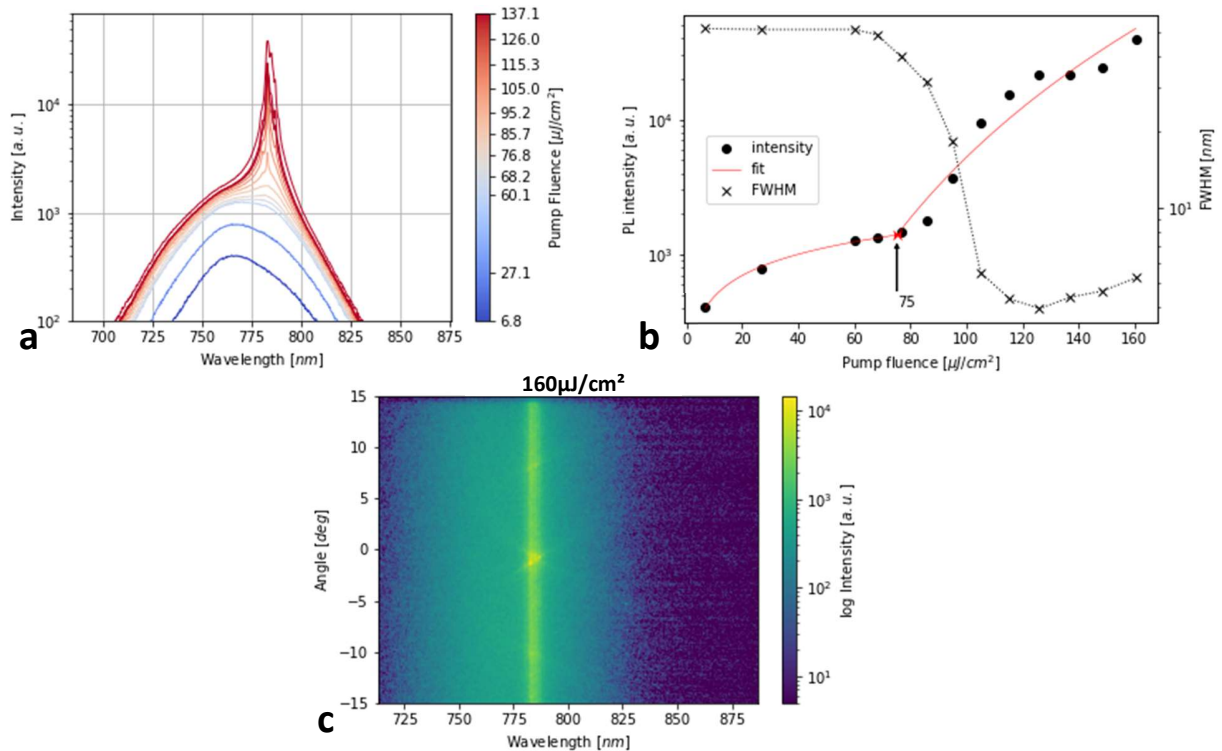


Fig. 42: 1D-spectrum (a), threshold plot (b), angular spectrum (c) of a 410nm grating ( $40 \times 80 \mu\text{m}$ , structure B) on sample 1. The threshold appears lower, spectra show finer lines in combination with some ASE-like features. The gain band in the angular plot is narrower, angular features appear only weakly.

The same sample (but at a slightly different grating period) investigated under a line excitation of variant A (two cylindrical lenses) shows a wholly different response. A wider peak appears above  $70 \mu\text{J}/\text{cm}^2$ , but soon narrows to a thin peak at  $95 \mu\text{J}/\text{cm}^2$ , before devolving into a spectrum containing multiple peaks close to each other. The peaks are not position-invariant, meaning if the excitation line is slightly translated over the sample, the peaks may change position significantly. The threshold of the sample appears at lower fluences, and the gain band as seen in Fig. 42c is narrower than under spot excitation.

### 5.7. Sample 2: Cryo-Cooling

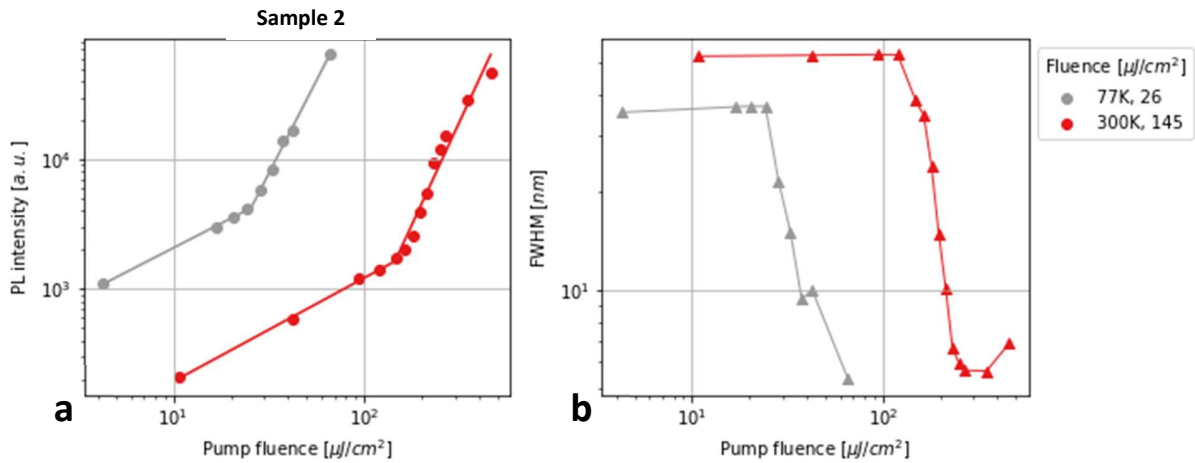


Fig. 43: Intensity (a) and FWHM (b) plots of a bulk area, at room and at liquid  $\text{N}_2$  temperature. Note the double logarithmic axes. At low temperatures, threshold is significantly decreased.

Sample 2 is investigated using the cryostat stage. Due to consequent geometric limitations, the use of the 50x objective is not possible. It is cooled down to 77K with liquid  $\text{N}_2$  and the cryostat is evacuated. During cooling, development of a condensate film can be seen on the surface of the sample, visualized in Fig. 44. Most gratings do not emit a strong signal, which is believed to be due to the condensate film filling up the grating. Since no good grating signals are obtainable, only threshold values for unimprinted areas can be compared, as shown in Fig. 43.

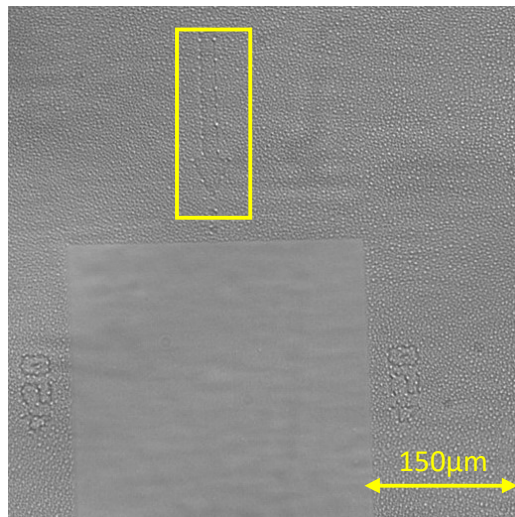


Fig. 44: CCD camera image of grating. Spots are visible on the arrow marked in the yellow box.



Spots can be seen in an image taken with the external camera, seen in Fig. 44. They appear in unimprinted areas, and are bigger at edges, like the arrow in the top of the picture. The grating seems to be unaffected by the spots.

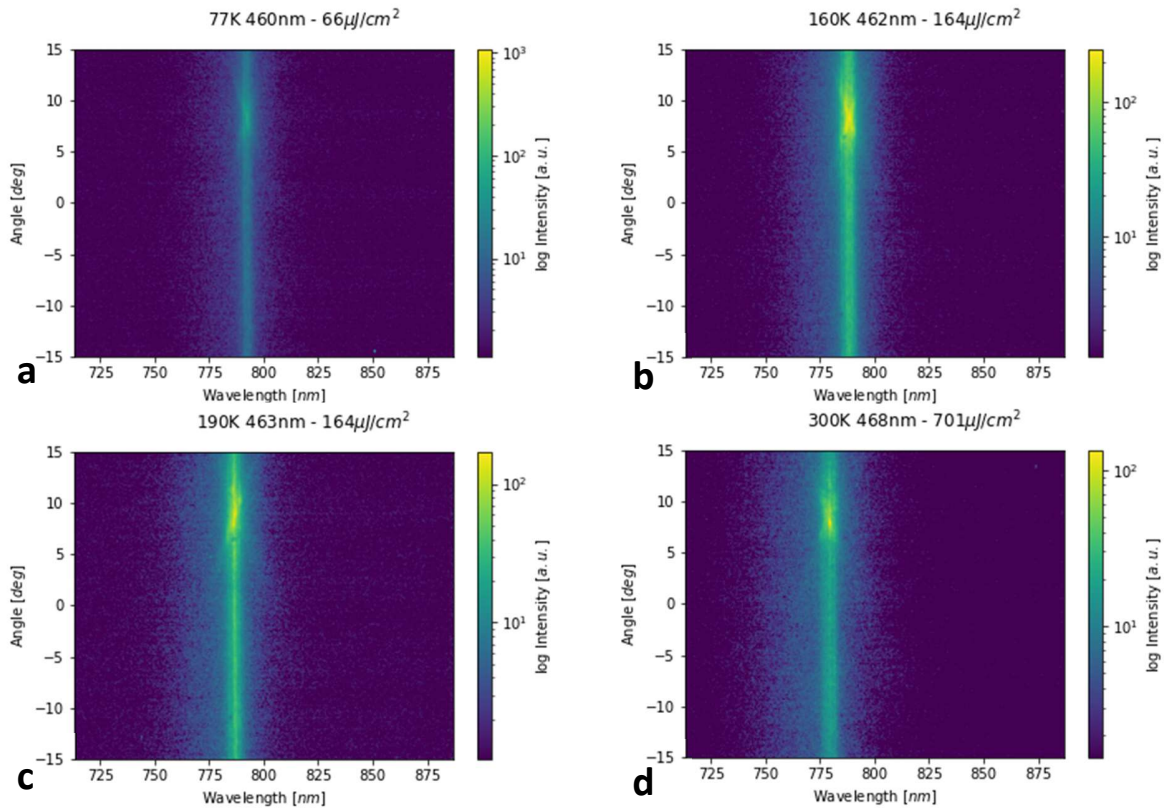


Fig. 45: Angular spectra of sample 2 at different temperatures. It can be seen that the gain band (vertical line) continuously shifts to lower wavelengths from 77K (a) to room temperature (d). The mode crossing can be seen faintly at  $\sim 10^\circ$ , indicating a BFP lens misalignment.

The sample is then brought to RT, which leads to the disappearance of the spots seen in Fig. 44. Photonic band structures can now be recorded when the large chirped grating is excited. The spectra seen in Fig. 45 are shifted by  $10^\circ$  due to a misaligned BFP lens. The photonic bands appear faint and under higher slopes, which is due to the 10x objective having a reduced collection angle. One notable observation is the shift of gain bandwidth of the sample during cooling. Angular spectra are collected with the line placed on the large chirped grating (structure A), and the mode crossing is aligned with the gain band by translating the excitation line across the grating (Fig. 45). The period of the grating is estimated from the measured position of the line on the chirped grating. A shift of the gain band (the vertical line) is observed when decreasing the temperature. As a result, the mode crossing aligns with the gain band at different grating periods, moving from 468nm at RT down to 460nm at 77K.

### 5.8. Sample 3: Grating Length Study

To investigate the influence of the size of the grating on the emission of the sample, different lengths of the grating (corresponding to different lengths for which the standing wave within the active layer would experience gain, hence the term “gain length” is used interchangeably) are investigated on sample 3. The grating period in all cases was 406nm. A master stamp with structure D is used for this purpose. The width of the gratings stays constant at 40 $\mu\text{m}$ , while the length varies from 20 $\mu\text{m}$  to 140 $\mu\text{m}$  in steps of 20 $\mu\text{m}$ . The length of the laser line is adjusted via a slit to illuminate only the grating area.

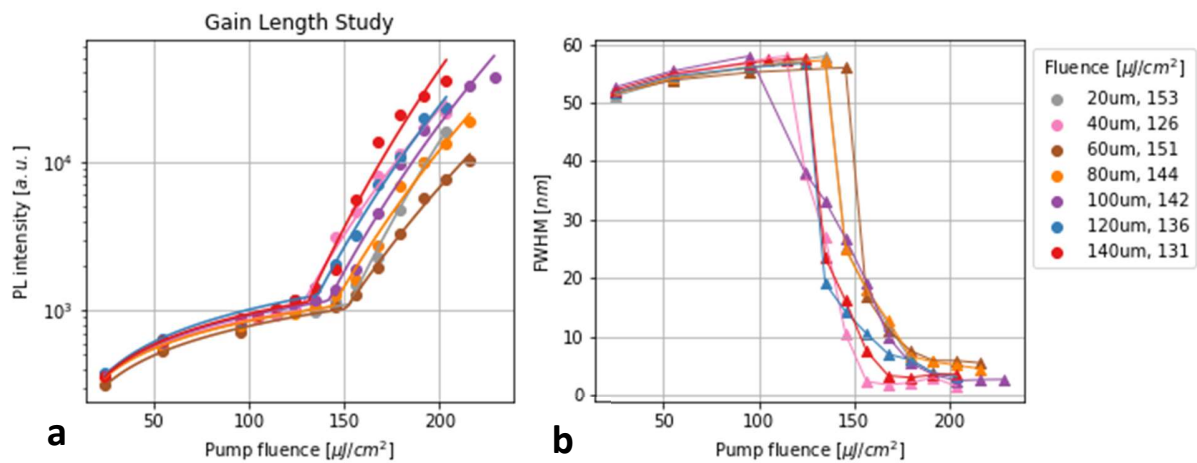


Fig. 46: Intensity (a) and FWHM (b) plots for the gain length comparison. Longer gratings shift the threshold to lower values. The threshold for the 40 $\mu\text{m}$  long grating does not fit the trend. The FWHM for the 100 $\mu\text{m}$  long grating drops earlier due to a more pronounced ASE signal.

As seen in Fig. 46, the threshold for the different lengths is in the range of 126-151 $\mu\text{J}/\text{cm}^2$ . The general trend is to lower threshold values for higher grating length. Only 40 $\mu\text{m}$  grating length defies this trend. The polarization of all of the gratings is quite similar, showing extinctions between 6 and 8. Only the 40 $\mu\text{m}$  length has higher extinction with 15.

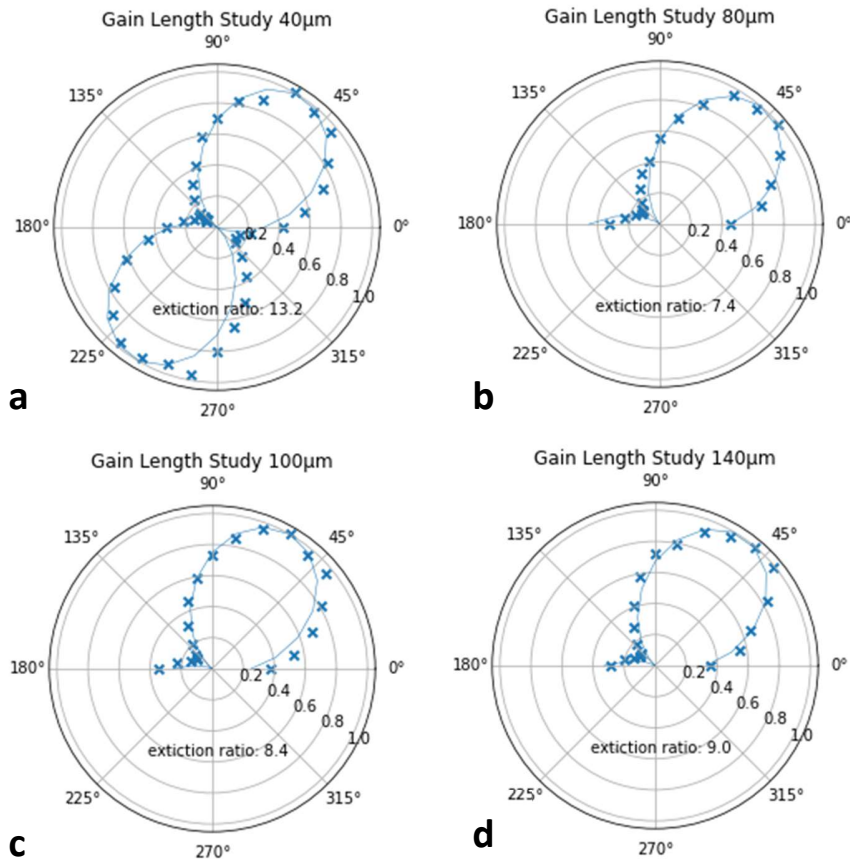


Fig. 47: Polarization plots for different gain lengths: 40 μm (a), 80 μm (b), 100 μm (c), 140 μm (d). (a) shows data recorded over the whole 360° range of the polarizer, and also has higher extinction, which might be due to a higher grating quality. Overall, the extinction is quite similar.

## 5.9. Sample 4: Main Findings

Sample 4 possesses 120nm of MAPbI<sub>3</sub> and half of the surface is covered with ITO. On top of the ITO, an adhesion promotor and UV-NIL resin are applied and baked at 70°C for 5min. The imprint is made using a working stamp made of PS90.

### 5.9.1. Preliminary Comparisons

Different lengths of the excitation spot were used during the measurements. Measurements were conducted on 140x40 μm gratings of type D (cf. Fig. 7) with a period of 406nm. As can be seen in Fig. 49, the length of the line does not change the threshold significantly. Also, the slopes of the lines after threshold are approximately the same.

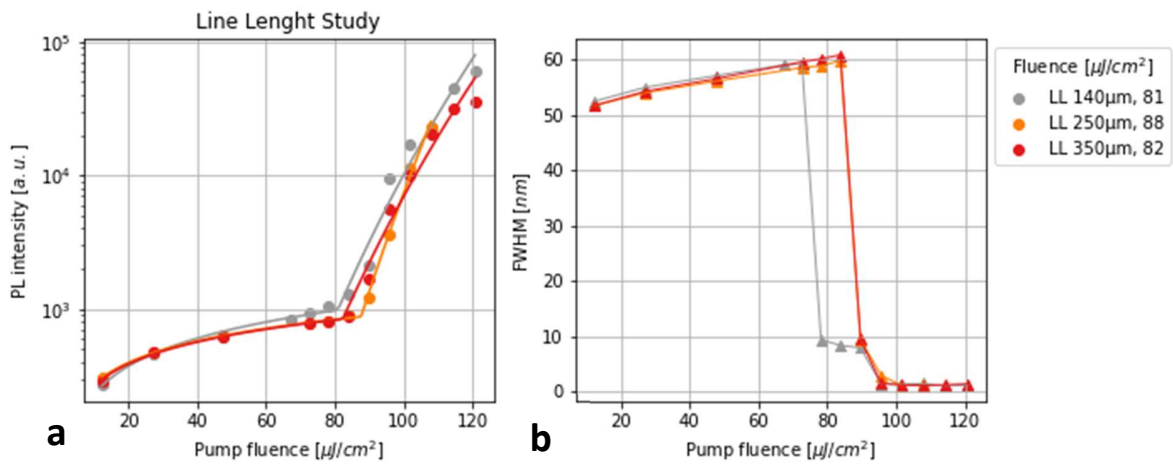


Fig. 49: Intensity (a) and FWHM (b) plots for 406nm gratings (140x40 $\mu\text{m}$ ) for lines of different length (140 $\mu\text{m}$ , 250 $\mu\text{m}$ , 350 $\mu\text{m}$ ). All line lengths show similar thresholds. The FWHM curve of the 140 $\mu\text{m}$  line drops earlier and reaches a plateau at 10nm before dropping further, indicating ASE.

The spectrum for a 140 $\mu\text{m}$  line looks different than that of a 350 $\mu\text{m}$  line (Fig. 48). The longer line appears to produce a spectrum containing multiple peaks, especially at higher fluences. The shorter line produces one singular thin line, up to the highest fluence.

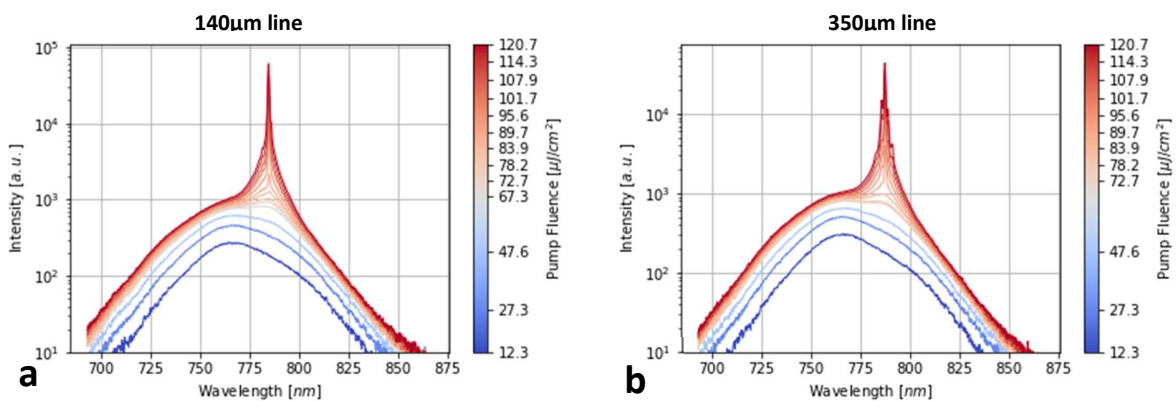


Fig. 48: Spectrum of 406nm grating, excited with a 140 $\mu\text{m}$  line (a) and a 350 $\mu\text{m}$  line in comparison. (a) shows a single fine line up to high fluences, whereas the initial fine line in (b) soon turns to a convolution of multiple peaks overlapping.

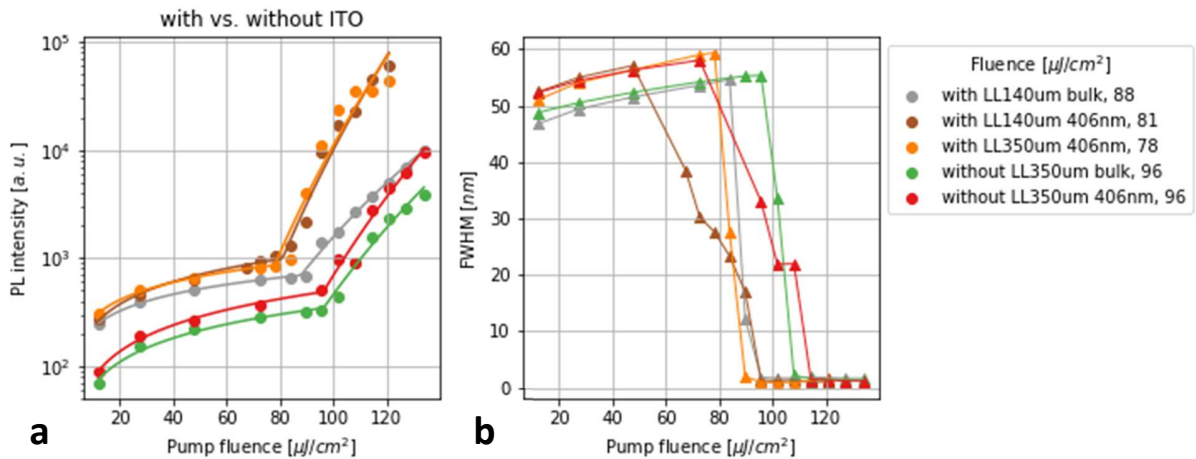


Fig. 50: Intensity (a) and FWHM (b) plots for bulk and 406nm gratings, with and without ITO interlayer. Thresholds for layers without ITO are marginally higher, which may be due to thickness variations within the sample.

If similar gratings with or without an ITO interlayer are compared, it can be seen that thresholds for the ITO gratings are lower by about 10% than the ones without ITO. Also, the slope after threshold is steeper for the 406nm gratings over ITO than for no ITO or bulk measurements. The FWHM drops to around 1nm, which corresponds to the resolution limit of the spectrometer in the chosen grating configuration.

### 5.9.2. Bulk

An area with a planar layer of UV-NIL resin without any imprinted grating structure (=bulk) is investigated. Between  $83.9\mu\text{J}/\text{cm}^2$  and  $89.7\mu\text{J}/\text{cm}^2$  in Fig. 51a, two bumps appear in the spectrum. The bumps grow into two distinguishable peaks, with narrow line widths below 1nm. A vertical line corresponding to the gain bandwidth can be observed in Fig. 51d. No features indicating any grating influence are visible in Fig. 51e and f.

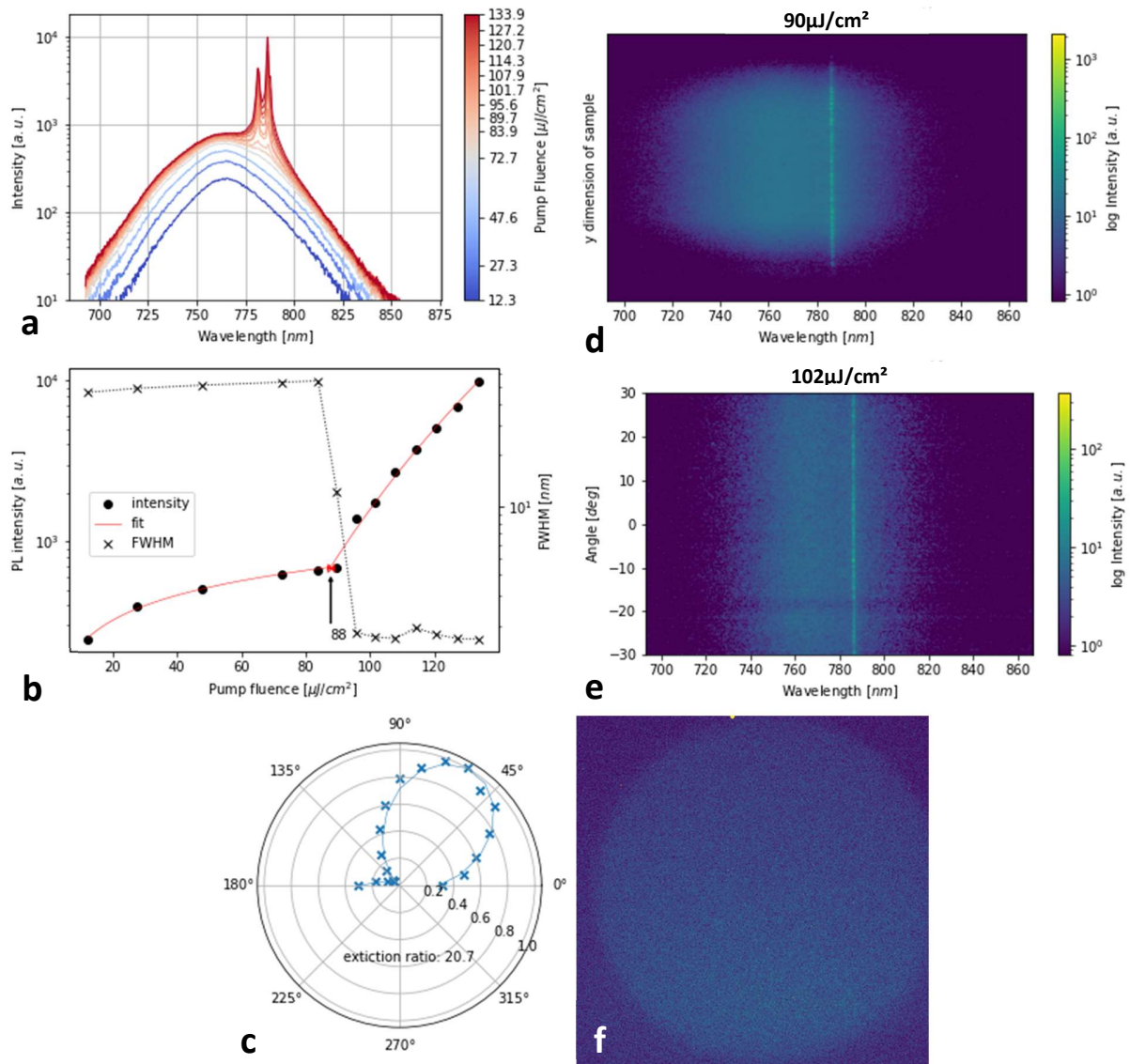


Fig. 51: Spectrum (a), threshold (b) and polarization (c), 2D spectrum (d), angular spectrum (e), and far-field image (f) of bulk area. Multiple peaks appear in (a), the singular fine line in (d) and (e) is due to the lower fluence. Extinction is high with 21 (c), and (f) shows no far-field pattern.

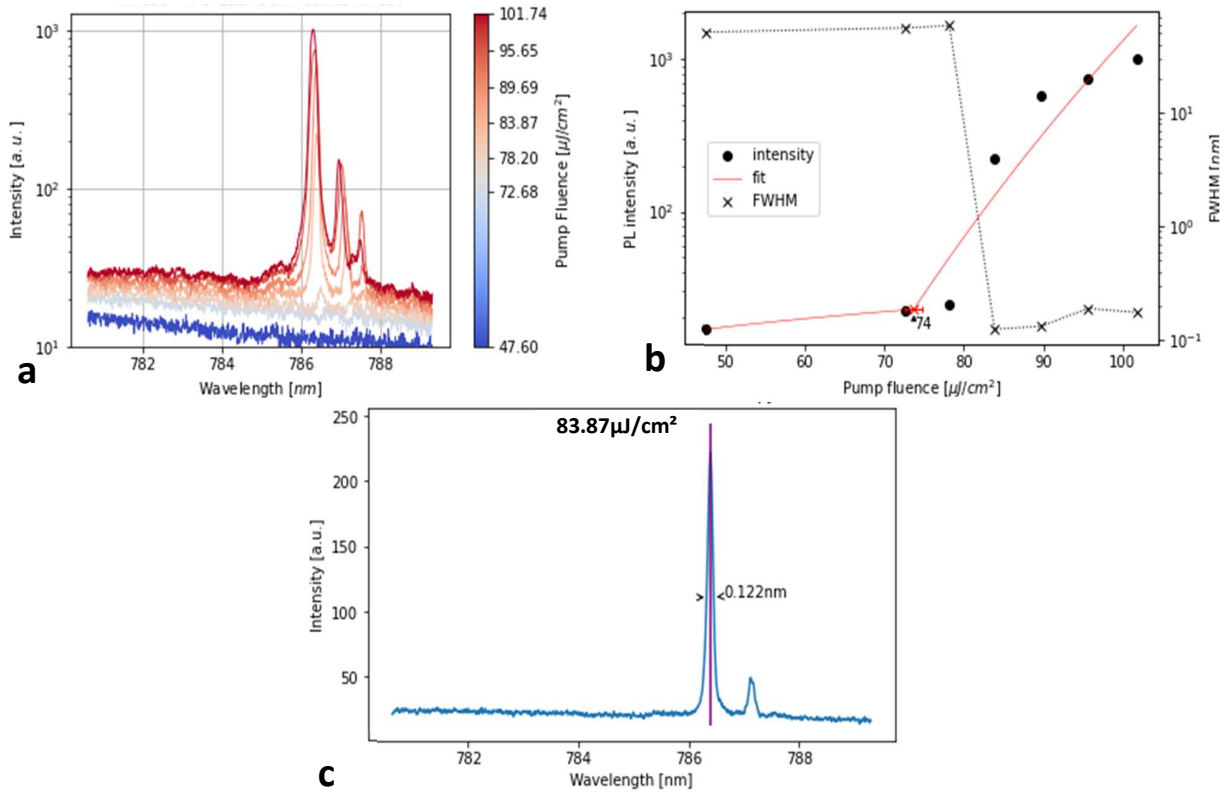


Fig. 52: Highest resolution of spectrum (a), corresponding threshold plot (b), line width (c). Three peaks appear in (a), threshold is seen at  $74 \mu\text{J}/\text{cm}^2$  in (b), linewidth in (c) is  $0.122 \text{ nm}$ .

In the highest resolution of the spectrometer, three emission lines can be seen in the spectrum (Fig. 52a), and the threshold appears a bit lower around  $74 \mu\text{J}/\text{cm}^2$  (Fig. 52b). The lines are very fine, with a line width as low as  $0.12 \text{ nm}$  (Fig. 52c).

### 5.9.3. Grating 406nm over ITO

A 406nm grating of 140 $\mu\text{m}$  length and 40 $\mu\text{m}$  width is excited with a beam of 140 $\mu\text{m}$  length and around 40 $\mu\text{m}$  FWHM of the Gaussian beam profile. The resulting spectrum exhibits a narrow peak appearing around 80 $\mu\text{J}/\text{cm}^2$ . In the threshold fit, the FWHM decreases to a plateau value of around 10nm before dropping further to around 1nm, which is the resolution limit of the spectrograph in this setting.

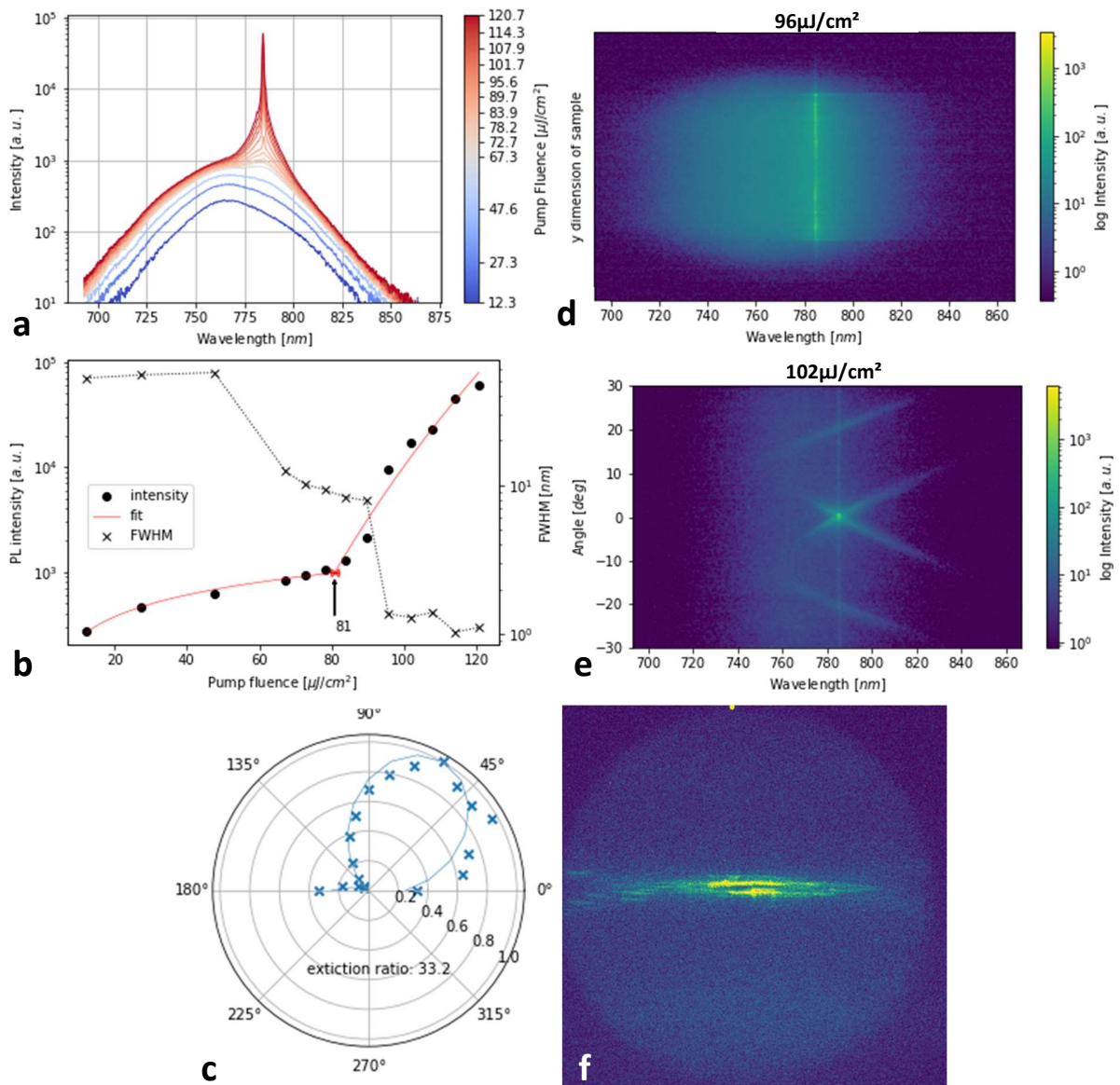


Fig. 53: Spectra of a 406nm grating. (a) 1D spectrum, (b) threshold plot, (c) polarization plot, (d) 2D spectrum, (e) angular spectrum, (f) far-field image. In (a), a very fine line emerges from an initially wider (ASE) peak. The same line can be seen in (d), where the grating extent is also visible by horizontal lines. The threshold in (b) is  $\sim 81 \mu\text{J}/\text{cm}^2$ , FWHM shows a plateau which is also indicative of ASE. Polarization (c) is high, the angular image shows photonic bands that intersect the narrow gain band with strong amplification. The far-field image shows intersecting bent lines.



The polarization exhibits strong extinction of said peak with a ratio of 33. In the 2D spectrum, a very narrow line is visible. Also, the extent of the grating can be seen, as the grating emits stronger than the surrounding bulk material. This leads to two horizontal lines in the spectral graph, corresponding to the upper and lower edge of the grating. The sharp line also appears to extend outside of the grating boundary.

In the angular distribution image (Fig. 53e), two sets of parallel slanted lines are visible. The two lines that can be seen intersecting around 780nm correspond to the forward and backward propagating transverse electric (TE) modes respectively, while the outer lines correspond to the transverse magnetic (TM) modes. At their intersection point, the vertical emission line also passes through, and a bright spot can be seen in the crossover. The far-field emission pattern shows two curved lines intersecting each other.

When analyzed with a finer spectrometer grating (300g/mm), it can be seen in Fig. 54a that the line appearing is even finer than the 1nm measured with the standard grating. The threshold appears at roughly the same value of around  $80\mu\text{J}/\text{cm}^2$  in the intensity plot, the fit in Fig. 54b indicates  $71\mu\text{J}/\text{cm}^2$ . At higher fluences, satellite peaks appear in regular intervals from the main peak. Their size appears exaggerated due to the logarithmic scale.

The polarization is strong, with an extinction factor of 53. Some anomalies can be seen in the plot at higher intensities, where the measured points deviate from the predicted  $\cos^2$  contour.

When taking a look at the 2D spectra, it can be seen that the grating itself emits strongly, while the bulk emits much less. A fine line at 784nm can be seen at lower fluence, while at higher fluence more lines in equally spaced intervals appear left and right of the peak. This also holds true for the angular emission image of the grating. The finer spectrometer grating allows for multiple lines to be distinguished in the region of the TE mode crossing. The lines' intervals appear similar to the ones in the 2D spectra, and the peak distances in the 1D spectra.

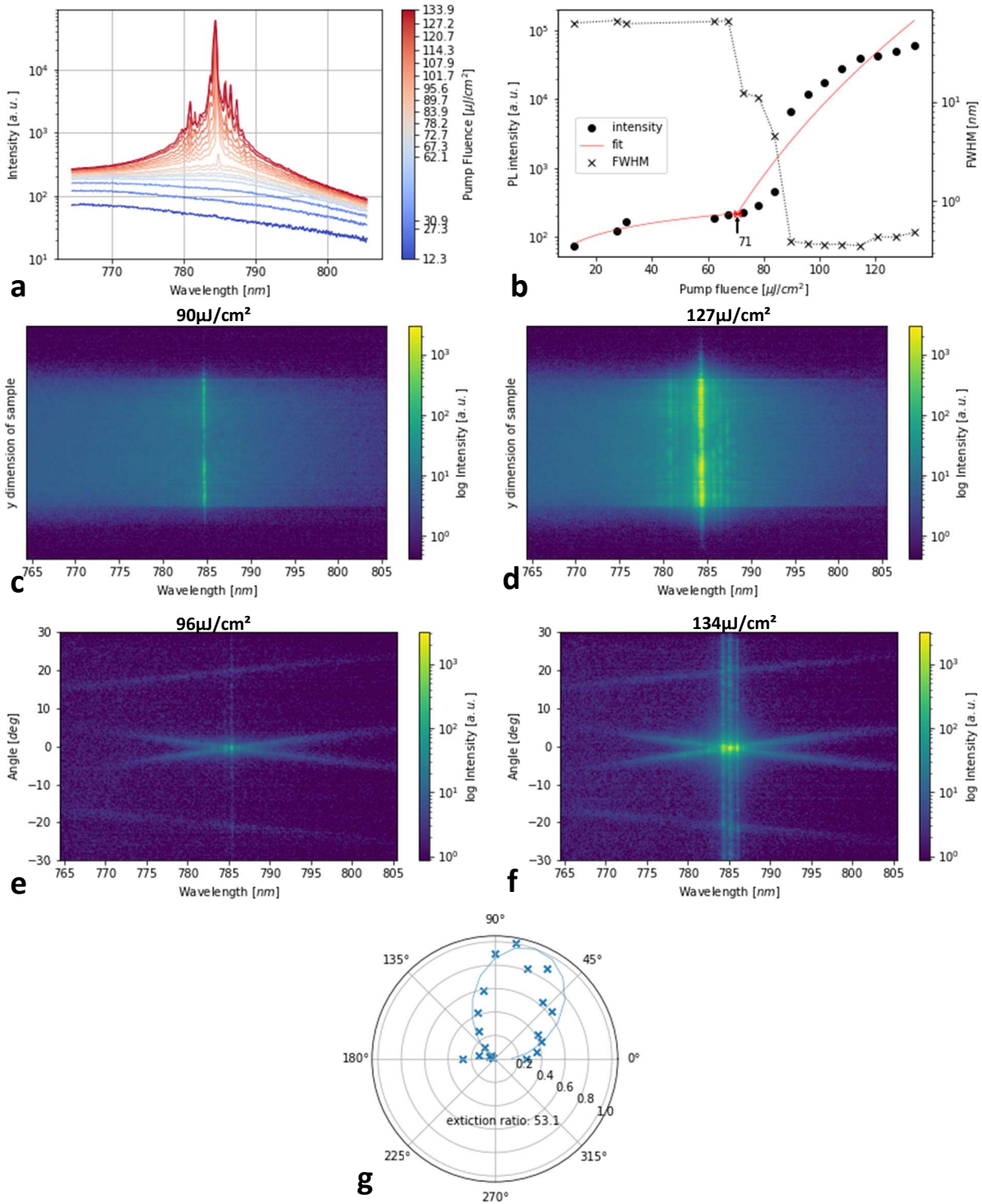


Fig. 54: Middle resolution of 1D spectra (a), corresponding threshold plot (b), 2D spectra (c), (d) and angular spectra (e), (f), polarization plot (g). Satellite peaks appear around the main peak as seen in (a), and mirrored by the vertical lines in (d) and (f). Strong amplification from the grating is observed in (c) and (d). Polarization is very strong, with a ratio of  $\sim 53$ . The threshold is  $\sim 78 \mu\text{J}/\text{cm}^2$  according to (b).

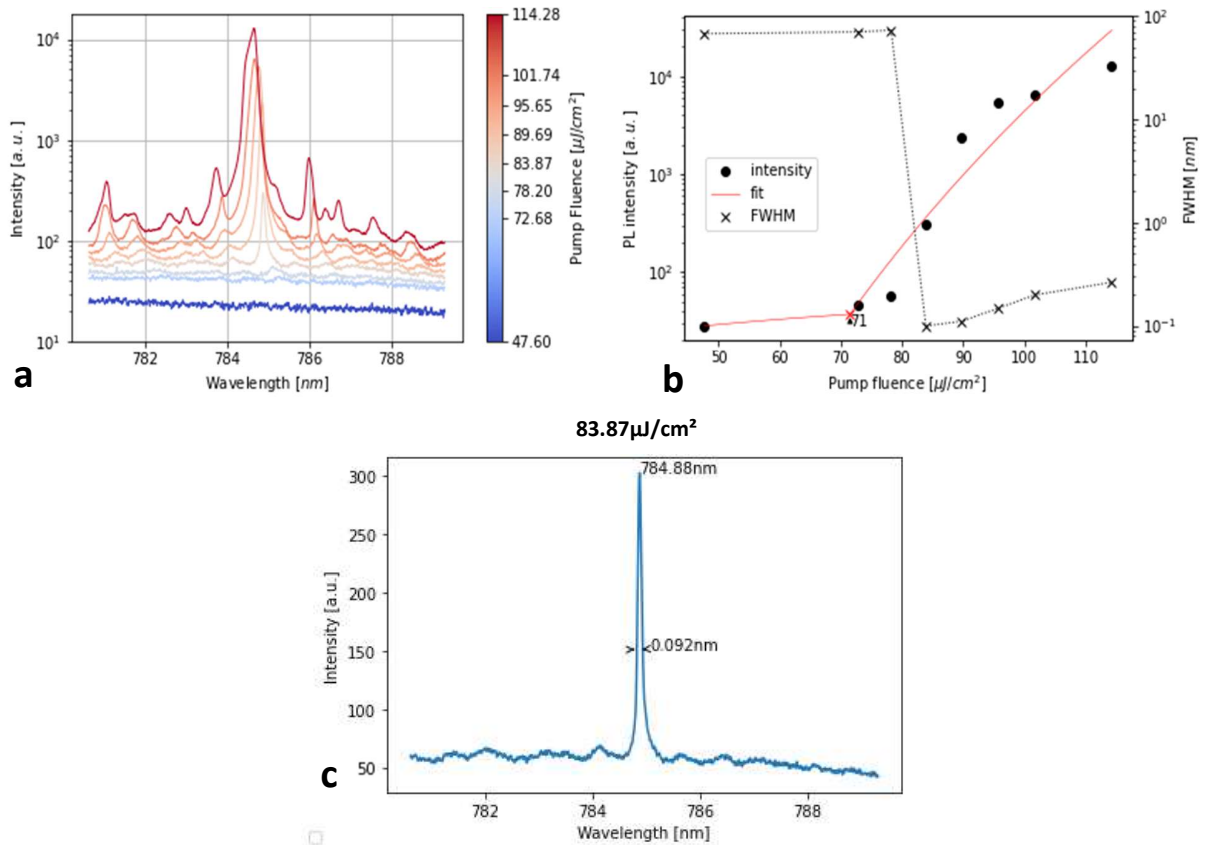


Fig. 55: Highest resolution of spectra (a), corresponding threshold plot (b) and line width (c). Satellite peaks in (a) are exaggerated due to the logarithmic scale, but appear in regular distances to the main peak. (b) shows a threshold around  $70\mu\text{J}/\text{cm}^2$ , and sharp drop in FWHM. The peak width is evaluated in (c), yielding  $0.092\text{nm}$  FWHM.

The finest available spectrometer grating ( $1200\text{g}/\text{mm}$ ) can resolve the peak width properly. The threshold appears to lie above  $80\mu\text{J}/\text{cm}^2$  as indicated in the intensity plot, and is again approximated as  $71\mu\text{J}/\text{cm}^2$  in the fit. Fig. 55c shows the peak width calculated from one single spectrum of Fig. 55a. The peak width is measured to be  $0.092\text{nm}$ . The Q-factor is estimated from the linewidth (cf. Eq. 2) as  $Q = \frac{784.88\text{nm}}{0.092\text{nm}} = 8531$ .

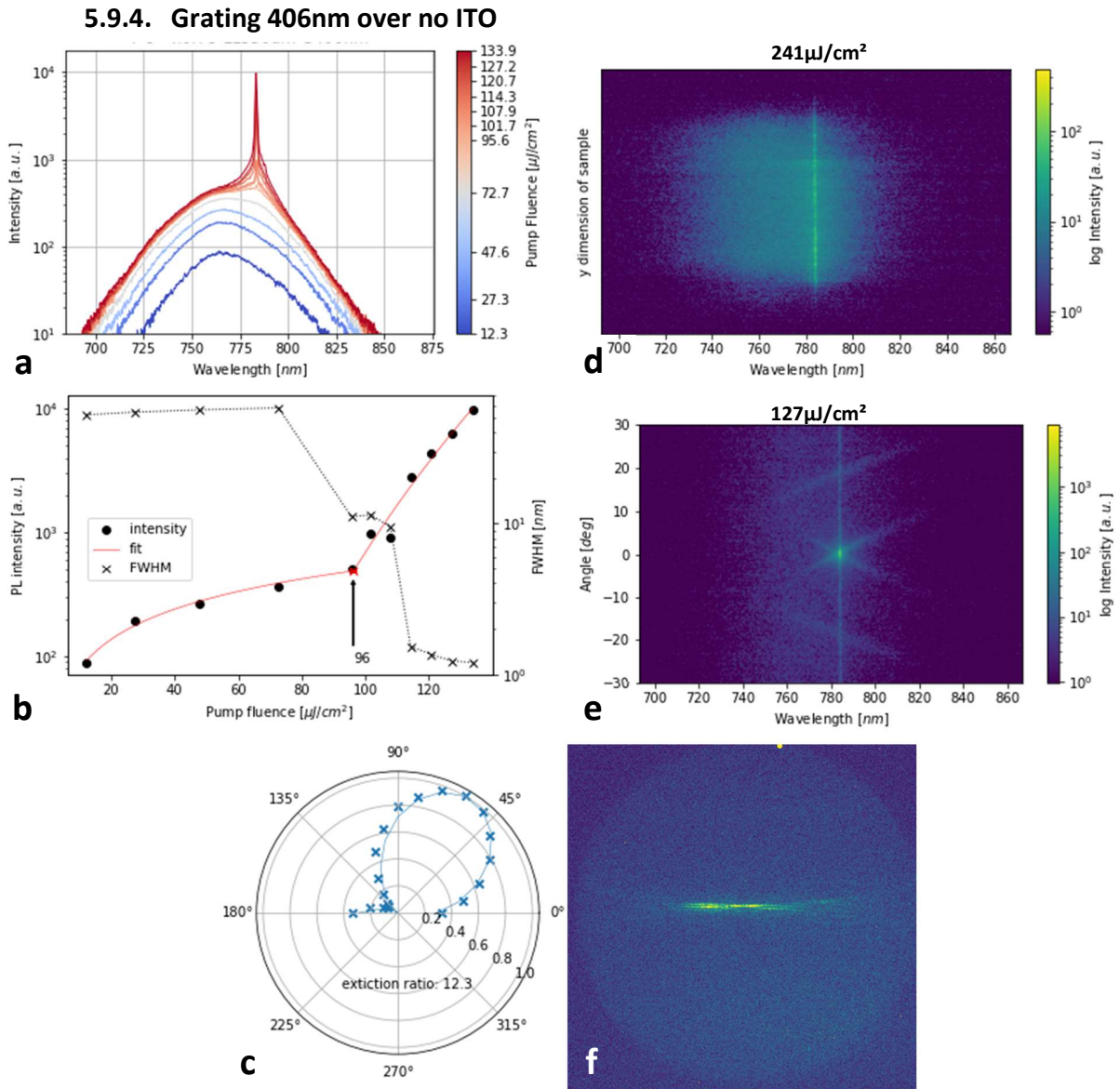


Fig. 56: 1D spectrum (a), threshold plot (b), polar plot (c), 2D spectrum (d), angular spectrum (e), far-field image of a 406nm grating without ITO interlayer. The peak in (a) is as fine as in Fig. 53. Threshold is higher (b), polarization is weaker (c) is weaker. Photonic bands in (e) and lines in (f) are less pronounced.

When the equivalent 406nm grating is investigated where no ITO is present, the following is observed: A fine line is emitted around the same wavelength as seen in Fig. 56a. The threshold is slightly higher ( $\sim 95 \mu\text{J}/\text{cm}^2$ ). Extinction is  $\sim 12$ . In the 2D spectrum, the line can be seen extending further into the bulk area beyond the grating, which in this case is  $120 \mu\text{m}$  long. The angular image appears quite similar to the case with ITO, but the intensity of forward and backward propagating TE modes is less pronounced. The far-field pattern appears similar to the ITO-covered case, but is less intense at higher excitation ( $127 \mu\text{J}/\text{cm}^2$  vs.  $108 \mu\text{J}/\text{cm}^2$ ).

## 5.9.5. Grating 426nm over ITO

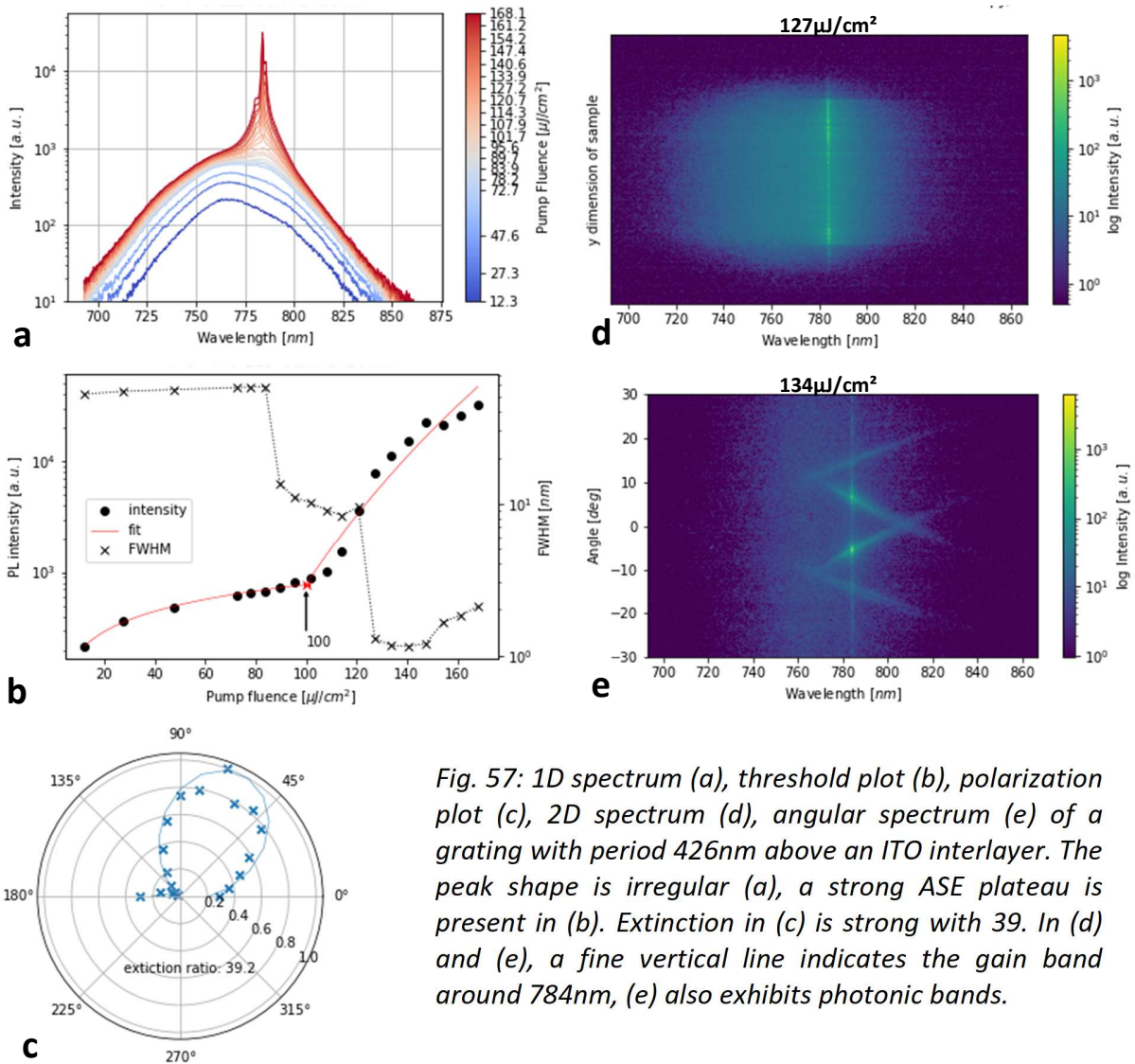


Fig. 57: 1D spectrum (a), threshold plot (b), polarization plot (c), 2D spectrum (d), angular spectrum (e) of a grating with period 426nm above an ITO interlayer. The peak shape is irregular (a), a strong ASE plateau is present in (b). Extinction in (c) is strong with 39. In (d) and (e), a fine vertical line indicates the gain band around 784nm, (e) also exhibits photonic bands.

If a grating of period 426nm above ITO is investigated, the peak shape appears less sharp. Upon closer inspection, it looks like it is composed of multiple peaks. The threshold is  $\sim 100 \mu\text{J}/\text{cm}^2$  in both the intensity plot and the fit. The extinction of the peaks still is quite strong with  $\sim 40$ . The threshold plot shows an FWHM of  $\sim 10 \text{nm}$  between  $90 \mu\text{J}/\text{cm}^2$  and  $120 \mu\text{J}/\text{cm}^2$ . The 2D spectrum presents a single thin line with little leakage into the bulk. The angular spectrum reveals that the gain bandwidth lies about 20nm from the TE mode crossing, which can be found at  $\sim 810 \text{nm}$  for that grating. Where the vertical line intercepts the propagating mode lobes, it appears enhanced.

### 5.10. Sample 5: FAPbI<sub>3</sub>

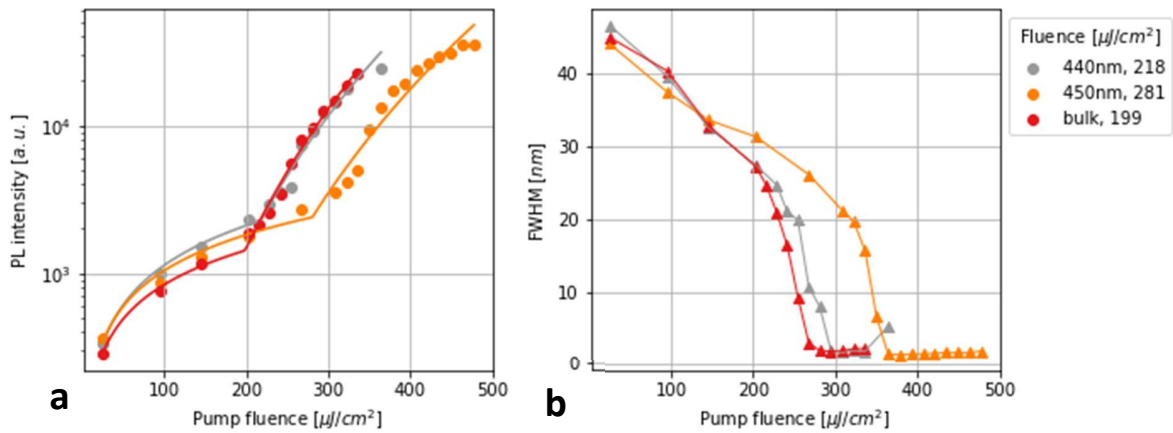


Fig. 58: Intensity (a) and FWHM (b) plots for a sample with FAPbI<sub>3</sub> active layer. Threshold is lowest for the bulk region. FWHM does not sharply drop, but exhibits an almost linear decrease.

Investigating a sample with a different active layer, FAPbI<sub>3</sub>, it can be seen in Fig. 58 that thresholds are significantly higher than for MAPbI<sub>3</sub>. The FWHM does not decrease as sharply as for MAPbI<sub>3</sub> either, rather a continuous decrease until a bottom plateau is reached. The minimal FWHM is also higher (2nm) and does not approach the resolution limit of the spectrometer. Higher-resolution spectroscopy shows the same picture. The threshold values vary greatly, and FWHM does not drop far below 5nm. In the spectral plots, no sharp peak appears up to a fluence of over 500μJ/cm<sup>2</sup>. The very wide peaks appear around 814nm. Polarization is very weak, with extinction reaching only ~3.4.

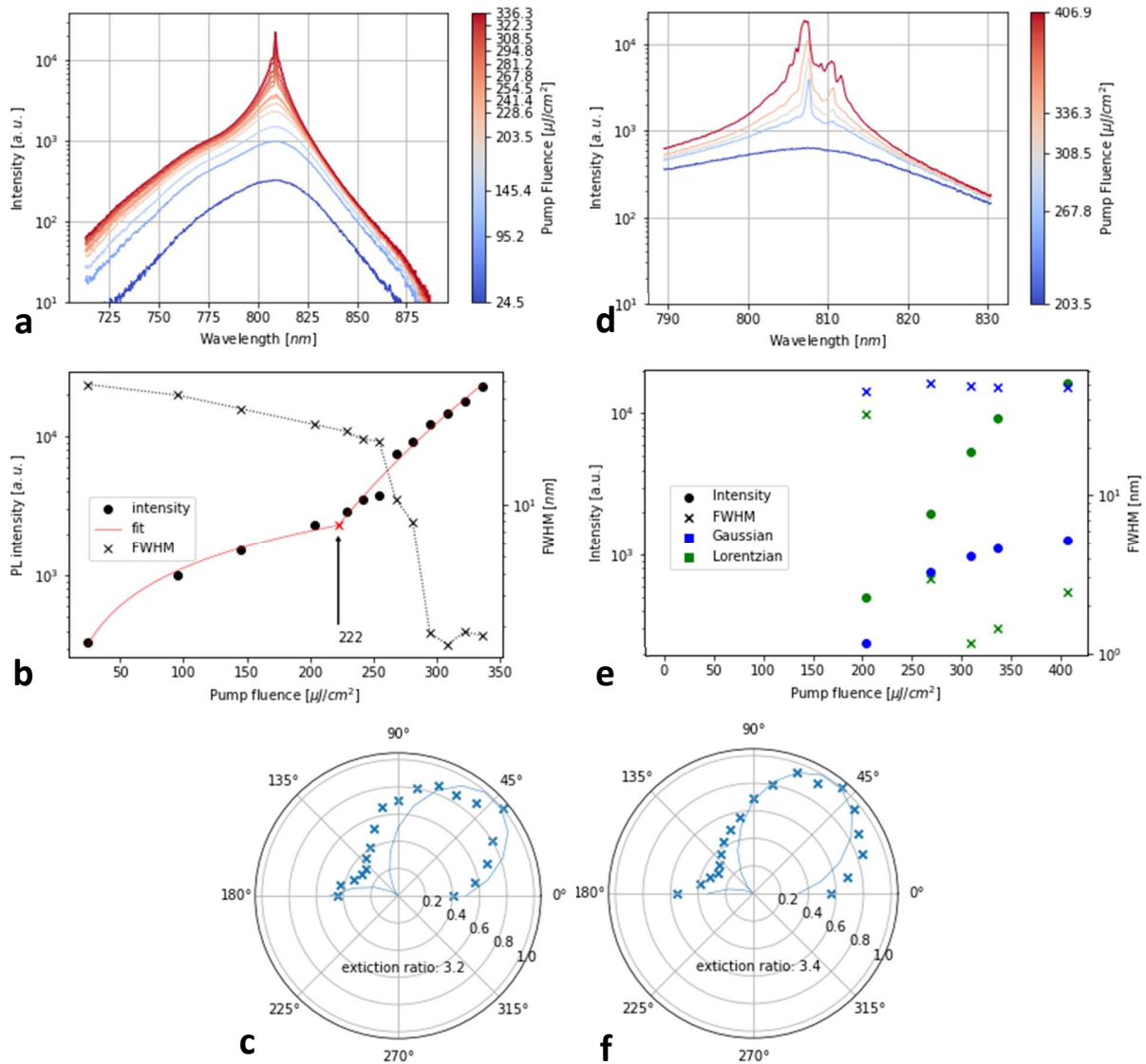


Fig. 59: left column – low resolution 1D spectrum (a), threshold plot (b) and polarization plot (c); right column – medium resolution 1D spectrum (a), line fits (b) and polarization plot (c). The line fit plot is shown instead of the threshold plot, as too few points are available for fitting the two-segment linear fit. (a) shows a wide peak up until  $\sim 250 \mu\text{J}/\text{cm}^2$ . A fine peak emerges at  $\sim 250 \mu\text{J}/\text{cm}^2$  in (a) and (d), with a line width of  $\sim 1 \text{ nm}$  as seen in (e). An irregular peak shape can be observed in (a). Polarization in both resolutions is similar (c, f).

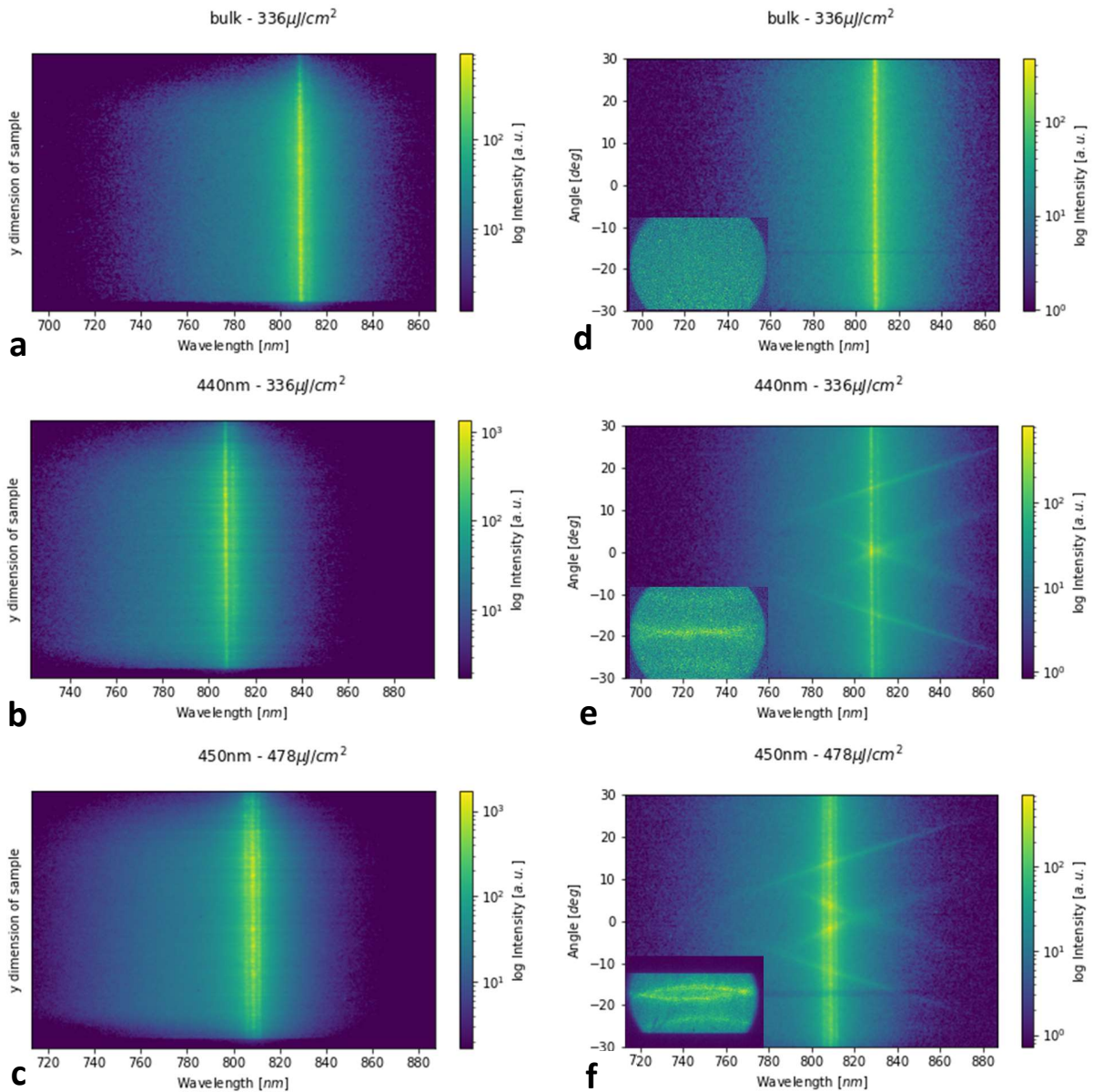


Fig. 60: 2D spectra (a, b, c) and angular spectra (d, e, f) of different grating periods on FAPbI<sub>3</sub>. Insets in (d, e, f) show the corresponding far-field patterns. The x-scales are not the same for all pictures. In (a, b, c), a central bright vertical line surrounded by a wider, less bright line appears around 810nm. The same line also appears in (d, e, f), in (e, f) it intersects photonic bands. The far-field images show no pattern for bulk, touching lines for 440nm and intersecting lines for 450nm.

Angular images of the emission (Fig. 60e, f) present weak forward and backward propagating modes. At higher grating periods, the TE mode becomes even fainter. Insets in Fig. 60 show the corresponding far-field emission patterns.



## 6. Discussion

### 6.1. Simulation

Simulations helped to predict and understand the grating behavior in the lab. The plots in Fig. 24 demonstrate that especially the duty cycle has a high influence on the grating response. Most other parameters tend to shift the peak position. The residual layer thickness study shows that grating response only significantly degrades above 100nm, indicating that negative influence from interlayers might be limited if the thickness is kept low. This assumes that those layers would have similar optical properties to the residual layer in these studies. The DOE-like parameter and response study in Tab. 12 indicates improved mode overlap for samples with reduced residual layers, which limits the usefulness of the previous conclusion. Also, a reduction in active layer thickness may improve mode overlap.

### 6.2. Ellipsometry

Ellipsometry measurements confirmed layer thicknesses, provided  $n$  and  $k$  values for different calculations, and produced spin curves that were used for processing.

### 6.3. Cross-Sectional Scanning Electron Microscopy

#### 6.3.1. Master stamp

We could discern that the etch process being used was not ideal, as the grating appeared to be non-rectangular, and uniformity of the grating peaks was limited. Issues in the master stamp will propagate to any working stamps, maybe even worsening in the process. The non-rectangular shape in itself should not pose a problem, which is underlined by findings in simulations. As the grating acts on the light through its periodicity, the interaction will still occur regardless of the peak shape. However, if the peaks in themselves are irregular, this might impact the interaction negatively, as the effective refractive index may vary slightly from peak to peak, selecting different resonance wavelengths at different positions. The reduced trench depth of only 80nm also impacts the grating response and mode overlap (cf. 5.1).

### 6.3.2. Etch Improvement

The different etch settings resulted in distinguishably different etch profiles. Notably, variation 4 shows the most uniform profile. The other recipes appear to just worsen the status quo, as it can be seen in Fig. 31-Fig. 33. Variation 1 also might have suffered from over-etching, although it is almost impossible to tell how much PMMA remained – thicknesses below 5nm are hard to resolve with either profilometer or ellipsometer. Variations 1 through 3 showed strongly isotropic etching. The valleys are rounded and peaks are either trapezoidal (Var. 1) or triangular (Var. 2 and 3). Variation 4 shows the highest uniformity. The sidewalls are strongly vertical, the top sections are very sharply defined. The bottom of the trenches is rounded but in a uniform and spherical way. Different peak shapes in the standard etch used to fabricate our master stamps might contribute to local aperiodicity and degrade grating quality. By moving to an etch according to variation 4, influence of stamp non-uniformity could be reasonably excluded from the studies conducted. The duty cycle is around 75%. Previously the e-beam linewidth was reduced to limit line widening. The high duty cycle indicates that line widening is not an issue in the case of variation 4. In our studies, we aimed for 50% duty cycle, because it is easy to control and does not lead to possible stability issues during the pattern transfer. Therefore, the duty cycle observed here was not deemed ideal for our use. Recent findings indicate though that duty cycle values close to 25% or 75% respectively would lead to higher diffraction efficiency.<sup>52</sup> To change the duty cycle, e-beam linewidth would have to be adapted, which may result in a time-consuming iterative process. As resources for e-beam writing were scarce within the scope of this thesis, the recipe change was not pursued any further, although it appears very promising.

### 6.3.3. Working Stamp Analysis

The features appear a bit more triangular than the ones seen from the Si master. The residual layers vary between 20nm to 40nm, most likely variations stem from processing differences. Higher annealing temperatures appear to improve replication. If cured at higher temperatures, PS40 seems to show less feature rounding. PS90 and PS380 both generally yield somewhat better feature replication. Overall, the structures can only be as good as the master stamps, highlighting the need for a uniform etching process.

#### 6.4. Adhesion improvement

Delamination in the first few batches of samples can mostly be attributed to improper curing of the used adhesion promotor and UV-NIL resin. The curing of the NIL resin and adhesion promotor at higher temperatures did not degrade the threshold of the active material. The adhesion was improved, and combined with the adapted delamination technique, intact samples could be produced repeatably. This result indicates that curing temperature is a crucial parameter in sample preparation. The difference in working stamp material in terms of feature reproduction is countered with a strong influence on demolding success. PS380 gives the best pattern replication, followed by PS90, and PS40 shows the worst results. However, the adhesion of the UV-NIL resin to the working stamp was highest for PS380, so much so that only very few samples could be produced with this working stamp material. PS40 worked reliably with the adhesion properties we could achieve, while PS90 was pushing the film to its limits, suffering high rates of delamination.

From time to time, delamination would still occur randomly even with PS40 as a working stamp, meaning that the adhesion between UV-NIL and underlying layers is only barely enough and sample yield would profit from increasing it. Also, demolding the working stamp from the sample too fast can result in delamination, emphasizing the need for careful process control and further adhesion improvement even more. Trials with mr-NIL (*micro resist technology GmbH*) were conducted, but upon contact with  $\text{MAPbI}_3$ , the latter was dissolved. Even the use of a special formulation of mr-NIL using PGMEA as a solvent resulted in dissolution of the perovskite. Further roads to explore from here would be the use of different UV-NIL resins. Another formulation with greater adhesion properties may be able to circumvent the processing issues encountered here.

## 6.5. Sample 1: Spot Excitation

Sample 1 was imprinted using working stamp material PS380, and the UV-NIL resin and adhesion promotor were deposited in the cleanroom under ambient air, not in the glovebox as usual.

If a 406nm grating of type B (cf. Fig. 7B) on the sample is excited using a circular spot ( $\varnothing \sim 250\mu\text{m}$ ), a strong influence of ASE is seen, as evident by the broad peak in Fig. 41a. Only at higher fluences, the tip of the peak narrows, but the increase of intensity is limited. Also, the prominence of the fine peak in relation to the wide ASE peak is small. The threshold is reached close to  $250\mu\text{J}/\text{cm}^2$ . The angular spectra in Fig. 41c also show some, but limited interaction of the gain bandwidth with the modes within the resonator. A certain amplification is evident by the brighter appearance of mode lines within the gain bandwidth, but it appears only at high fluences and to a limited extent.

Another investigation of sample 1 was carried out using a line excitation shape (variant A, cf. Fig. 10). A 402nm grating of type B presents different characteristics: The line shape appears finer and more irregular, as if the spectrum consists of multiple fine emission lines that combine into one irregular peak (Fig. 42a). The line excitation shape is larger than the grating, but if it is translated slightly, a change in the position and intensity of the peaks in Fig. 42a is observed. The threshold is reached at  $75\mu\text{J}/\text{cm}^2$  (Fig. 42b), a reduction by a factor of more than 3. In the angular image (Fig. 42c), the gain band is narrower, but photonic bands appear more faded than in Fig. 41c.

These differences can be attributed directly to the excitation shape. First, the used spot was quite large, so a large amount of unimprinted bulk material around the grating was excited as well. Also, ASE can occur in any direction within the spot. For a stripe excitation, ASE occurs more strongly along the major axis of the stripe, as this provides more opportunity for interaction with the active material. ASE that is not perpendicular to the grating in a circular excitation spot appears as a parasitic loss, thus increasing the threshold for lasing. The irregular peak shape seen for the line excitation exhibits properties of RL. Many peaks close together could originate from random cavities within the active material. Also, no strong photonic bands in Fig. 42c indicate a

limited influence of the grating. The line excitation promotes random cavities along the major axis, which may even produce limited spatial coherence, as seen by the yellow area in Fig. 42c.

## 6.6. Sample 2: Cryo-Cooling

Sample 2 has a thinner active layer (80nm), and UV-NIL resin was diluted to reduce the residual layer thickness. The condensate seen forming on the surface is suspected to be water, most likely as a residue from ambient air after evacuating the cryostat. Although it appears to spare the grating, it can be hypothesized that the grating grooves are filled with water ice. As  $n_{H_2O} \cong 1.3$ , the index modulation of the grating is thus greatly reduced. The result is that almost no grating influence on the emission spectrum is visible at all. The threshold of the bulk area is reduced by a factor of 5.6, and the intensity of the emission is increased by cooling. The issue of condensation could be tackled by allowing the sample to warm up again to room temperature after cooling – the vacuum in the chamber helps the water to vaporize, and through continuous pumping water content in the chamber can be reduced further.

Even after the removal of the condensate, only very weak signals from the grating could be seen when the large chirped grating (structure A) was excited. The weak signal is still sufficient to identify the mode crossing. Also, due to the lower collection angle of the 10x objective, less light overall is collected, and the mode lines appear weaker and with higher slopes, making it harder to identify them. The slight shift in gain band position can also be utilized. If a grating is just barely outside of the resonance condition, temperature adjustments can move the gain band to the desired position, with up to 8nm blueshift achievable when going from RT to 77K. Another big difference is the reduced active layer thickness of only 80nm, which leads to higher leakage of the mode from the active layer (which should be beneficial to grating interaction according to Tab. 12. One drawback is that the resonance condition shifts to gratings of  $\Lambda=468\text{nm}$  at RT - gratings with a constant period were only available up to  $\Lambda=450$  on this sample.

Cooling the sample offers great promise to reduce the threshold, perhaps aiding in cases where lower thresholds are needed, or enabling electrically pumped lasing in the future.

### **6.7. Sample 3: Grating Length Study**

The UV-NIL resin for sample 3 is UV-A4, which was spun at 6000rpm, to reduce the residual layer thickness. The results indicate that longer gratings (meaning higher gain length) enable lower thresholds for lasing and/or ASE. This seems plausible from a physical point of view – light has a longer path within the medium where it can be amplified before being emitted from the grating. The lower value at 40 $\mu$ m can be seen as an outlier – its stronger extinction indicates that the 40 $\mu$ m grating on this sample might have just been of better quality than the others. The gradual decrease in FWHM implies that first wider peaks appear which only gradually narrow with increasing fluence. This might correlate with ASE. The 100nm grating shows an earlier decrease of FWHM, while still having a threshold in the range of the other gratings. This indicates some additional emission phenomena taking place at lower fluence, perhaps a high-Q random cavity is involved. The extinction ratios don't allow any conclusions on which grating emits more polarized light.

Through those findings, it was decided to mainly focus on measuring gratings with longer gain lengths for further experiments. Additionally, differences between similar grating lengths (for example 120 $\mu$ m and 140 $\mu$ m) were discovered to be minimal compared to inhomogeneities within samples.

### **6.8. Sample 4: Main Findings**

From the preliminary comparisons, it can be seen that having a longer excitation stripe does not negatively affect the threshold of the gratings observed. Although some bulk area is excited in the vicinity of the grating, the parasitic loss is minimal since in that case, the appearing ASE is strongly perpendicular to the grating and can couple to the grating. The spectra in Fig. 48 indicate that for longer lines, RL does become an issue as multiple peaks appear around a main peak, most likely caused by the grating. The excitation of the bulk material around the grating is strong enough to excite RL cavities that lie within the excitation shape. The peaks that appear around the main peak also change position and intensity when a slight translation of the sample is performed, which might be due to different RL cavities being in favorable conditions upon translating.

When comparing the same grating over ITO to one without ITO, it is apparent that having the ITO in place leads to lower thresholds, and produces a higher slope after threshold, indicating stronger coupling between grating and active material. This might be due to the fact that the ITO-free structures were located closer to the edge of the substrate than the structures with ITO. It was observed in previous experiments that slight thickness variations in the active layer are common. Also, in sample 1 it was shown that resonance occurs at different grating periods for films of different thicknesses, meaning that the grating without ITO was not in a perfect resonance condition, while the one with ITO was. This could explain the slight variation in threshold and slope after threshold.

In this sample, the emission is very fine, both over ITO and over no ITO areas. The TE mode crossing appears to lie between 402nm and 406nm. The combination of all features like small line width (below 0.1nm), strong angular emission, far-field pattern with intersecting lobes, strong polarization, and narrow emission angle all point to DFB lasing.

In the bulk measurements of sample 4, a threshold of around  $90\mu\text{J}/\text{cm}^2$  is observed, as well as a high extinction ratio of 21. The spectrum exhibits multiple peaks around 786nm, which are spectrally fine ( $\sim 0.12\text{nm}$ ) as apparent in Fig. 52c. The signal indicates RL, consistent with what was measured on previous samples. In the 2D spectrum, the truncation of the line can be seen at the top of the image, as the bright vertical line has a slight drop in intensity. The strong polarization of the light (cf. Fig. 51c) can be explained by the excitation shape: If RL occurs preferentially for light traveling along the major axis of the excitation area, a high degree of spatial coherence is produced. The lack of photonic structures in the angular image (Fig. 51e) and the far-field image (Fig. 51f) confirm that there is no influence of a periodic structure.

Once the beam is moved over a grating, the signal characteristics change significantly. Over the 406nm grating with ITO, the spectrum presents one single narrow line, which also does not change its wavelength if the beam is slightly translated within the grating. Through visual inspection and fitting, the threshold is found around  $80\mu\text{J}/\text{cm}^2$ . The FWHM plot shows that before the fine line is detected, a plateau appears, indicating that ASE precedes the lasing line, which can also be recognized as a wide peak (and as a sort of base, from which the peak emerges at higher fluences) in the spectrum.

The grating shows stronger extinction than the bulk, with a value of  $\sim 33$ . In the 2D spectrum, the grating dimensions can clearly be distinguished. The line within the grating appears to be brighter towards the edges. Strong angular features are visible in the spectral Fourier transform (Fig. 53e), with a central bright spot where the mode bands cross. A faint vertical line is also present, which corresponds to the gain band. The far-field image shows two lobes intersecting. According to *Kogelnik et al.*<sup>53</sup>, this is indicative of DFB lasing, as two curved photonic bands with minimal separation are to be expected for a grating in resonance.

With a higher resolution of the spectrometer, the features appear similar. Not only one peak is visible in the spectrum, but multiple modes, equally spaced and symmetrical around the main peak are detected (Fig. 54a). If the extinction of the main peak is measured specifically, an extinction ratio as high as 53 is reached (Fig. 54g). The angular image also shows more than one spectral line, in accordance with the 2D spectrum (Fig. 54d and f). The light tends to be intensified within the area of the modes crossing. The peaks on the left side of the spectrum appear to be depressed for some reason (perhaps due to some imperfection within the grating) compared to the right side.

In the finest spectrometer setting, the line width is measured to be around 0.09nm. The threshold is a bit lower than in the regular setting, lying at  $\sim 75\mu\text{J}/\text{cm}^2$  visually and at  $\sim 71\mu\text{J}/\text{cm}^2$  in the fit. A Q-factor in the order of 8500 is calculated for this cavity.

A 406nm grating without ITO interlayer shows similar thresholds, and also exhibits a very fine line. The far-field spectra are less intense, and extinction is also not as high as for gratings with ITO. Those minor differences may be attributed to the slight differences in layer thickness through the spin-coating process, as discussed earlier.

A grating further removed from the mode crossing (426nm) already shows distinctly different characteristics. The threshold is higher, and the peak shape is more irregular (Fig. 57a and b). Higher FWHM can be seen, and an extensive ASE plateau is visible (Fig. 57b). The extinction is still quite high, reaching a value of 39 (Fig. 57c). The angular spectrum reveals that the gain band is very narrow (most likely influenced by the grating) and shows amplification at the intersections with the forward and backward propagating mode lines, although less intense than for the 406nm grating (Fig. 57e).



All the observations mentioned above indicate single-mode lasing supported by the resonator. The light is amplified by the grating, as is apparent from Fig. 53d, and Fig. 54c and d. The light is emitted under a very fine angle, as seen in Fig. 53e, and Fig. 54e and f. The far-field pattern shows strong features, and the beam is highly polarized. Most convincingly, the peak is not dependent on the position of the beam on the grating. Furthermore, it appears that multiple cavity modes of the grating can be seen in the higher resolution spectrograms in Fig. 54a, d, and f, and Fig. 55a.

One major difference between sample 4 and all other samples within this thesis is the use of PS90 as working stamp material; sample 1 used PS380, while samples 2, 3, and 5 used PS40. PS90 is harder and showed better replication qualities in XSEM (cf. chapter 5.3.3). Since sample 1 was only measured with a line excitation of variant A, which can be longer than 250 $\mu\text{m}$  (cf. Fig. 12), it might be the case that lasing similar to sample 4 could have been observed with a line of variant B, and the RL as observed in chapter 6.5 was due to the high amount of bulk excitation.

## 6.9. Sample 5: $\text{FAPbI}_3$

The sample with the second active material,  $\text{FAPbI}_3$ , generally shows higher thresholds compared to  $\text{MAPbI}_3$ . SE takes place at a higher wavelength ( $\sim 800\text{nm}$ ). Sharp peaks appearing around 810nm are generally less pronounced, and the very weak polarization leads to the conclusion that in this case, strong ASE in combination with only weak (random) lasing is recorded. This hypothesis is supported by the angular images, which show only weak grating interaction. The mode crossing is found around a grating period of 440nm. Where the vertical line intersects the mode lobes, no strong amplification can be seen. The vertical lines have a wide envelope, indicating a strong ASE influence. Far-field images show some features, but fairly weak.

One additional consideration is the stability of  $\text{FAPbI}_3$  in air.  $\text{FAPbI}_3$  exhibits a yellow phase at room temperature, which is converted to a metastable black phase during annealing (done for this sample at 90°C until color change was observed after  $\sim 30\text{min}$ ). To prevent phase changes,  $\text{FAPbI}_3$  is often stabilized by exchanging small amounts of anions or cations.<sup>54</sup> This was not done in this study, meaning limited amounts of phase change cannot be excluded, although no color change was observed visually.

## 7. Summary and Outlook

The benefits of linear excitation shapes have been shown. Studies of the length of the excitation shape have shown little influence on thresholds for excitation spots up to twice the length of the studied grating, although peaks show increasing noise from RL for longer lines. If gratings of different lengths are compared, thresholds for longer gratings are lower. Cooling the sample to 77K can reduce the threshold by a factor of 5.

As thoroughly discussed in chapter 6.8, single-mode lasing from a grating produced in the UV-NIL process is demonstrated, exhibiting thresholds in the range of  $80\mu\text{J}/\text{cm}^2$ . Linewidths below 0.1nm are measured. The findings are supported by narrow angular emission and a strong far-field pattern.

The perovskite laser research group at *imec* did further research into the mechanisms at hand, and a paper is being prepared about the findings. In it, more evidence for discerning RL and single mode cavity lasing is presented, taking coupled wave theory into consideration (Iakov Goldberg, Nirav Annavarapu, Simon Leitner, Karim Elkhoully, Fei Han, Tibor Kuna, Weiming Qiu, Cedric Rolin, Jan Genoe, Robert Gehlhaar, and Paul Heremans", **Multimode Lasing in All-Solution-Processed UV-Nanoimprinted Distributed Feedback MAPbI<sub>3</sub> Perovskite Waveguides**". Submitted to ACS Photonics in February 2023).

Other samples and unimprinted areas showed predominantly random lasing under line excitation, which is caused by the combination of having a linear beam shape, as well as the multitude of scattering centers owing to the small grain size of the active films. If a spot is used instead, RL is less visible due to a stronger ASE signal. Placing the grating above the active layer (especially even with interlayers like ITO present) showed no adverse effects on the threshold or lasing peak shape, and thus demonstrates great promise as an alternative way to produce resonators in pursuit of electrically pumped perovskite lasers. Applications in other related fields seem plausible as well.

Regarding working stamp materials, the importance of a balance between sufficient hardness and reduced adhesion is made apparent. Once a fully functioning electrically pumped

device is demonstrated, the cause of the low adhesion between UV-NIL resin and stack may be explored, and improved upon to aid commercialization.

One inherent downside of gratings produced using any kind of NIL is pattern fidelity. A lot of parameters, many of which are not fully understood or controllable yet, influence the quality of the imprints. Also, curing the resins at temperatures according to the manufacturer's instructions may degrade perovskites, which in our case could not be detected. The fact that gratings are deposited above any other layers means that the used solvents have to be compatible with all the layers below, to make sure no unwanted interactions (like dissolution or degradation of a layer) occur.

In conclusion, it has been demonstrated that nanoimprint lithography can significantly reduce the time and cost related to producing a DFB resonator, and possibly other resonator geometries as well. As an outlook, the material selection for working stamps and UV resin can further be explored, and process parameters further optimized to produce high-fidelity structures. Adhesion is one major problem between perovskites and UV resin. If further layers are introduced to the system (e.g., electrode layers like ITO, or electron/hole transfer layers), special care must be taken to guarantee proper adhesion. In general, more detailed studies into the interfacial interactions between UV resin, perovskites, and any interlayers can be pursued in the future.

## 8. Literature

- (1) DiLaura, D. A Brief History of Lighting. *Opt. Photonics News* **2008**, *19* (9), 22–28. DOI: 10.1364/OPN.19.9.000022.
- (2) Einstein, A. Zur Quantentheorie der Strahlung. *Phys. Z.* **1917** (18), 121–128.
- (3) Straumann, N. Einstein in 1916: "On the Quantum Theory of Radiation". *SPS Comm.* **2017**, *51*, 26–31.
- (4) Maiman, T. H. Stimulated Optical Radiation in Ruby. *Nature* **1960**, *187* (4736), 493–494. DOI: 10.1038/187493a0.
- (5) Heliotis, G.; Xia, R.; Bradley, D. D. C.; Turnbull, G. A.; Samuel, I. D. W.; Andrew, P.; Barnes, W. L. Blue, surface-emitting, distributed feedback polyfluorene lasers. *Appl. Phys. Lett.* **2003**, *83* (11), 2118–2120. DOI: 10.1063/1.1612903.
- (6) Riedl, T.; Rabe, T.; Johannes, H.-H.; Kowalsky, W.; Wang, J.; Weimann, T.; Hinze, P.; Nehls, B.; Farrell, T.; Scherf, U. Tunable organic thin-film laser pumped by an inorganic violet diode laser. *Appl. Phys. Lett.* **2006**, *88* (24), 241116. DOI: 10.1063/1.2211947.
- (7) Samuel, I. D. W.; Turnbull, G. A. Organic semiconductor lasers. *Chem. Rev.* **2007**, *107* (4), 1272–1295. DOI: 10.1021/cr050152i.
- (8) Chénais, S. Organic Lasers: Introductory Course, Université Paris 13, Bouthéon Castle, France, 2014.
- (9) Chénais, S.; Forget, S. Recent advances in solid-state organic lasers. *Polym. Int.* **2012**, *61* (3), 390–406. DOI: 10.1002/pi.3173.
- (10) Zhang, Q.; Su, R.; Du, W.; Liu, X.; Zhao, L.; Ha, S. T.; Xiong, Q. Advances in Small Perovskite-Based Lasers. *Small Methods* **2017**, *1* (9), 1700163. DOI: 10.1002/smtd.201700163.
- (11) Tan, Z.-K.; Moghaddam, R. S.; Lai, M. L.; Docampo, P.; Higler, R.; Deschler, F.; Price, M.; Sadhanala, A.; Pazos, L. M.; Credgington, D.; Hanusch, F.; Bein, T.; Snaith, H. J.; Friend, R. H.

Bright light-emitting diodes based on organometal halide perovskite. *Nat. Nanotechnol.* **2014**, *9* (9), 687–692. DOI: 10.1038/nnano.2014.149.

(12) Deschler, F.; Price, M.; Pathak, S.; Klintberg, L. E.; Jarausch, D.-D.; Higler, R.; Hüttner, S.; Leijtens, T.; Stranks, S. D.; Snaith, H. J.; Atatüre, M.; Phillips, R. T.; Friend, R. H. High Photoluminescence Efficiency and Optically Pumped Lasing in Solution-Processed Mixed Halide Perovskite Semiconductors. *J. Phys. Chem. Lett.* **2014**, *5* (8), 1421–1426. DOI: 10.1021/jz5005285.

(13) Cho, C.; Antrack, T.; Kroll, M.; An, Q.; Bärschneider, T. R.; Fischer, A.; Meister, S.; Vaynzof, Y.; Leo, K. Electrical Pumping of Perovskite Diodes: Toward Stimulated Emission. *Adv. Sci.* **2021**, *8* (17), e2101663. DOI: 10.1002/advs.202101663.

(14) Feldman, M., Ed. *Nanolithography: The art of fabricating nanoelectric and nanophotonic devices and systems*; Woodhead Publishing Series in Electronic and Optical Materials, Vol. 42; Woodhead Publishing, 2014.

(15) Schiff, H. Nanoimprint lithography: 2D or not 2D? A review. *Appl. Phys. A* **2015**, *121* (2), 415–435. DOI: 10.1007/s00339-015-9106-3.

(16) Kooy, N.; Mohamed, K.; Pin, L. T.; Guan, O. S. A review of roll-to-roll nanoimprint lithography. *Nanoscale Res. Lett.* **2014**, *9*, 1–13.

(17) Bonal, V.; Quintana, J. A.; Villalvilla, J. M.; Boj, P. G.; Díaz-García, M. A. Controlling the emission properties of solution-processed organic distributed feedback lasers through resonator design. *Sci. Rep.* **2019**, *9* (1), 11159. DOI: 10.1038/s41598-019-47589-4.

(18) Svelto, O. *Principles of Lasers*; Springer US, 2010. DOI: 10.1007/978-1-4419-1302-9.

(19) Dutta, A. Stimulated Emission, Indian Institute of Technology Bombay, Bombay. <https://www.youtube.com/watch?v=4UzqPv8IXgs> (accessed 2022-11-08).

(20) Mason, B.; Fish, G. A.; DenBaars, S. P.; Coldren, L. A. Widely tunable sampled grating DBR laser with integrated electroabsorption modulator. *IEEE Photon. Technol. Lett.* **1999**, *11* (6), 638–640. DOI: 10.1109/68.766769.

- (21) Millett, R.; Hinzer, K.; Benhsaien, A.; Hall, T. J.; Schriemer, H. The impact of laterally coupled grating microstructure on effective coupling coefficients. *Nanotechnology* **2010**, *21* (13), 134015. DOI: 10.1088/0957-4484/21/13/134015.
- (22) Navarro-Fuster, V.; Vragovic, I.; Calzado, E. M.; Boj, P. G.; Quintana, J. A.; Villalvilla, J. M.; Retolaza, A.; Juarros, A.; Otaduy, D.; Merino, S.; Díaz-García, M. A. Film thickness and grating depth variation in organic second-order distributed feedback lasers. *J. Appl. Phys.* **2012**, *112* (4), 43104. DOI: 10.1063/1.4745047.
- (23) He, L.; Özdemir, Ş. K.; Yang, L. Whispering gallery microcavity lasers. *Laser Photonics Rev.* **2013**, *7* (1), 60–82. DOI: 10.1002/lpor.201100032.
- (24) Fürst, J. U.; Strelakov, D. V.; Elser, D.; Aiello, A.; Andersen, U. L.; Marquardt, C.; Leuchs, G. Quantum light from a whispering-gallery-mode disk resonator. *Phys. Rev. Lett.* **2011**, *106* (11), 113901. DOI: 10.1103/PhysRevLett.106.113901.
- (25) Navarro-Fuster, V.; Boj, P. G.; Villalvilla, J. M.; Quintana, J. A.; Díaz-García, M. A.; Trabadelo, V.; Juarros, A.; Retolaza, A.; Merino, S. Second-order distributed feedback lasers based on films containing perylenediimide derivatives. In *Organic Photonics IV*; Heremans, P. L., Coehoorn, R., Adachi, C., Eds.; SPIE, 2010; 77221G. DOI: 10.1117/12.854281.
- (26) Eichhorn, M.; Pollnau, M. The Q-factor of a Continuous-wave Laser. In *Conference on Lasers and Electro-Optics 2012*; JW2A.29. DOI: 10.1364/CLEO\_AT.2012.JW2A.29.
- (27) Green, E. I. The Story of Q. *Am. Sci.* **1955** (43), 584–594.
- (28) Turnbull, G. A.; Andrew, P.; Jory, M. J.; Barnes, W. L.; Samuel, I. D. W. Relationship between photonic band structure and emission characteristics of a polymer distributed feedback laser. *Phys. Rev. B* **2001**, *64* (12), 125122. DOI: 10.1103/PhysRevB.64.125122.
- (29) Andrew, P.; Turnbull, G. A.; Samuel, I. D. W.; Barnes, W. L. Photonic band structure and emission characteristics of a metal-backed polymeric distributed feedback laser. *Appl. Phys. Lett.* **2002**, *81* (6), 954–956. DOI: 10.1063/1.1496497.
- (30) Samuel, I. D. W.; Namdas, E. B.; Turnbull, G. A. How to recognize lasing. *Nat. Photonics* **2009**, *3* (10), 546–549. DOI: 10.1038/nphoton.2009.173.

- (31) Chou, S. Y.; Krauss, P. R.; Renstrom, P. J. Imprint of sub-25 nm vias and trenches in polymers. *Appl. Phys. Lett.* **1995**, *67* (21), 3114–3116. DOI: 10.1063/1.114851.
- (32) Chou, S. Y. Nanoimprint lithography. *J. Vac. Sci. Technol. B* **1996**, *14* (6), 4129–4133. DOI: 10.1116/1.588605.
- (33) Schiff, H. Nanoimprint lithography: An old story in modern times? A review. *J. Vac. Sci. Technol. B* **2008**, *26* (2), 458. DOI: 10.1116/1.2890972.
- (34) Hamouda, F.; Aassime, A.; Bertin, H.; Gogol, P.; Bartenlian, B.; Dagens, B. Tunable diffraction grating in flexible substrate by UV-nanoimprint lithography. *J. Micromech. Microeng.* **2017**, *27* (2), 25017. DOI: 10.1088/1361-6439/aa5404.
- (35) Asif, M. H.; Graczyk, M.; Heidari, B.; Maximov, I. Comparison of UV-curable materials for high-resolution polymer nanoimprint stamps. *Micro and Nano Engineering* **2022**, *14*, 100118. DOI: 10.1016/j.mne.2022.100118.
- (36) Kistler, S. F., Ed. *Liquid Film Coating: Scientific principles and their technological implications*; Springer, 1997. DOI: 10.1007/978-94-011-5342-3.
- (37) Sahu, N.; Parija, B.; Panigrahi, S. Fundamental understanding and modeling of spin coating process: A review. *Indian J. Phys.* **2009**, *83* (4), 493–502. DOI: 10.1007/s12648-009-0009-z.
- (38) D. E. Bornside; C. W. Macosko; L. E. Scriven. Modeling of Spin Coating. *J. Imaging Technol.* **1987**, *13* (4), 122–130.
- (39) Tilley, R. J. D. *Perovskites: Structure-property relationships*; John Wiley & Sons, Ltd, 2016.
- (40) Giorgi, M. L. de; Anni, M. Amplified Spontaneous Emission and Lasing in Lead Halide Perovskites: State of the Art and Perspectives. *Appl. Sci.* **2019**, *9* (21), 4591. DOI: 10.3390/app9214591.
- (41) Pourdavoud, N.; Haeger, T.; Mayer, A.; Cegielski, P. J.; Giesecke, A. L.; Heiderhoff, R.; Olthof, S.; Zaefferer, S.; Shutsko, I.; Henkel, A.; Becker-Koch, D.; Stein, M.; Cehovski, M.; Charfi, O.; Johannes, H.-H.; Rogalla, D.; Lemme, M. C.; Koch, M.; Vaynzof, Y.; Meerholz, K.; Kowalsky, W.; Scheer, H.-C.; Görrn, P.; Riedl, T. Room-Temperature Stimulated Emission and Lasing in

Recrystallized Cesium Lead Bromide Perovskite Thin Films. *Adv. Mater.* **2019**, *31* (39), e1903717. DOI: 10.1002/adma.201903717.

(42) Li, Z.; Moon, J.; Gharajeh, A.; Haroldson, R.; Hawkins, R.; Hu, W.; Zakhidov, A.; Gu, Q. Room-Temperature Continuous-Wave Operation of Organometal Halide Perovskite Lasers. *ACS nano* **2018**, *12* (11), 10968–10976. DOI: 10.1021/acsnano.8b04854.

(43) Sum, T.-C.; Mathews, N. *Halide Perovskites - Photovoltaics, Light Emitting Devices, and Beyond*; John Wiley & Sons, Inc, 2019.

(44) Zhizhchenko, A.; Syubaev, S.; Berestennikov, A.; Yulin, A. V.; Porfirev, A.; Pushkarev, A.; Shishkin, I.; Golokhvast, K.; Bogdanov, A. A.; Zakhidov, A. A.; Kuchmizhak, A. A.; Kivshar, Y. S.; Makarov, S. V. Single-Mode Lasing from Imprinted Halide-Perovskite Microdisks. *ACS nano* **2019**, *13* (4), 4140–4147. DOI: 10.1021/acsnano.8b08948.

(45) Pourdavoud, N. Stimulated Emission and Lasing in Metal Halide Perovskites by Direct Thermal Nanoimprint. Dissertation, Bergische Universität Wuppertal, Wuppertal, 2020. <https://nbn-resolving.org/urn/resolver.pl?urn=urn%3Anbn%3Ade%3Ahbz%3A468-20200924-085950-5>.

(46) Basak, S.; Bar-On, O.; Scheuer, J. Metal-halide perovskite-based edge emitting lasers. *Opt. Mater. Express* **2022**, *12* (2), 375–383. DOI: 10.1364/OME.443294.

(47) Satyalakshmi, K. M.; Olkhovets, A.; Metzler, M. G.; Harnett, C. K.; Tanenbaum, D. M.; Craighead, H. G. Charge induced pattern distortion in low energy electron beam lithography. *J. Vac. Sci. Technol. B* **2000**, *18* (6), 3122. DOI: 10.1116/1.1321755.

(48) Bass, M., Ed. *Handbook of Optics: Volume II: Devices, Measurements, and Properties*, 2nd ed.; Handbook of Optics, Vol. 2; McGraw-Hill, Inc., 1995.

(49) Milanese, S.; Giorgi, M. L. de; Anni, M. Determination of the Best Empiric Method to Quantify the Amplified Spontaneous Emission Threshold in Polymeric Active Waveguides. *Molecules* **2020**, *25* (13), 2992. DOI: 10.3390/molecules25132992.

(50) Milanese, S.; Giorgi, M. L. de; Cerdán, L.; La-Placa, M.-G.; Jamaludin, N. F.; Bruno, A.; Bolink, H. J.; Kovalenko, M. V.; Anni, M. Amplified Spontaneous Emission Threshold Dependence on Determination Method in Dye-Doped Polymer and Lead Halide Perovskite Waveguides. *Molecules* **2022**, *27* (13), 4261. DOI: 10.3390/molecules27134261.



(51) Palatnik, A.; Cho, C.; Zhang, C.; Sudzius, M.; Kroll, M.; Meister, S.; Leo, K. Control of Emission Characteristics of Perovskite Lasers through Optical Feedback. *Advanced Photonics Research* **2021**, *2* (12), 2100177. DOI: 10.1002/adpr.202100177.

(52) Meshalkin, A. Y.; Podlipnov, V. V.; Ustinov, A. V.; Achimova, E. A. Analysis of diffraction efficiency of phase gratings in dependence of duty cycle and depth. *J. Phys.: Conf. Ser.* **2019**, *1368* (2), 22047. DOI: 10.1088/1742-6596/1368/2/022047.

(53) Kogelnik, H.; Shank, C. V. Coupled-Wave Theory of Distributed Feedback Lasers. *J. Appl. Phys.* **1972**, *43* (5), 2327–2335. DOI: 10.1063/1.1661499.

(54) Masi, S.; Gualdrón-Reyes, A. F.; Mora-Seró, I. Stabilization of Black Perovskite Phase in FAPbI<sub>3</sub> and CsPbI<sub>3</sub>. *ACS Energy Lett.* **2020**, *5* (6), 1974–1985. DOI: 10.1021/acsenergylett.0c00801.